Investigation of the Properties of X-ray Pulsars during Outbursts

A Thesis

submitted for the Award of Ph.D. degree of

Mohanlal Sukhadia University

in the

Faculty of Science

By

Prahlad Rameya Epili

Dr. Sachindranatha Naik

Associate Professor

Astronomy & Astrophysics Division

Physical Research Laboratory, Ahmedabad, India

DEPARTMENT OF PHYSICS

FACULTY OF SCIENCE

MOHANLAL SUKHADIA UNIVERSITY

UDAIPUR (RAJ)

Year of submission: 2018

Chapter 1

Introduction

1.1 X-ray Astronomy: The early years

The idea that the extra-solar objects also emit in X-rays has got much attention after the World War II. It was mainly because of the advancement of technology in sending the X-ray detectors above the Earth's atmosphere. The rocket flight experiment in 1962, led by Riccardo Giacconi, discovered the first X-ray source in Scorpius constellation outside the solar system. This source was later designated as Sco X-1 (Giacconi et al., 1962). After the discovery of Sco X-1, about 30 other X-ray sources were discovered in subsequent rocket experiments. Apart from these discoveries, many new X-ray sources were also discovered serendipitously by the next generation of X-ray instruments. The first X-ray astronomy satellite, *Uhuru* that was flown to space, catalogued 339 X-ray sources during its three years of mission life time (1970 - 1973). Majority of these sources are later classified as X-ray binaries, galaxies, galaxy clusters, supernova remnants etc. Among these sources the discovery of X-ray pulsars has enriched the X-ray astronomy as it led to theoretical developments explaining the pulsed emission from these sources. The mechanism of X-ray emission from these objects was immediately understood to be due to the *accretion* of matter by the compact stellar sources (namely: Neutron stars) residing in a binary system with another normal star.

1.2 X-ray Binaries and their Classification

X-ray binaries are brightest celestial X-ray sources in the sky comprising of a compact object (i.e either a neutron star, black hole or a white-dwarf) and a companion star in a binary system. The compact object in these systems outshines in X-rays with luminosity in the range of $10^{34} - 10^{38} ergs\ s^{-1}$ and orbits around the common center of mass of the binary system. These cosmic sources came into limelight in 1962 with the discovery of Scorpius X-1, the first X-ray source to be discovered outside the solar system. A vast majority of such Galactic X-ray sources ($> 90\%$) were found in binary systems. Depending upon the mass of the companion star, the binary systems are classified as into two different classes such as (i) High Mass X-ray Binaries (HMXBs) and (ii) Low Mass X-ray Binaries (LMXBs). A major fraction (i.e 90%) of Galactic X-ray sources present in binary systems can be classified into either of these categories (Lewin and van der Klis, 2006; Tauris and van den Heuvel, 2006). In our Galaxy, there are about 300 X-ray binary sources known so far. Among these, 187 are classified as LMXBs and 113 as HMXBs (Liu et al., 2006, 2007).

1.2.1 Low Mass X-ray Binaries

In low mass X-ray binaries (LMXBs), the mass donor or the secondary star is a low-mass star ($M \leq 1\ M_{\odot}$) whereas the compact object is either a neutron star or a black hole. During the evolution process, the companion star first fills its Roche lobe in the binary system. After this, mass transfer from the companion star to the compact object takes place through the inner Lagrangian point. The accreted matter then spirals around the compact object forming an disc-like structure known as accretion disc. As the accreting matter has specific angular momentum (J), it doesn't hit the accreting object directly. Therefore, the accreting matter first encircles around the accretor at a radii given by *circularization radius*, R_{circ} before losing its angular momentum.

$$R_{circ} = \frac{J^2}{G\,M_c} \tag{1.1}$$

Here M_c is the mass of the accreting object (i.e NS or BH). As per the standard assumptions of accretion disk theory, the accreting matter loses its energy at a faster rate than the angular momentum. So, the accretion continues in a series of circular orbits with decreasing angular momentum. Before settling into smaller circular orbits, the angular momentum of accreting matter gets transported to outer layers of the disc through viscosity. This also helps in energy dissipation of inner disc layers thereby providing a torque between adjacent Kepler orbits. A brief discussion regarding disc-accretion is given in Section 1.3.1.

The less massive optical counterparts in LMXBs are rather faint with $L_{opt}/Lx << 0.1$. The orbital period of these binary systems is very short (i.e within a few hours to few days). The reprocessed X-ray emission from the accretion disk dominates over the optical emission. The number of LMXBs identified so far is nearly 200 (Liu et al. (2007)). This includes those present in our Galaxy and in the Magellanic clouds. Unlike HMXBs (which are bright in X-rays), the identification of the compact object in LMXBs is very difficult owing to their low X-ray luminosity. Secondly, the optical spectra of LMXBs are characterized by hot and blue continuum with broad H and He emission lines (Lewin and van der Klis (2006)).

1.2.2 High Mass X-ray Binaries

High Mass X-ray binaries (HMXBs) are the luminous X-ray sources in our Galaxy. During the initial days (i.e. in 1970s), these bright sources were the first ones to be identified with their optical companions (Liu et al., 2007). The X-ray brightness of the compact sources in these systems is due to the accretion of matter from the OB companion stars. The companion star in this case happens to be a young (i.e $< 10^7$ Yr) and massive star ($\geq 10\ M_\odot$) also referred as the mass *donor* star in the binary. The compact star can be either a black hole or a neutron star. The stellar wind of the OB companion star reaches a terminal velocity of $\sim 2000\ \mathrm{km\,s^{-1}}$with an effective mass loss of $10^{-6} - 10^{-10} M_\odot\ \mathrm{yr}^{-1}$ (Lewin and van der Klis (2006)). Depending on the luminosity class of the optical companions, the high mass X-ray binaries are further classified as (i) supergiant X-ray Binaries and (ii) Be/X-ray binaries.

Supergiant X-ray Binaries

The mass donor in a Supergiant X-ray Binary (SgXB) system is a luminosity OB-type star of luminosity class I-II. The X-ray binaries such as Vela-X1, GX 301-2 represent the class of SgXBs. In the SgXB, the compact object is a NS acreting matter from the dense stellar wind of the OB supergiant companion. A typical mass loss rate of these donor stars is of the order of 10^{-6} $M_{\odot}$ yr^{-1} in the form of winds with terminal velocities $\sim$ 1500 $km\,s^{-1}$. In our Galaxy, majority of HMXBs are populated near the Galactic plane (i.e located close to their birth place). Before the launch of *INTEGRAL* (i.e until 2002), the total number of HMXBs identified in the Milky Way was 110. Among these, only 13 systems were confirmed to be SgXBs. The classification of the remaining 45 systems was not done due to lack of sufficient information on the characteristics of the optical companion stars (Walter et al., 2015). However, the discovery of 23 new SgXBs with the *INTEGRAL* mission has increased the HMXB population in the Galaxy. Among the known HMXBs, there are almost 40 confirmed systems consisting of pulsating neutron stars with typical spin and orbital periods in the ranges of 10 - 300 s and $\leq$ 10 days, respectively. The eccentricity of these systems lies in $e \leq 0.1$. Cen X-3, SMC X-1 are some of the bright sources in this class of binary systems. The optical luminosity of the companion star ($L_{opt} > 10^5$ $L_{\odot}$) and its spectral type indicate that these are O-type progenitor stars having intial ZAMS mass and radii of $\geq$ 20 $M_{\odot}$ and $10-30$ $R_{\odot}$, respectively.

Be/X-ray Binaries

The major sub-class of HMXBs are the Be/X-ray binary (BeXB) systems. The Be star in these systems is a non-supergiant star of O or B spectral type. Contrary to the isolated Be stars, the spectral types of Be stars in BeXBs fall in a narrow range of O8-B2 (Negueruela, 1998). These B-emission type stars are rapid rotators with luminosity class III-V. This class of stars rotate faster (with rotation velocity close to their critical limit) till their centrifugal forces balances gravity (Porter and Rivinius, 2003). The rapid rotation causes the surface matter from the Be star spilling up and thereby forming an circumstellar equatorial disk. The companion stars in BeXBs show Balmer emission lines in the optical/infrared spectra. Hence, the qualifier *e* stands for emission lines seen in Be stars. The observed emission lines in the spectra of these Be stars are generally double peaked. The observed emission lines are thought to be due to the reprocessing of the photons emitted from the B star in the circumstellar disk. The circumstellar disk also emits additional continuum radiation in optical and infrared regime, termed as *infrared excess* (Porter and Rivinius, 2003; Reig, 2011).

The accreting compact objects in the BeXBs are mainly neutron stars. In contrast to standard accretion scenarios in X-ray binaries such as through Roche lobe overflow (in LMXBs) and quasi spherical accretion of stellar wind (in HMXBs), the accretion in BeXBs is quite different. When the neutron star in these systems passes through the periastron, accrets huge amount of matter from the extended Be circumstellar disk. This leads to significant enhancement in X-ray emission from the neutron star. The X-ray emission from BeXBs is highly variable. At times, these sources become brightest in the X-ray sky for a few weeks to a couple of months time. These variability in BeXBs can be classified into three major types based on the intensity modulations, luminosity, frequency of occurrence. These are namely: (i) Type-I X-ray outbursts, (ii) Type-II X-ray outbursts and (iii) long periods of quiescence with persistent low luminosity of $L_x \sim 10^{34}$ $erg\ s^{-1}$. From the emission in quiescence to the outburst peak luminosity, the X-ray variabilities in these sources span over $\sim$4 orders of magnitude. This is the extreme case of variability seen in HMXBs. Therefore, these binaries are known as BeXB transients. In Fig. 1.1, a schematic view of a BeXB system is shown where the neutron star accrets matter from the Be disc during its close encounter with the Be star in the binary orbit.

Type-I X-ray Outbursts

This type of X-ray activity in BeXBs coincides with the periastron passage of the neutron star during which the outburst luminosity reaches $L_x \sim 10^{36} - 10^{37}$ erg s^{-1}. These recurring outbursts last for several days to a few tens of days covering a fraction of the orbital period (i.e 20 - 30 % of P_{orb}) (Reig, 2011). The relative X-ray

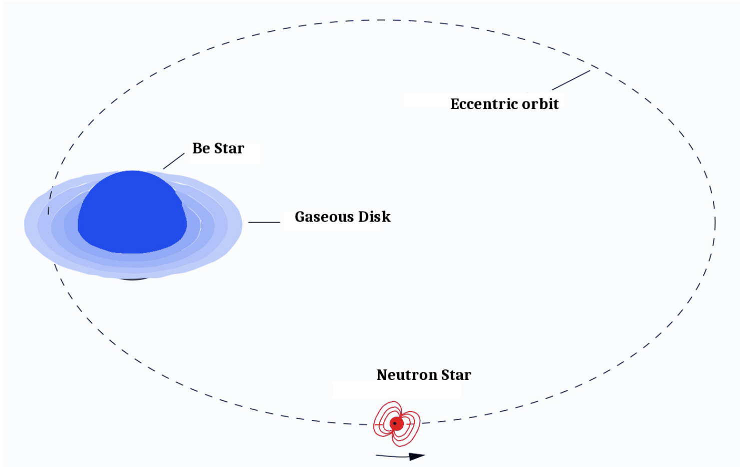

Fig. 1.1 A schematic view of Be/X-ray binary system. The orbiting neutron star during its periastron passage accretes matter from the extended disc of Be star giving rise to transient X-ray outbursts in BeXBs. Figure is adapted from Kretschmar (1996).

variability during Type-I outbursts is greater than a factor of 10 compared to intensity variations observed in quiescence. Majority of the BeXBs show Type-I outbursts. Typical systems showing Type I outbursts almost at every periastron passage include A 0535+262, EXO 2030+375 (Wilson et al., 2008).

Type-II X-ray Outbursts

These are major events in BeXBs. During Type-II outbursts, the luminosity of the X-ray pulsar (neutron star) enhances to $L_x \gtrsim 10^{37}$ $erg\ s^{-1}$. In other words, it increases by a factor of 100-1000 above the quiescent X-ray emission (Reig and Roche, 1999). In some cases, it surpasses the Eddington luminosity for a neutron star (i.e for NS, $L_{Edd} = 1.7 \times 10^{38}$ $erg\ s^{-1}$). Outbursts of these kind continue for a few weeks to months. The beginning of these events in BeXBs does not have any correlation with the orbital parameters of the binary system (Finger and Prince, 1997; Negueruela, 2007). An accretion disk around the neutron star is expected to be formed due to the accretion of matter from the Be circumstellar disk. As there is a substantial amount of matter accreted, angular momentum associated with the accreting matter eventually leads to strong spin-up of the NS. These steady spin-up episodes otherwise are difficult to explain with the direct accretion scenario (Reig, 2011)). A few BeXBs that have shown giant Type-II outbursts since their discovery are : EXO 2030+375 (Parmar et al., 1989a; Wilson et al., 2008), 4U 0115+63 (Baykal et al., 2005; Ferrigno et al., 2009), A0535+362 (Finger et al., 1996), KS 1947+300 (Borozdin et al., 1990; Fürst et al., 2014), V0332+53 (Ferrigno et al., 2016).

Persistent X-ray emission

There are a few BeXBs which show persistent albeit weak X-ray emission. The X-ray luminosity of these type of sources is rather low ($L_x \sim 10^{34} erg\ s^{-1}$) displaying lesser variability. Currently, X-ray binaries such as X Persi and LS I +61 235 represent these systems. The NS in these systems show long spin-periods and low X-ray luminosity. For example, the NS spin period in X-Persei is 837 s and in LS I +61 235, it is 1412 s (Haberl et al., 1998). The long orbital periods in these systems owing to their low X-ray luminosity can be understood from the Corbert diagram (Corbet, 1986). The Corbet diagram represents a relation between the spin period (P_{spin}) and orbital period (P_{orb}) of X-ray pulsars depicting different types of mass transfer processes. In this diagram, the BeXBs show a positive correlation. This implies that the persistent BeXBs having long spin periods are expected to have long orbital periods as well (i.e 100s of days). As a result, the residing neutron star accrets matter from the outermost part of the circumstellar Be disc. The matter density in these regions is comparatively low, resulting in low luminosity.

1.3 Accretion in X-ray binaries

For a self gravitating spherical body of mass M and radius R, the accretion of mass m on to its surface releases gravitational potential energy of the order of

$$\Delta E_{acc} = \frac{GMm}{R}$$

, where G is gravitational constant. If we consider accretion of mass m onto the neutron star of radii $R_* \sim 10$ km and $M_* \sim 1\ M_\odot$, the energy released per gram of the accreted mass will be 10^{20} *ergs* which is $\sim$15% of the rest mass energy of the accreting matter. In other words, accretion onto the compact objects like neutron stars and blackholes (with radii $3(\frac{M}{M_{\odot}})$ km) is the most efficient energy release mechanism over the nuclear processes. In case of white dwarfs ($R_{WD} \sim 10^9$ cm), however, the efficiency of energy release is about 20 times less than the nuclear burning processes.

1.3.1 Accretion onto neutron star X-ray binaries

The mass accretion in X-ray binaries, specifically onto the NS in X-ray binaries occurs in either of the two ways i.e accretion through the capture of stellar-wind or via disc accretion (Roche lobe overflow). In case of LMXBs, the secondary star fills its Roche-lobe. Hence the accretion onto the NS occurs through the formation of a thin disc around it. In case of HMXBs, the massive OB companion stars possess strong stellar wind with velocities as high as ~ 1000 kms^{-1}. These stars have a substantial mass loss of $10^{-4} - 10^{-8} M_{\odot}/yr^{-1}$. Presence of such strong stellar wind in these early-type giants is due to the strong radiation pressure. The capture of a small fraction of these outflow by the NS at a rate of 10^{-9} $M_{\odot}/yr$ is sufficient to radiate in X-rays.

As the accreted matter from the optical companion star enters into the magnetosphere of the NS in binary systems, the accreted plasma reaches the NS surface through various mechanisms, largely depending on the type of accretion flow (i.e quasi-spherical or disk like accretion). The velocity of the accreting plasma outside the magnetospheric radius r_M compared to that of the magnetospheric field is also crucial while considering the entry of matter into the magnetosphere. Another dynamical quantity, known as *corotation radius*, also plays an important role in accretion onto neutron star X-ray binaries. The corotation radius (or the centrifugal radius) r_c is the distance from the pulsar at which the accreted matter corotates with the rigid magnetosphere of the NS before loosing its angular momentum while entering the magnetosphere. This can be estimated by equating the gravity and centrifugal force acting on the matter (of mass m) that co-rotates with the NS.

$$r_c = (GM/\Omega_s^2)^{1/3} = 1.5 \times 10^8 P^{2/3} m^{1/3} \; cm. \tag{1.2}$$

Accretion through Roche-lobe overflow (Disk accretion)

The disk accretion in X-ray binaries is the preferred accretion process when the binary optical star overfills its Roche-lobe. As the compact star and the optical companion star co-rotate around the common center of mass, the gravitational potential due to the binary system at any point can be described by *Roche potential*, Φ_R (Roche 1873) as:

$$\Phi_R(\mathbf{r}) = -\frac{GM_1}{|\mathbf{r}-\mathbf{r_1}|} - \frac{GM_2}{|\mathbf{r}-\mathbf{r_2}|} - \frac{1}{2}(\omega \wedge \mathbf{r})^2 \quad (1.3)$$

where $\mathbf{r_1}$ and $\mathbf{r_2}$ are the position vectors of the two stars. The gravitational potential of the individual stars is described by the first two terms and the third term on the right hand side of equation 1.3 denotes the potential associated with the centrifugal force due to binary motion. A cross-sectional view of the equipotential surfaces of a binary stellar system is shown in Fig.1.2. The critical cross-section passing through the inner Lagrangian point, L1, forms an equipotential surface of dumb-bell shape (known as *Roche lobe*) when seen in three dimensions. The *secondary* star in the binary system evolves faster, expands its outer layer and fills it Roche-lobe. After its lobe is filled, further evolution causes the overflow of matter beyond the Roche-lobe. The material in the overfilled lobe instead of escaping the critical lobe surface altogether, it crosses through L_1 easily into the lobe of the *primary* star. Since both the stars are in a rotating system, the material transferred from the secondary to the compact object through the L_1 point has high specific angular momentum. Thus, it cannot get accreted directly onto the accreting star. Rather, the angular momentum is sufficient to form an *accretion disc* around the compact object. The typical conditions to form an accretion disc around the accreting compact object in X-ray binaries require that the circularization radius (R_{circ}) (Equation 1.1) of the accreting matter (that has high specific angular momentum J) should be greater than the size of the compact object.

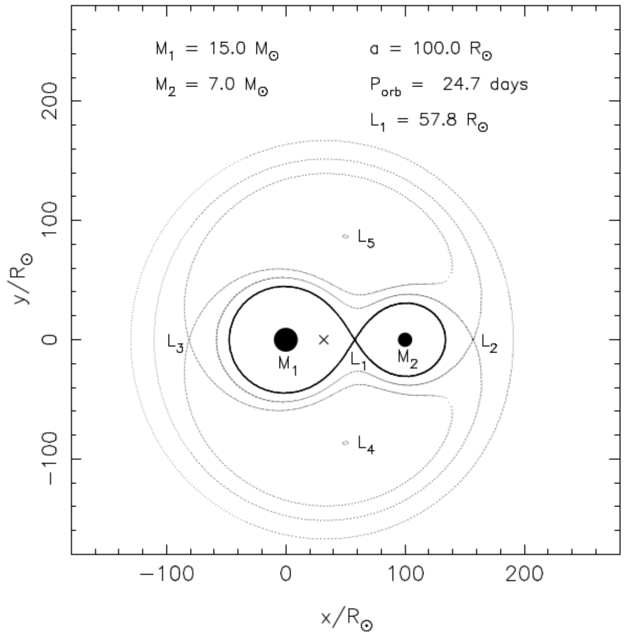

Fig. 1.2 Cross-sectional view of critical equipotential surfaces formed by a binary stellar system.

Wind accretion

The Roche-lobe overflow in LMXBs is the preferred mass-transfer process leading to formation of accretion disc around the compact objects. However in HMXBs, a fraction of total mass loss from the companion OB star in the form of stellar wind is captured by the compact object due to its strong gravity. The stellar wind of massive OB type stars in HMXBs are very intense and highly supersonic. The typical mass loss rates from these stars can be as high as $10^{-6} - 10^{-5}$ $M_\odot$/yr with the wind velocities comparable to the escape velocities from the stellar surface:

$$v_{wind}(r) \sim v_{escape}(R_*) = \left(\frac{2GM_*}{R_*}\right)^{1/2}. \tag{1.4}$$

Now, assuming the compact star (i.e consider a neutron star) with orbital velocity v_{orb}, sweeping through the stellar wind of the companion star, accretes matter at a distance of *accretion radius* r_{acc}. This can be written as :

$$r_{acc} = \zeta \frac{2GM_x}{v_{rel}^2 + c_s^2} \simeq \frac{2GM_x}{v_{rel}^2}. \tag{1.5}$$

where $v_{rel} = \left(v_{wind}^2 + v_{orb}^2\right)^{1/2}$ is the relative velocity of neutron star with respect to the stellar wind, $c_s \sim 10\ km/s$ due to the typical wind velocities v_w of the order of $\sim$ 1000 km/s. Because of the supersonic nature of the stellar wind, a strong bow shock is formed at the accretion radius r_c from the neutron star. Given the orbital velocity of NS in HMXBs, $v_{orb} \sim 200$ km s^{-1} at $r = 2R_*$ and $v_{wind}(2R_*) \sim 1000 km\ s^{-1}$, the approximate distance at which the outflowing material from stellar wind gets channelled towards the neutron star is, $r_{acc} \sim 10^8 m$. Therefore, in case of stellar wind accretion, the mass accretion rate would be

$$\dot{M} = 4\pi\rho_0 v_{rel} r_a^2 = 4\pi \left(GM_{NS}\right)^2 \frac{v_w \rho_w}{v_{rel}^2} \tag{1.6}$$

Considering the total mass loss rate of the massive star as $-\dot{M}_w$ and the mass flow into the accretion cylinder of radius r_{acc} near the NS, we have the fraction of mass captured by the NS as (Frank et al., 2002):

$$\frac{\dot{M}}{-\dot{M}_w} \simeq \frac{r_{acc}^2 v_w(a)}{a^2 v_w(a)} = \left(\frac{GM_{NS}}{a}\right)^2 \frac{1}{v_w^4(a)}. \tag{1.7}$$

Here, a is the binary separation. For typical stellar parameters of NS X-ray binaries, the accretion rate, $\dot{M}$ given by equation 1.7 onto the NS is very less (i.e it is $10^{-4} - 10^{-3}$ times total mass loss rate of companion star). However, the observed X-ray luminosity from HMXBs accreting through the capture of stellar wind is of $\sim 10^{37}$ erg s^{-1} is mainly due to very high mass loss rate ($10^{-6} - 10^{-5}$ M$_\odot$yr^{-1}) from the companion OB stars. In other words, compared to Roche-lobe overflow, accretion through the capture of stellar wind is very inefficient process in powering the X-ray sources in binary systems.

1.4 Characteristics Properties of Neutron Stars

The theory of stellar evolution in 1930's postulated the neutron stars as one of the end products. However, it had been confirmed in 1960s with the discovery of pulsars (Hewish et al. (1968)). The first pulsar, discovered by Anthony Hewish and Jocelyn Bell, was found to be a radio source showing periodic and rapid time variations of

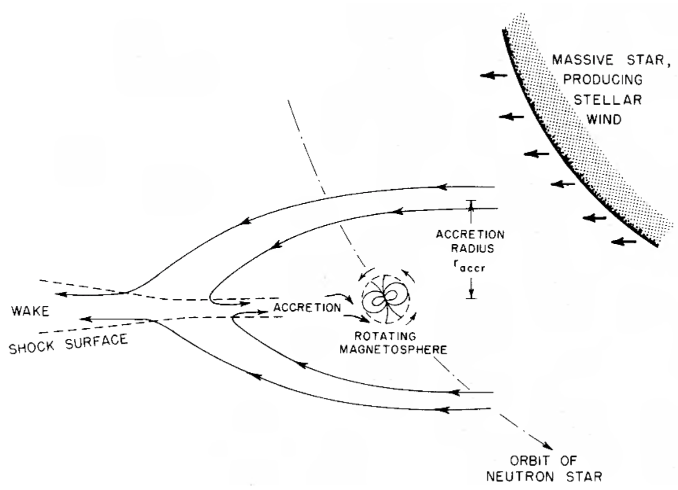

Fig. 1.3 Accretion through the capture of stellar wind from a massive star onto the neutron star in HMXBs. *Picture courtesy :* Davidson and Ostriker (1973).

1.33 seconds. These remarkable clock like radio pulses were alluded to be signals from extra-terrestrial civilization. However, these signals were later confirmed to come from a special class of stellar objects. They are rapidly rotating neutron stars whose existence had been predicted theoretically as early as in 1933 (Gold (1968)), but had not been observed until the discovery of pulsars.

When a massive star runs out of most of its nuclear fuel, it leaves off the normal stellar evolution. Neutron stars (NS) are one of the end products of this stellar life cycle. The gravitational collapse of a massive star's ($> 8\ M_{\odot}$) core results in a Type-II supernova leaving behind the central dense region. The matter present in these dense region is compressed to supra-nuclear densities. Hence, a $\sim 1.5 M_{\odot}$ NS is confined to a size of about 12 km radii. The mass range of neutron stars is limited to $3M_{\odot}$. The upper bound on the mass estimate of neutron star comes from the general relativistic considerations and lies in the range of $1.44 - 3M_{\odot}$. The lower bound, however, is obtained from the observations of binary pulsars. Along with the neutron stars, there are other two kinds of end products of stellar evolution such as white dwarfs and black holes, together called as compact objects.

Mass and Spin of Neutron Stars

A preliminary estimate of maximum mass of neutron star comes from the theoretical considerations that Landau used while deriving the maximum mass of white dwarfs as calculated by Chandrasekhar (Chandrasekhar, 1931). Miller and Miller (2015) assumed that the fermion degeneracy pressure (i.e neutrons star is mostly made of neutrons) hold up the dense and speherical structure of neutron stars. Then each of these fermions can be localized in a region $\Delta x \sim n^{-1/3}$, where n is the number density of fermions. Therefore, from the Uncertainity principle, the corresponding Fermi momentum (p_F) can be derived. Now in a non-relativistic case, the Fermi energy per fermion would be: $E_F \approx \frac{p_F^2}{2m_F} \sim 1/R^2$ and for relativistic degeneracy (i.e at $E_F \approx p_F c$), it would be $E_F \sim \hbar\, c[M/(\mu_F m_n R^3)]^{1/3} \sim 1/R$. Here the average number density of fermions is, $n \sim M/(\mu_F m_n R^3)$ in a star of total mass M and radius R mostly consisting of neutrons of mass mn. The gravitational potential energy per degenerate fermion is $E_g \sim -\frac{GMm_n\mu_F}{R}$. The total energy per degenerate fermion, as calculated by Miller and Miller (2015) for relativistic and non-reltivistic case, shows the dependence on mass, radius and μ_F as:

$$
\begin{aligned}
E_{tot} = E_F + E_g &= \frac{K_1 M^{2/3}}{\mu_F^{2/3} R^2} - \frac{K_2 M \mu_F}{R} \quad (Case\ I: non-relativistic) \\
&= \frac{K_3 M^{1/3}}{\mu_F^{1/3} R} - \frac{K_2 M \mu_F}{R} \quad (Case\ II: relativistic)
\end{aligned}
\tag{1.8}
$$

Using this, the minimization of energy for a stable configuration can be derived to $R \propto M^{-1/3}$ in the first case. This implies that the degenerate objects become smaller in size with increase in their mass. In the second case, $E_{tot} = 0$ at the limiting mass shows that $M_{max} \propto \mu_F^{-2}$. In case of neutron stars with $\mu_F \approx 1$, the maximum mass would be $\sim 5.6 \mathrm{M}_\odot$. This estimated value of maximum mass of NS, however, exceeds the realistic value. Due to the compactness of the neutron star, the factors contributing to mass energy relation other than the rest mass energy are significant. Hence, in order to obtain a stringer constraint on the maximum mass of NS, one has to resort to the equation of hydrostatic equilibrium for a spherically symmetric and non-rotating star in general-relativity. This has been considered in TOV (Tolman-Oppenheimer-Volkov) equation as:

$$\frac{dP(r)}{dr} = -\frac{G}{r}\left[\rho(r) + \frac{P(r)}{c^2}\right]\left[M(r) + 4\pi\, r^3 \frac{P(r)}{c^2}\right]\left[1 - \frac{2GM(r)}{rc^2}\right]^{-1} \tag{1.9}$$

Here, $M(r)$, Pr and ρr are the gravitational mass, pressure and mass-energy density of the star with in a radius r, respectively. Thus, given the $P-\rho$ relation, the maximum mass of the neutron star can be derived. However, the central density exceeds the nuclear saturation density ($\rho_s \approx 2.6 \times 10^{14} g\ cm^{-3}$) and unlike normal nuclear matter (which is nearly symmetric in distribution of neutrons and protons in a nuclei), the NS matter is strongly skewed towards the neutrons. Hence, it is diffcult to know $P-\rho$ relation from first principles. Interestingly, Rhoades and Ruffini (1974) came up with the idea that at higher density, the NS equation of state with maximum possible mass is the one in which the speed of sound is taken same as the speed of light (i.e $c_s = (dP/d\rho)^{1/2}$). Using this assumption to densities higher than ρ_s results in a maximum mass of $M_{max} \approx 3.2\mathrm{M}_{\odot}$ (Miller and Miller, 2015). Extending the equation of state to densities up to $2\rho_s$, (Kalogera and Baym, 1996) showed that the maximum mass drops to $2.9\mathrm{M}_{\odot}$. This criteria of maximium mass has been in use in X-ray astronomy to distinguish black holes from the neutron stars in a binary system. If in a X-ray binary system (see Section.1.2), the X-ray emitting object exceeds $3\mathrm{M}_{\odot}$, it is most likely to be a black hole than a neutron star. A list of neutron star masses with their uncertainities is given in Lattimer (2012) and it is maintained at the webpage (https://stellarcollapse.org/nsmasses) by Jim Lattimer. The spin periods of almost 2500 neutron stars are known from periodic intensity modulations. Among these, a majority of the neutron stars observed in radio band with periods ranging from few milliseconds to seconds (Manchester et al., 2005). Radio emission from these pulsars is thought to be originated from the observed spin-down of the neutron star. There are another class of neutron stars (nearly 200) that are bright in X-rays and have a spin-period distribution in the range of 1.7 ms - 3 hr. These neutron stars derive their energy by accreting matter from the binary

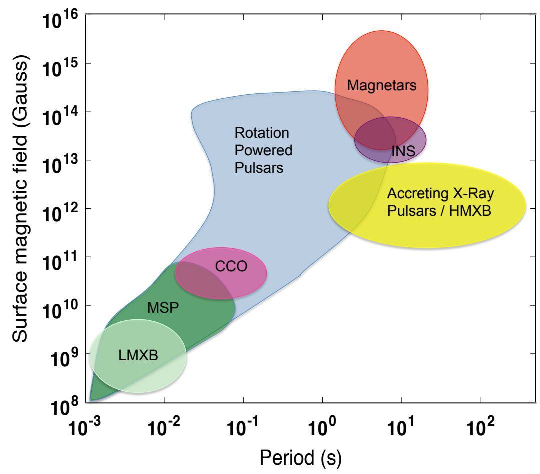

Fig. 1.4 A schematic representation of neutron star populations among various categories based on their period and derived values of surface magnetic field. The figure is taken from Harding (2013)

companion. These are known accretion powered pulsars. A detailed physcial picture of these type of sources will be discussed in the Section 1.6. Before venturing into the properties of these pulsars (which will be the subject of discussion in later sections), we will have a brief overview of neutron stars found in other astrophysical systems.

We have seen that the neutron stars are found in wide range of spin frequencies. They also possess highest magnetic fields comparable to any objects in the Universe. Based on the primary source of emission and depending on the spin period evolution, they are classified in various categories such as (i) Rotation-powered Pulsars (RPP), (ii) Anomalous X-ray pulsars (AXPs)/magnetars, (iii) isolated neutron stars (INS) and (iv) accretion-powered NSs. Based on the spin-period and estimated magnetic field strength, the population of these systems is shown in Fig. 1.4.

Rotation Powered Pulsars

Rotation-powered pulsars spin-down due to torques exerted from the magnetic dipole radiation and particle emission. This spin-down energy is being emitted in a broad energy range i.e. from radio to gamma-ray bands. These objects are discovered from the detection of pulsation in radio emission. Since the discovery of pulsar in 1967, more than 2000 radio pulsars with spin period in the range of a few ms to several seconds have been identified. At least 100 of these pulsars are also detected in X-ray band and more than 130 as Gamma ray pulsars Abdo et al. (2013). Occasional 'glitches' are seen in the spin down frequency of these pulsars though most of the time the spin-down rate is smooth and can be predicted. Among the two main classes of RPP, i.e *normal pulsars* and *milisecond pulsars*(MSP), the eariler ones have a characteristic ages of $\tau < 100\ Myr$ and the later have $\tau \geq 100\ Myr$. The RPPs have $< 10\%$ of their spin-down power in pulsed radiation whereas most of the power in pulsed emission is radiated in gamma rays (around a GeV).

Isolated Neutron Stars

These neutron stars emit mainly in soft X-ray band and are very faint in optical or UV emission. There are no observational evidences of association of these objects with any of the SNRs or nebulae. The X-ray spectra of these NSs are generally described with a soft blackbody component with temperature in the range of $0.04 - 0.1$ keV. These sources are less luminous with X-ray luminosity of $10^{30} - 10^{32}\ \mathrm{ergs\,s^{-1}}$. Presently, there are only 7 confirmed INS and are called as *The Magnificient Seven* (Harding, 2013). The six of these NSs show weak X-ray pulsations with periods in 3 s to 11 s range. Compared to CCOs, these periods are much longer. Most of these sources show spectral absorption lines in 0.3 - 1 keV range though the origin of these lines is not known. The X-ray luminosity of INS are higher compared to their spin down luminosity indicating that the rotation cannot be the possible cause of observed X-ray emission. In addition to these, the thermal luminosity and temperatures for INSs are way high for conventional cooling at their characteristic ages. This hints that the magnetic fields have decayed from their intial NS birth values.

Magnetars

In this class of NSs, the primary source or radiation is the energy stored in the magnetic field. The decay of ultra-strong magnetic field ($B > 10^{15} G$) results in the persistent X-ray emission and also high-luminosity X-ray bursts seen in these sources. These magnetars are further grouped in to *Anomalous X-ray pulsars* (AXPs) and *Soft Gamma-Ray Repeaters* (SGRs). The X-ray luminosity of these sources is about 100 times higher than the luminosity estimated from the spin-down rate. This indicates that the emitted radiation exceeds that of the magnetic dipole spin-down seen in RPPs. According to Duncan & Thomson (1992), some neutron stars generate huge magnetic fields through dynamo action soon after their birth in the supernova explosions. The ambipolar diffusion of magnetic flux from the NS core due to field decay on short time scales powers the magnetars.

Accretion in Neutron Star X-ray Binaries

The NSs residing in binary systems can accrete mass from the companion stars through the capture of stellar wind or Roche Lobe overflow of the companion. The resultant gravitational potential energy of the infalling matter does provide the energy of radiation observed in X-rays. The accretion torque provided by the matter drives the spin evolution of these systems. Much of the discussion in this thesis deals with the variety of phenomena seen in these kind of NSs in binary systems based on their accretion properties, magnetic field strength and X-ray emission.

1.5 Accretion powered X-ray Pulsars

Accretion powered X-ray pulsars are rotating neuron stars in binary systems along with a main sequence companion star. X-ray emission from these neutron stars is powered by accretion of matter from the companion star. The neutron stars residing in these binary systems are relatively young. The surface magnetic field strength of these objects lies in the range of $(1-10)\times10^{12}$ G (Kundt 1981; Taam and van den Heuvel (1986)). Such strong magnetic field affects the accretion flow closer (i.e at hundreds of of NS radii) to the neutron star. At this distance, the ionized accreted matter is funneled onto the NS magnetic poles by the field lines. A schematic view of an X-ray pulsar is shown in Fig.1.5.

The strong magnetic magnetic field of the NS exerts magnetic force on the incoming plasma. The region of influence of magnetic field on the accreting plasma

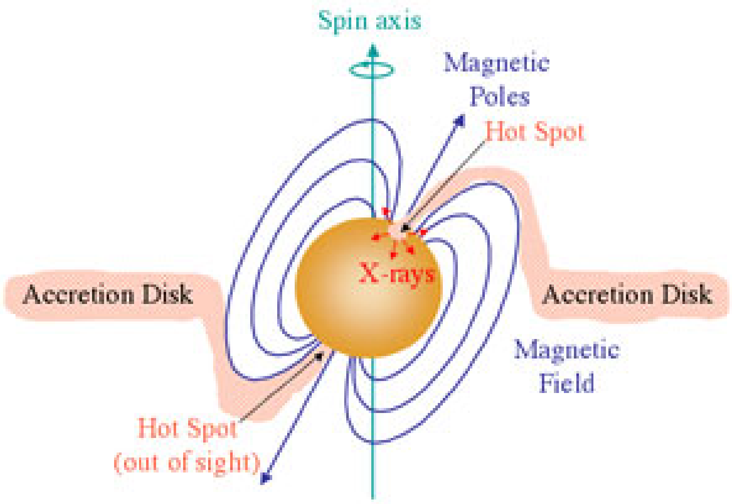

Fig. 1.5 Schematic view of an X-ray pulsar. Misallignment of the beam of X-ray emission from the hot spots at the magnetic poles and the spin axis of the neutron star causes the emission region into and out of view as seen by a distant observer. This causes pulsations in X-ray emission for a distant observer. Figure is adapted from http://astronomy.swin.edu.au/cosmos/X/X-ray+Pulsar.

is known as *magnetosphere*. The size and shape of the pulsar magnetosphere is determined by the manner in which the accretion flow near the NS surface interacts with the pulsar magnetic field. An estimate of the size of magnetosphere can be obtained by equating the ram pressure of accreting plasma with the magnetic pressure of the NS. Considering a dipolar magnetic field, the variation of field strength, B with radial distance r from the NS is roughly given as:

$$B \sim \frac{\mu}{r^3} \tag{1.10}$$

Here $\mu = BR_{NS}^3$ is the dipole magnetic moment of the NS at r = radius of neutron star R_{NS}. Hence, the magnetic pressure exerted by the NS at a radial distance r from the surface is

$$P_{mag} = \frac{B^2}{8\pi} = \frac{\mu^2}{8\pi r^6} \text{(in cgs units)} \tag{1.11}$$

As the accreting matter approaches the NS surface, the infalling gas gets disrupted at the magnetospheric boundary (i.e at magnetospheric radius or r_M, also called as *Alfven radius*) at which the ram pressure $P_{ram} = \rho v^2$ is superseded by the NS magnetic pressure. The velocity of the incoming gas is close to the free-fall velocity, $v \sim v_{ff} = \sqrt{\frac{2GM}{r}}$. Also writing the accretion rate $\dot{M}$ in terms of ρv as $\dot{M} = 4\pi r^2 \rho |v|$, we have

$$P_{ram} = \frac{\dot{M}}{4\pi r^2}\sqrt{\frac{2GM}{r}} \tag{1.12}$$

At $r = r_M$, setting $P_{mag} = P_{ram}$, we have the magnetospheric radius, r_M as

$$r_M = (2\pi/\mu_0)^{2/7}(2GM)^{1/7}\mu^{4/7}\dot{M}^{-2/7} \tag{1.13}$$

Writing the magnetic moment, μ in units of $10^{30}\ Gcm^3$ as μ_{30} and mass accretion rate, $\dot{M}$ in units of $10^{16}\ g/s$ as $\dot{M}_{16}$, we have

$$r_M = 5.1 \times 10^8 \dot{M}_{16}^{-2/7} M^{-1/7} \mu_{30}^{4/7}\ cm \tag{1.14}$$

It's convenient to express r_M in terms of accretion luminosity L_{acc} instead of $\dot{M}$. Assuming all the kinetic energy of the accreting matter at the NS site is converted into radiation, the accretion luminosity is given as :

$$L_{acc} = GM\dot{M}/R_{NS} = 1.3 \times 10^{36} \dot{M}_{16}(M/M_{\odot})(10\ km/R_{NS})\ erg/s.$$

With $L_{37} = (L_{acc}/10^{37})\ erg/s$, $R_6 = (R_{NS}/10^6)\ cm$, the value of r_M can be obtained by using the following expression,

$$r_M = 2.9 \times 10^8 M^{1/7} R_6^{-2/7} L_{37}^{-2/7} \mu_{30}^{4/7}\ cm \tag{1.15}$$

where the neutron star mass M_{NS} is expressed in terms of $M_{\odot}$ as $M = M_{NS}/M_{\odot}$.

For typical accretion luminosities seen in NS X-ray binaries, the magnetosphere gets extended up to a few 1000s of km from the neutron star surface. After the incoming plasma enters into the magnetosphere, it flows along the field lines to the NS surface. At the distances of r_M from the NS, its the type of accretion flow (i.e Roche-lobe overflow or stellar wind accretion) that determines the mechanism by which the accreting matter will enter into the magnetosphere.

1.5.1 Critical & Eddington Luminosity

In accretion powered X-ray binary pulsars, the accretion of matter from the companion star to the NS is the prime source of X-ray emission. Considering the accretion onto the NS to be spherical symmetric, the maximum luminosity that can be emitted is limited to the *Eddington luminosity*. This is obtained by balancing the radiation force acting on a electron-proton pair with the gravity acting on the pair due to the accreting object. The Thomson scattering cross-sections of the protons is smaller than the electrons by a factor of $(m_{\rm e}/m_p)^2 \cong 2.5 \times 10^{-8}$. As a result, the free electrons scatter more due to the radiation force. Assuming the Thomson scattering cross section over which the electron absorbs momentum $\sigma_T S/c$ from the outgoing radiation, we have the outward radiation force as $(\frac{\sigma_T}{c})(\frac{L}{4\pi r^2})$. Here, the luminsoity of the accreting source is L $(erg\ s^{-1})$. At the luminosity $L = L_{Edd}$, we have

$$\left(GMm_{\rm p} - \frac{L_{\rm Edd}\sigma_T}{4\pi c} \right) \frac{1}{r^2} = 0 \tag{1.16}$$

i.e $L_{\rm Edd} = 4\pi GMm_{\rm p}c/\sigma_T \cong 1.3 \times 10^{38} (M/{\rm M}_{\odot})$ erg s^{-1}.

As the accreting luminosity increases beyond the Eddington value, its expected that the accretion will halt due to excess of outward radiation pressure. For accretion powered sources, the Eddington limit L_{Edd} acts as a constraint on steady accretion flow. However, in case of accreting X-ray pulsars, the accretion is not spherically symmetric as the accreting matter is being channeled by magnetic field lines unto a fraction of the NS surface. The pulsar luminosity at these sites exceeds the Eddington limit. During giant X-ray outbursts from the transient Be/X-ray binary pulsars, the X-ray luminosity at the peak of outburst reaches close to or even higher than the Eddington luminosity. At such high luminosity, the radiation emanating from the magnetic poles of the neutron star could stop the incoming matter above the magnetic poles by forming a radiation-dominated shock. As a result, the structure of the accretion column begins to rise above the NS *hotspots*. This transitional luminosity at which the radiation pressure is sufficient enough to halt the in-falling matter reaching the NS surface is termed as *critical luminosity*, L_{crit} (Basko and Sunyaev, 1976; Mushtukov et al., 2015). An estimate of L_{crit} depends on the NS surface magnetic field (Mushtukov et al., 2015). The analytic expression of L_{crit} in terms of scattering cross-sections is given by Mushtukov et al. (2015) as:

$$L_{crit} = 4 \times 10^{36} \left(\frac{M/\dot{M}}{R_{\rm NS}/10^6\ cm} \right) \left(\frac{l_0}{2 \times 10^5 cm} \right) \frac{\sigma_T}{\sigma_{eff}} \mathrm{ergs\,s^{-1}} \tag{1.17}$$

where $R_{\rm NS}$is the NS radius, l_0 being the base length of accretion channel on the NS surface. σ_{eff} is the effective cross section due to Compton scattering in the strong magnetic field of NS surface.

1.6 Emission mechanism in accreting X-ray pulsars

In accretion powered X-ray pulsars the strong magnetic field ($10^{12} - 10^{13}$ G) of NS drives the accretion flow near the NS surface. This is independent of the accretion mechanism (stellar wind or disc accretion) through which the the mass of the companion star reaches the magnetosphere. As the matter approaches towards the NS, it interacts first with NS magnetosphere at $r \sim r_M$. At the magnetospheric radii the field lines start co-rotating with the NS and thus exerting magnetic pressure on the incoming plasma. Due to intense magnetic stress, the matter cannot move across the field lines. Rather it freezes with the dipole field lines and channels along these unto the stellar surface. Near the NS surface, the matter is funneled unto the polar caps. As the infalling material strikes the surface, it releases some of its kinetic energy in heating the NS. In order to produce the X-ray luminosity of 10^{37} $\mathrm{ergs\,s^{-1}}$ the surface temperature reaches upto 10^7 $\deg K$. At this temperature the soft X-rays are produced. These soft X-ray photons propagate upward in the accretion column and interact with the in-flowing plasma (having speeds $\sim 0.5\ c$). The Comptonization of these soft X-ray seed photons in the column results in high energy X-ray emission from the pulsar. The beaming of this column emission from the magnetic poles rotates through our line of sight whenever there is a misalignment between rotation and magnetic axis. As a result this, the observed emission is manifested as pulsations from these accretion powered sources. Depending upon the rate of inflow of mass (and hence luminosity) the height of the accretion column changes. The different ways through which the the plasma is decelerated near the NS poles leads to different emission geometries (as discussed below).

1.6.1 Accretion regimes in X-ray pulsars

The emission beam pattern in X-ray pulsars depends on several factors such as structure of accretion column, the accretion column height above which a radiation dominated shock forms, the strength of the NS magnetic field and the accretion luminosity of the pulsar. In high luminous X-ray pulsars ($L_x \sim 10^{37-38}\,\mathrm{ergs\,s^{-1}}$), as the accretion flow stops via a radiation dominated shock at a certain height above the accretion column, the escaping radiation diffuses through the column walls resulting in a fan-beam emission pattern. Whereas below the radiative shock, the accretion flow settles down subsonically. The critical luminosity is also helpful in distinguishing the accretion powered pulsars in two distinct classes, namely: *super-critical* sources emitting at luminosity $L_x \gtrsim L_{crit}$ and *sub-critical* sources with $L_x \lesssim L_{crit}$. In the super-critical sources, the height of the accretion column begins to rise due to radiative shock formation. In the shock region, the radiation pressure is higher than the ram pressure of accretion flow. So, the infalling matter decelerates beyond the shock height. Above the shock region the kinetic energy of the incoming matter is lost into the scattered radiation. However below the radiative shock region down to base of accretion column the X-ray photons escape through the walls of accretion column in a fan-beam emission as shown in Fig. 1.6

In the sub-critical sources, the accreting matter is brought to rest onto the NS surface thorough Coulomb interactions near the base of accretion column (Burnard et al., 1991). It's due to fact that in these sources the radiation pressure is not strong enough to decelerate completely the accreting matter which initially passes through a radiation dominated shock (Becker et al., 2012). The *critical* luminosity plays a vital role in distinguishing the two accretion regimes in accreting X-ray pulsars. For the given strength of surface magnetic field, the physical models developed by Becker et al. (2012), show a clear correlation of cyclotron line energy (E_{cyc}) and X-ray luminosity (L_x) in pulsars accreting in super-critical and sub-critical accretion

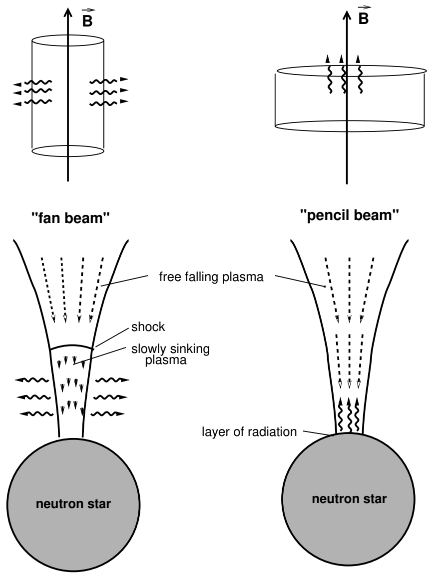

Fig. 1.6 Two different accretion geometries in NS/X-ray binaries and the corresponding pulsar emission beam pattern, *Left:* "fan beam emission" due to "cylindrical geometry" of accretion column and *Right:* " pencil beam emission" pattern due to " slab geometry of accretion column. This figure is adapted from Schönherr et al. (2007).

regimes. In the group of accretion powered pulsars in which $L_x > L_{crit}$, (i.e in their super-critical accretion regime), there is a negative correlation between cyclotron line energy and luminosity. Whereas, the sources in sub-critical regime with luminosities $L_x \leq L_{crit}$ show a positive correlation between L_x & E_{cyc}. Based on the dynamics of radiation pressure and Coulomb interaction or gas pressure in accreting X-ray pulsars, Becker et al. (2012) express the critical luminosity in terms of NS parameters as:

$$L_{crit} = 1.28 \times 10^{37}\,\mathrm{erg\,s^{-1}} \left(\frac{\Lambda}{0.1}\right)^{-7/5} w^{-28/15} \times \left(\frac{M_{NS}}{1.4M_{\odot}}\right)^{29/30} \left(\frac{R_{NS}}{10\,\mathrm{km}}\right)^{1/10} \left(\frac{E_{cyc}}{10\,\mathrm{keV}}\right)^{16/15} \tag{1.18}$$

Here, E_{cyc} is the observed cyclotron line energy related to NS magnetic field through equation 1.22. The constant $\Lambda = 1$ for spherical accretion and $\Lambda < 1$ for disk accretion. For typical values of NS parameters with $\Lambda = 0.1$, and $w = 1$ the above expression in terms of NS magnetic magnetic field (B_{12} in units of 10^{12} G) reduces to

$$L_{crit} = 1.49 \times 10^{37} \,\text{erg sec}^{-1} B_{12}^{16/15}$$

.

1.6.2 Phenomenological Spectral Models

The X-ray spectra of accreting pulsars are often fitted with various functional forms. These functions are characterized in terms of a power-law distribution in energy. In case of accretion powered X-ray pulsars, the power-law photon index Γ varies in the range of 1–2. One of the widely used empirical model to fit the pulsar spectrum is power law with an exponential cutoff at higher energy *HighECut* (White et al., 1983). Analytically, this can be expressed as:

$$\text{HIGHECUT}(E) = A\, E^{-\Gamma} \times \begin{cases} 1 & (E \leq E_{\text{cut}}) \\ \mathrm{e}^{-(E-E_{\text{cut}})/E_{\text{fold}}} & (E > E_{\text{cut}}) \end{cases} \tag{1.19}$$

In the above expression, E_{cut} and E_{fold} are respectively the cutoff and folding energies in units of keV and Γ denotes the power-law photon index. The normalization, A is in $photons\ keV^{-1}\ cm^{-2}\ s^{-1}$.

Using the Fermi-Dirac form of high energy cutoff with the power-law function, (Mihalas and Winkler, 1986) proposed a new continuum model which can be written as

$$\text{FDCO}(E) = A\, E^{-\Gamma}\, \frac{1}{1+\mathrm{e}^{(E-E_{\text{cut}})/E_{\text{fold}}}} \tag{1.20}$$

In order to describe the broad-band pulsar spectrum obtained from *Ginga*, another continuum model which generalizes the above single power-law model, known as Negative and Positive EXponential (*NPEX*) was formulated (Mihara, 1995). The analytical form of this model consists of a double power-law function with a single exponential cutoff at higher-energy.

$$\text{NPEX}(E) = (A_1\, E^{-\Gamma_1} + A_2\, E.^{+\Gamma_2})\, \mathrm{e}^{-E/E_{\text{fold}}} \tag{1.21}$$

Here, $E_{\rm fold}$ represents the typical plasma temperature (kT) of the X-ray emitting source. The parameters A_1&A_2 denote the normalizations of the two power-law components. Γ_1 and Γ_2 are the indices of the positive and negative power-laws, respectively. A physical interpretation of the NPEX model lies in the fact that in a plasma temperature, T, it resembles the photon spectrum due to unsaturated thermal Comptonization (Sunyaev and Titarchuk, 1980).

Cyclotron lines

X-ray binaries containing highly magnetized accreting neutron star show absorption line like features in their hard X-ray spectra. These features are also called as Cyclotron Resonance Scattering features (CRSFs) which are formed near the magnetic poles of the NS. At these sites, due to intense magnetic field of the pulsar ($\sim 10^{12}$ G), the motion of electrons perpendicular to the magnetic field is quantized in Landau orbits. As the X-ray photons with energy equivalent of these quantized electrons resonantly scatter off from the discrete Landau levels, an absorption like feature is seen in the X-ray spectrum of the pulsar. The energy difference between the Landau levels is related to the NS magnetic field through the expression:

$$E_{cyc} = 11.58\ \mathrm{keV}\left(\frac{B_{NS}}{10^{12}\mathrm{G}}\right) \tag{1.22}$$

Therefore, from the observational evidence of CRSF features in the X-ray spectra, the magnetic field of the accreting magnetized NS can be inferred directly. Her X-1 is the first X-ray pulsar in which a cyclotron line near ~ 58 keV is detected in 1976 (Truemper, 1978). Thereafter in a number of X-ray pulsars (almost 30), the CRSF features have been detected (Caballero and Wilms, 2012; Jaisawal and Naik, 2017) . In the vicinity of strong gravity of NS, the CRSF features are red shifted. Taking into account the redshift $1.25 < z < 1.4$ for typical NS parameters, the observed cyclotron line energies are corrected as $E_n = nE_{cyc} = (1+z)E_{n,obs}$. Here, n denotes the harmonics of fundamental line energy due to occurrence of CRSF line features at the multiples of E_{cyc} in few X-ray pulsars such as 4U 0115+63 (Boldin et al., 2013), V 0332+53 (Pottschmidt et al., 2005) etc.

Emission of $Fe\ K_{\alpha}$ line

The X-ray spectrum of some HMXBs consist of additional features above their usual broad-band continuum. Among these, the prominent feature is the FeKα fluorescence line emission in soft X-rays ($\sim 6.4\ keV$) produced by neutral iron atoms. As the Fe atoms present in accreting matter gets illuminated by X-ray photons with sufficient energy ($E > 7.2\ keV$), an inner K-shell electron is knocked out from the Fe atom. This K-shell vacancy is filled by adjacent electron from the L-shell with the transition producing the $Fe\ K_{\alpha}$ emission in X-rays. The origin of 6.4 keV iron line emission thought to be originated from possible sites such as in the accretion disk around the NS, the shock fronts or accretion wakes in which the stellar wind gets stagnated. Apart from this the reprocessing of accretion matter trapped with in the NS Alfven shell is also a possible candidate for $Fe\ K_{\alpha}$ line emission. The ubiquitous presence of these lines in HMXBs is due to their production in the stellar winds of massive stars. On the other hand the lack of Fe lines in the X-ray spectra of LMXBs could be due to their donor stars insufficient stellar wind (Torrejón et al., 2010). The line intensity variations are also a good indicator of matter distribution around the pulsar. Apart from FeK-α emission from neutral iron atoms, the 6.7 keV iron line from the H-like iron atoms (due to radiative recombination) and Fe K-absorption edge (near 7.2 keV) are also been observed in the stellar winds of Vela X-1 (see Nagase, 1989, and references therein).

1.7 Motivation for present thesis

The X-ray intensity variabilities associated with the BeXB pulsars have always offered us opportunities to understand these systems better. The timing and spectral studies of these sources provided a rich phenomenology with several speculations. Among these, the understanding of geometry of pulsar accretion column and matter distribution in the vicinity of the neutron star remains a daunted task. Even though the polar emission of the pulsar (mostly in X-rays) studied at different source luminosities at different phases of regular Type I and rare Type II X-ray outbursts, an in-depth understanding of these emission structures and their possible co-existence or transition from one form to other requires further investigation. Previous studies of BeXB pulsars were often confined to a particular outburst epoch (i.e it may be a Type I or Type II outburst) of the pulsar. But an investigation of pulsar properties in finding the commonalities across different types and phase of outbursts at similar source luminosities has never been carried out extensively before. With an aim to explore various emission properties of the BeXB pulsars across wide range of source luminosities during Type I and Type II outbursts events, the present thesis helps in bridging the gap in our understanding these sources. A detailed spectral and timing studies of the properties of the BeXB pulsars at different phases of rarely observed giant outburst and regular periodic outbursts provide a rare opportunity to probe the emission regions near the pulsar. Though the regular periodic X-ray outbursts in BeXB pulsars are known to be due to capture of matter from the equitorial circumstellar disk of the Be star at the periastron passage of the neutron star, the origin of rare giant X-ray outbursts in these systems are not well understood. The primary cause for this is extremely rare occurrence of such outbursts (once in a few decades) in these BeXB systems. Therefore, comparing the characteristic properties of the pulsars during different type of X-ray outbursts and at different luminosities can provide important information on the understanding of the origin of these X-ray outbursts. It also helps in better understanding the complex astrophysical physical processes happening near the neutron star site.

The complex pulse shapes of BeXBs have shown strong luminosity and energy dependent absorption dip like features. Phase resolved spectral studies of these features revealed that partial obscuring of X-rays by the matter that is rotating in phase with the pulsar leads to such absorption features in the pulse profiles (Paul and Naik, 2011). However, a follow up of these dip like features in the pulse profiles in a broad luminosity range of pulsar would be helpful in investigating the cause of such features. Many a times, it happens that, the X-ray properties of these pulsars are explained from a single pointed observations of the source. This is sufficient to find the spectral state of the pulsar at those epochs. However during the accretion time scale, the X-ray pulsars undergo rapid changes in the emission behaviour. To understand time dependent changes in the pulsar, it is important to study the spectral and timing properties of the pulsar during different evolutionary stages of the X-ray outburst and also low luminosity quiescent phases. Hence, an important task of the present work is to probe and compare such long term properties of the pulsar spanning many years to have a better understanding of the mechanism of X-ray emission during different types of outbursts and quiescent phase of the neutron star in the BeXBs.

1.8 Thesis Outline

The emission from the NS accretion column in BeXB pulsars is quite complex. The variation in emission patterns seen from various pulse profile patterns suggest various emission geometries at the base of accretion column. In BeXBs during outbursts, the luminosity dependent changes in the accretion column emission is evident from the timing and spectral studies. In the present thesis, a long term X-ray variability study of BeXBs is carried out to understand these changes in the column emission in wide range of luminosity. The spectral study of BeXBs covering many type-I and a type-II outbursts (i.e for EXO 2030+375) is done extensively using decades of monitoring observational data from *RXTE* satellite. These studies also probe the different accretion regimes in the BeXBs and their dependence on pulsar luminosity.

The first chapter of the present thesis provides an overview of X-ray binaries. The timing variabilities associated with BeXBs such as Type-I and Type-II outbursts are discussed. The various empirical continuum models that are used in fitting the broad-band spectra of BeXBs are also discussed. The different mechanisms by which mass accretion onto the neutron star proceeds in HMXBs and LMXBs is also illustrated briefly. The role of critical luminosity in distinguishing the accretion regimes of the pulsar, spectral properties of BeXBs during outbursts, cyclotron line features in the spectra, emission of Fe-Kα, the luminosity dependence of the pulsar emission beam pattern etc. are encapsulated to understand the spectral and timing properties of few BeXBs during outbursts.

In the second chapter, the X-ray observations of Be/X-ray binary pulsars that are used in the present thesis is catalogued. The instruments on-board various X-ray observatories from which the data has been found useful for the present work, are briefly described. This chapter also discusses the basic X-ray data reduction and analysis procedures that are employed in analyzing the data obtained from BeXBs.

In the third chapter, the timing and spectral properties of the transient BeXB pulsar KS 1947+300 has been studied using its 2013 giant outburst observations as seen by *Suzaku*. The broad-band spectrum of the pulsar showed that an emission component in soft X-rays is pulsating in phase with the pulsar. The origin of this feature is probed using phase-resolved spectral studies.

The basis of fourth chapter is an effort to understand the emission properties of X-ray pulsars from its various patterns of X-ray variabilities. To pursue this we have used the decades of *RXTE* observations of BeXB pulsar EXO 2030+375. The X-ray emission from this pulsar spanned almost two orders of magnitude ($i.e. 10^{36} - 10^{38}\,\mathrm{ergs\,s^{-1}}$) among various phases of its numerous Type I and a Type II outbursts. The pulse profiles and the broad-band spectra obtained at different source luminosities gave us an opportunity to understand the various emission geometries of the pulsar.

In the fifth chapter, for the first time we employ a physical model to the spectra of EXO 2030+375 to understand the column emission from the pulsar at different pulsar luminosities. Based on these long term spectral studies we find the evidence of critical luminosity regimes in the pulsar.

Finally, in the sixth chapter, a brief conclusion of the work carried out in the present thesis is presented. The importance of similar line of study for other BeXB sources and its future scope is also mentioned briefly.

Chapter 2

X-Ray Observations & Data Analysis

2.1 X-ray Observations

X-ray observations of cosmos from the surface of the earth is a formidable task. It is mainly because of the earth's atmosphere being opaque to X-rays. The main components of the atmosphere that are responsible for absorption of X-rays from sources in the sky are namely water vapor, carbon dioxide and ozone. The 480 km thick atmosphere of earth acts strangely. The high-energy radiation from Sun and other extra-terrestrial sources is augmented but the optical band of the electromagnetic spectrum in 400-700 nm and the radio band ranging few centimeters to 10s of meters could transmit through the thick atmosphere of earth. Hence to have a glimpse of the universe in X-rays and gamma-rays, corresponding telescope and detector systems have to be placed above the atmosphere of earth.

2.2 X-ray Telescope

The key issues behind the realization of an X-ray telescope to be flown to space are (i) the methods by which the X-rays from the cosmic sources could be captured and (ii) how an X-ray image of the cosmic source could be constructed from the incident X-rays on the telescope. X-ray photons can easily penetrate through matter if incident normally on the detector material. They may be absorbed in the thick detector material. Therefore, in order to focus a parallel beam of X-rays at the focal plane of the detector, the physical process such as total external reflection of X-rays has been explored. At grazing incidence on the metal surface, the X-ray photons get reflected obeying the laws of optical reflection (i.e angle of incidence is same as the angle of reflection). For the X-ray energies E far off from the absorption edges of reflecting material, the critical grazing incidence angle is related to atomic number (Z) of material and E as $\theta_c \propto \frac{\sqrt{Z}}{E}$. Hence to have larger critical angles for wide range of X-ray energies, high Z materials such as gold, platinum and iridium are used as the reflecting surfaces. These materials also reflect high energy X-ray photons for a given grazing incidence. However, above the energies of atomic edges of reflecting material and at larger angle of incidences, the X-ray photons pass through the metal surface. So, to achieve reflection of X-rays at these energies, several layers of mirrors could be sought. This arrangement in principle leads to a constructive interference of X-rays from nested mirrors .

X-ray imaging of extended sources such as supernova remnants, galaxies and galaxy clusters is not possible from the grazing incidence on a single X-ray mirror as they suffer from coma. Although such single mirror system can focus the X-ray photons, true imaging of X-rays could not be achieved. In 1952, a configuration of two mirror systems is proposed by Hans Wolter to image an X-ray source extending over a finite field of view (FOV). Generally in a Wolter configuration of mirrors, the basic principle is that the optical path length of all incident X-ray photons on the telescope should be identical to form an image of the source. Of the three possible configurations of mirrors illustrated by Wolter (1952a,b) such as Type-I, II & III, the Type-I geometry has been widely used in X-ray astronomy. The Type-I Wolter optics consists of an elliptical or parabolic mirror (from which the X-rays reflect off the concave surface) followed by an hyperbolic mirror (from which again the X-ray photons get reflected off the concave or convex surface) to reduce the effective focal length of the telescope and to achieve the higher aperture to focal length ratio. In X-ray telescopes, the use of this kind of optics along with the arrangements of nested mirrors in concentric shells also increases the total aperture of the telescope. Hence the total collecting area can be maximized without increasing the focal length

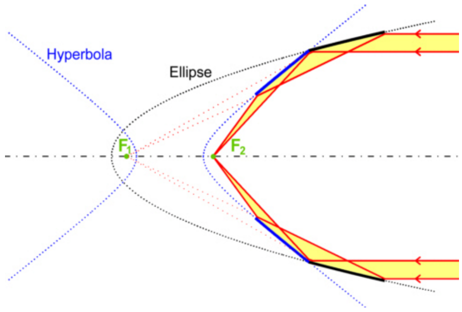

Fig. 2.1 Schematic arrangement of a Wolter Type-I mirror used in X-ray telescopes. The incident parallel X-ray photons from the distance source get reflected by the elliptical/parabolic mirror to focus at F_1. This also happens to be one of the focus of hyperbolic mirror from which further reflection causes the X-rays to focus at F_2. An X-ray image is formed at F_2 with the effective focal length increased by second reflection. Source:http://www.x-ray-optics.de

(or diameter) of the X-ray telescope. A schematic view of Type-I Wolter optics arrangement of X-ray mirrors is shown in Figure 2.1.

X-ray focusing telescopes with grazing incidence of X-rays in Wolter type-I optics are found useful in studying the non-solar X-ray sources. Compared to the conventional collimators used in studying the astronomical sources in other wavelengths, the X-ray focusing telescopes can accomplish higher spatial and spectral resolution using dispersive techniques (Giacconi et al., 1968). This helps in X-ray source localization as well as its structure can be studied in detail.

2.3 X-ray Detectors

The importance of X-ray detectors on-board every X-ray observatory lies in their capability to register the information of incident X-ray photons on the detector from various X-ray sources. The detection of X-ray photons is, however, is an indirect process. At first the incoming photons interact with the detector material to generate electrons and positively charged ions. The ionization process by these electrons within the detector leads further effects which can be converted into electrical signal for later retrieval and analysis. The four basic parameters of an X-ray photon that could be recorded from the detector are the photon energy, the arrival time of the photon, the number of incident X-ray photons and their position in 2D configuration plane of detector. As it is envisaged that an efficient X-ray detector on-board any

X-ray observatory (i) should have high spatial resolution over a large detector area, (ii) should be able to process the large photon flux with best temporal resolution, (iii) energy resolution should be good enough over a wide band of X-ray energy with the quantum efficiency close to unity and (iv) the internal background noise should be substantially low with a stable output for few years. While orbiting around the earth, it should remain unaffected from the energetic charged particles present in radiation belt. Ideal detector specifications would require that the detector should function with minimum power consumption and no other loss of resources that it should have simple, light weight and easy to build structure with a low output data rate (Fraser, 1989). Having such a detector is practically impossible. The detectors used in X-ray satellites such as *RXTE*, *Suzaku*, *Swift*, *NuSTAR*, *AstroSat* have been tuned to carry out specific tasks more efficiently to achieve desired science goals.

In the present thesis, timing and spectral data for several X-ray pulsars have been used from various instruments on-board some of the present and past satellites such as *RXTE*, *Suzaku*, *Swift*, *NuSTAR*. The characteristic properties and important features of X-ray telescopes and onboard detectors are briefly described in the following sections.

2.4 Rossi X-ray Timing Explorer (1995 - 2012)

The X-ray satellite *RXTE* was operational in space for about 17 years (from 1995 to 2012). During its active phase of operation, *RXTE* had observed a large number of X-ray sources such as black holes, neutron stars, white dwarfs, X-ray pulsars, galaxies and cluster of galaxies etc., producing huge number of significant and path-breaking results. Data from this observatory have been extensively used by researchers from various countries. Pointed observations from *RXTE* were also used in understanding the properties of Be/X-ray binary pulsars during outbursts, which is a part of the present thesis. In the following sections, properties of two main X-ray instruments onboard *RXTE* are briefly described.

Fig. 2.2 The Rossi X-ray Timing Explorer (*RXTE*) satellite, Source:https://heasarc.gsfc.nasa.gov/Images/xte/xte_spacecraft.gif

2.4.1 Proportional Counter Array (PCA)

The *RXTE/PCA* is an array of 5 proportional counter units (PCUs) with a large total collecting area of $\sim 6500 cm^2$ and sensitive in 2 - 60 keV energy range. Each of the PCA detector was assembled with a mechanical collimator. The presence of large number of identical hexagonal tubes in each of the collimators provided a field of view of $\sim 1^\circ$ (FWHM). Besides the collimator, there are two aluminazied mylar windows, a propane filled "veto" volume and the second window main volume with a mixture of Xenon & Methane by 90% and 10% compositionJahoda et al. (1996). Five layers of anode wire grids run through these volumes to carry the information of X-ray events recorded in the detectors. In the propane "veto" volume (VP) of top layer, all the propane anodes are connected. Subsequent 3 layers are the Xenon cells, each partitioned to two equal halves. The alternate cells from these layers are connected to amplifier chains to the "right" or "left". This forms six signal chains as XL1, XR1, XL1, XR2, XL3, XR3. Below these Xenon layers is the Xenon veto layer (VX) i.e the outermost anode. The top propane veto layer and bottom Xenon veto layer were used to discriminate whether the detected signal is due to a high energy photon impinging on the detector or any energetic particle entering side ways. During observation of X-ray sources, data were collected from one or multiple PCUs based on the number of PCUs that were kept ON during the observation, the position of source relative to the Sun and other detector configurations. The data were also collected from different detector combinations, allowed by the electronic data system (EDS) onboard the satellite to meet scientific goals of each X-ray observation. The 5 PCUs from which the data were labelled as PCU0 through PCU4. The X-ray data from PCU0 was not available after 12 May 2000 due to loss of propane.

2.4.2 High Energy X-ray Timing Experiment (HEXTE)

The HEXTE onboard the *RXTE* satellite was capable of detecting X-ray sources in the energy range of 15 – 250 keV. It is a system of eight phoswich scintillation detectors equally divided in two clusters (i.e. Cluster-A & Cluster-B). Each of these detectors was made up of two volumes of NaI(TI)/CsI(Na) crystals which distinguished source X-ray events from the particle background events in the following way. In the NaI crystal, the X-ray photons produce scintillation whereas the particles can from scintillation effects in both the NaI & CsI crystals. In the photo-multiplier tube, the scintillation from both the crystals show different rise times. This helps in distinguishing the events caused of source X-ray photons. The cleaned events from NaI crystal which survive the rise-time rejection criteria are further subjected to pulse-shape and pulse-shape analysis. The collimators attached to each detector comprise a honeycomb structure of hexagonal tubes that help in achieving a FOV of $\sim 1^{\circ} FWHM$ and full width zero intensity (FWZI) at 2.2°. During normal operations of HEXTE, the Cluster-A and Cluster-B rock on and off the target X-ray source which allows to collect the source and background data. During pointed observation of a source of interest, the two clusters with their rocking axis kept orthogonal, record X-ray background fields four times (two per cluster) by changing positions. Hence, the data collection from these clusters is also synchronized to cluster rocking with the data boundaries occurring at the change of cluster position. The default rocking period was set to 32 sec. However, other rocking intervals that could be set were 0 s, 16 s, 64 s and 128 s. On 2006 October 20, the HEXTE Cluster-A stopped rocking on and off the source position. Hence, it was fixed permanently in the on-source position by the instrument team [1]. The observations made by HEXTE are stored as FITS data files in two formats, namely Science Array (SA) and Science Event (SE) format although the same data sets are configured to five different modes of packaging [2]. Among these, the event list mode facilitates the timing information of each event survived after rejecting the background and passed through other discriminators. The recipes for reduction and analysis of HEXTE data, as illustrated by RXTE Guest Observer Facility [3], are found useful in data reduction and analysis of HEXTE data of BeXBs presented in this thesis. The characteristics of PCA and HEXTE are given in Table 2.1.

2.5 Suzaku (2005 - 2015)

The X-ray astronomy satellite *Suzaku* (ASTRO-EII), Japan's 5th X-ray satellite, was operational in space from 2005 to 2015. The broad energy coverage from soft X-rays (0.1 keV) to gamma rays (600 keV) was the unique capability of *Suzaku* that was very much useful in wide band spectroscopy of compact X-ray sources, AGNs, evolution of galaxy clusters, dynamics of plasma in stellar X-ray sources etc. Also the studies related to accretion phenomena around black holes, neutron star and white dwarf binaries were carried out from decade long scientific observations with *Suzaku*. It was developed by $ISAS/JAXA$ in collaboration with NASA and other Japanese & US institutions. Among the payloads carried by *Suzaku*, there was a hard X-ray detector system and rest five are soft X-ray telescopes. There were five detectors at the focal point of five X-ray telescopes (XRT). Four of these detectors were XIS (i.e X-ray imaging spectrometers, explained briefly in Section-2.5.1) and the fifth one was a high resolution X-ray spectrometer (XRS) . The XISs were suitable to study sources in soft X-rays i.e. in the energy range of 0.1–10 keV with an energy resolution of 120 eV at 5.9 keV. The XRS was non-operational after 2005 July 29 as there was a premature loss of liquid-He cryogen (coolant) due to a design flaw in the

[1] https://heasarc.gsfc.nasa.gov/docs/xte/whatsnew/newsarchive_2006.html#_hexteA-norock
[2] https://heasarc.gsfc.nasa.gov/docs/xte/abc/hexte_issues.html#struc_struc
[3] https://heasarc.gsfc.nasa.gov/docs/xte/recipes/hexte.html

Fig. 2.3 A schematic view of Suzaku satellite

interface of XRS dewar/spacecraft (see *suzaku-memo* [4]). The scientific capabilities of XIS and hard X-ray detector (HXD) remain unaffected from the loss of cryogens in the XRS. A schematic view of *Suzaku* is shown in Fig. 2.3.

2.5.1 X-ray Imaging Spectrometers (XIS)

The X-ray Imaging Spectrometer (XIS, Koyama et al. (2007)) contains four X-ray sensors (namely, XIS0, XIS1, XIS2 & XIS3) with CCD (i.e Charge Coupled Devices) chips in each of them. Among these, the sensors XIS-0, 2 & 3 were front-illuminated (FI) and XIS-1 was back-illuminated (BI). Due to a gate structure of thin Si and SiO_2 layers on the front side of FI CCDs, these were less sensitive to soft X-rays compared to XIS-1. CCDs present in each of the XISs were MOS-type semiconductor devices working in photon-counting mode where the arrival times, position and energy of individual X-ray events within XIS can be registered separately. This provided the XIS its ability to carry out X-ray imaging and spectroscopic studies in 0.1 – 12 keV energy range with an energy resolution of 120 eV. Each X-ray telescope with its 1024×1024 pixeleted CCD has an imaging area (IA) of size 25 $mm \times 25$ mm provided a coverage of $18' \times 18'$ region of the sky. The specification of all the XIS CCDs are given in Table 2.1

[4] http://www.astro.isas.jaxa.jp/suzaku/doc/suzakumemo/suzakumemo-2006-38.pdf

Fig. 2.4 Suzaku-XIS
Source:http://space.mit.edu/XIS/pics

The variety of observation modes were available for XIS sensors. Of these, the clocking mode was the default mode and used during most of the observations. The clocking mode governed the ways with which the CCD pixels should be read out. With its $\mu-$code and a voltage clocking pattern for CCD exposure and charge transfer, the clocking mode allowed either full, partial or stacked read from exposed CCD pixels. Based on these, there were two major clocking modes: the Normal mode and the P-sum mode. The normal mode was for CCD read out with a timed exposure. However, with the different read out options available such as window option (i.e partial readout in space), burst option (partial readout in time) or both (partial read put in space and time), the Normal clocking mode was suitable for carrying out time sequence of exposure, transfer of charge in frames, readout and storage to the Pixel memory. The P-sum clocking mode was for stacked readout of pixels and was functional for XIS-3. In this, the pulse height information from 128 rows of 1024×1024 pixelated CCD are stacked into a single Y direction. Because of this, the spatial information was lost in Y-direction. So in its place, the timing information of photon arrival was retained at a resolution of 7.8 *ms*. The data from different editing modes ($5\times5, 3\times3, 2\times2$, timing) specifying the telemetry format of the X-ray events observed by XIS CCD can be added as per the combinations allowed by the instrument team (see Table 7.5 of Suzaku technical description [5]).

2.5.2 Hard X-ray Detector (HXD)

The Hard X-ray Detector (HXD) onboard *Suzaku* was sensitive to observe X-ray sources in high energy ($10-600\ keV$) ranges. Unlike XIS (having X-ray imaging capability as described in Section 2.5.1), the HXD detector was a non-imaging instrument. It allowed the X-ray band pass of *Suzaku* to highest possible energies to have a broad-band study of celestial X-ray sources. The 16 main detectors of HXD are arranged in an array of 4×4 with active shielding provided by 20 crystal scintillators around them. In each detector unit, there were four GSO/BGO phoswich counters and four PIN silicon diodes facing a GSO scintillator in front. The PIN silicon diodes could detect X-ray photons up to 70 keV with an energy resolution of $\sim 3.0\ keV$. The GSO/BGO counters were capable of detecting X-ray photons with energies above 30 keV at an energy resolution of $7.6\sqrt{E}\%(FWHM)$ where the photon energy, E is measured in MeV.

PIN Silicon diodes

The PIN silicon diodes have an effective are of $\sim 16.5\times16.5\ mm^2$ maintained at a temperature of $-15\pm3^\circ\ C$ to reduce electrical noise. As the X-rays incident on the HXD, the PIN diodes absorb part of the energy of X-ray photon (i.e up to 70 keV) through photoelectric effect but were transperent to photons with energies higher than this. Subsequently, the hard X-ray photons reach the GSO detectors and registered there. The X-ray radiation detected in PIN diodes was amplified by the detector electronics and was amplified and converted to digital form for read out. To reduce the contamination from cosmic X-ray background and particle events, the PIN diodes were placed with in well-type BGO collimators.

[5] https://heasarc.gsfc.nasa.gov/docs/suzaku/prop_tools/suzaku_td/node10.html#SECTION00102000000000000000

GSO/BGO phoswich counters

The GSO/BGO counter units were the crystal scintillators with active anti coincidence shields. The collimators were made of BGO (i.e Bismuth Germanate, $Bi_4Ge_3O_{12}$) crystals and the X-ray sensor inside the detector well was made of GSO (i.e Gadolinium Silicate, $Gd_2SiO_5(Ce)$) crystals. A counter unit of GSO/BGO consisted of 4 GSO crystals of $24mm \times 24 \times 5$mm thick in a 2×2 matrix form behind each PIN diode with the BGO crystals underneath the GSO sensors. The use of two different kinds of crystals for X-ray sensor and the shield yields an easy discrimination of X-ray source signal from that of any particle events or Compton events registered by the crystal material. The different rise/decay times (i.e $\sim 700ns$ for BGO and $\sim 120ns$ for GSO) allows a single PMT to distinguish the X-rays received at the sensor and shield due to scintillation. As a result of which the events registered in both the GSO and BGO (i.e particle or Compton events different than source events) can be rejected by the phoswich technique. The details of XIS and HXD/PIN and HXD/GSO detectors are given in Table 2.1.

2.6 Nuclear Spectroscopic Telescope Array (2012 - present)

The application of focusing X-ray optics in telescopes helps in achieving higher concentration factor because of their large collecting area i.e. by a factor of 1000 or more than the physical area of the detector over which the X-ray signal gets registered. The X-ray focusing technique has been employed in several X-ray observatories before *NuSTAR* at soft X-rays. However, the *NuSTAR* mission (Harrison et al., 2013) extended the focusing of X-ray photons with energies beyond 10 keV. It is the first hard X-ray focusing telescope orbiting in space. Prior to it, several short duration balloon-borne hard X-ray telescopes such as HERO (High-Energy Replicated Optics) were used to capture X-ray images of galactic X-ray sources in hard X-rays (Ramsey et al., 2002). The *NuSTAR* mission was launched on 2012 June 13 into a low Earth

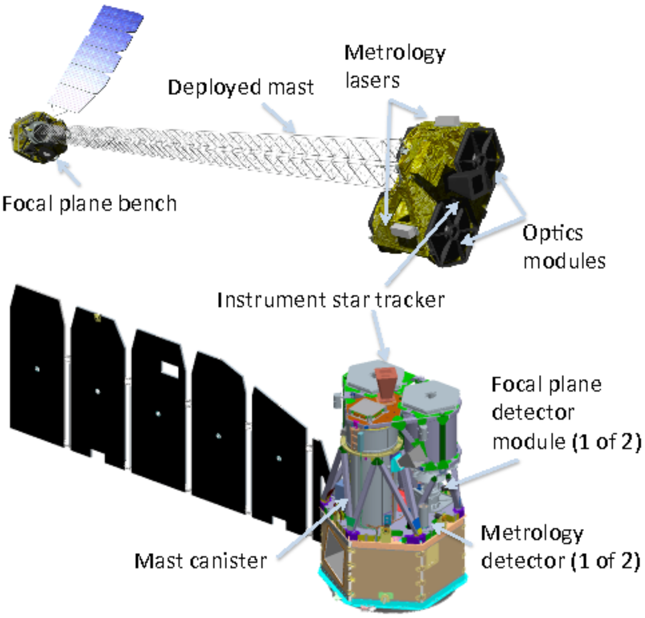

Fig. 2.5 NuSTAR X-ray observatory, Source:https://apod.nasa.gov/apod/image/1206

near-equatorial orbit to carryout sensitive X-ray observations with imaging in hard X-rays up to 79 keV. The lower energy threshold of detection is limited to 3 keV.

There are the two hard X-ray grazing incidence and co-aligned telescopes onboard *NuSTAR* satellite. The two X-ray optics modules are of Wolter-I type mirrors with conical approximation. Each of the optics module has 133 mirror shells. The X-ray optics and the corresponding focal plane detectors (shown in Figure 2.5) are separated by 10.14 m (focal length of the telescope) with the help of a lightweight extendable mast. The two focal plane modules are designated as FPMA and FPMB. These detector modules are a composite system of four hybrid pixelated detectors made from 2 mm thick CdZnTe (CZT) crystal. Due to the location of detector modules at the focal plane of the telescope, the Field of View (FoV) covered by the twin telescopes is $12.45'$. The detector module constitutes a 2×2 array of detectors with each detector as an array of 32×32 pixels of 0.6 mm thick. The detectors are enclosed by an anti-coincidence shield made of CsI material. The X-ray events detected simultaneously by anti-coincidence shield and the detector are treated as X-ray background by onboard signal processors. At energies below 50 keV, the spectral resolution of *NuSTAR* detectors is constant at 400 eV. However beyond this energy due to effects of charge trapping, the energy resolution broadens to 900 eV at 68 keV. A good temporal resolution of 2μ sec can be achieved with the CZT detectors of *NuSTAR*. The telescope and detector parameters of *NuSTAR* observatory are given in Table 2.1.

The present thesis deals with the questions pertaining to X-ray emission properties of Be/X-ray binary (BeXB) pulsars during X-ray outbursts. As the X-ray luminosity of the pulsars gets enhanced during Type-I & Type-II outbursts due to which the pulsars become easily detectable, it gives an opportunity to understand the mechanisms of X-ray emission from the polar regions. The observations carried out during X-ray outbursts of BeXB pulsars form an important basis for this study. In order to understand the changes in pulsar X-ray emission properties during periods of high X-ray activity, we have carried out X-ray spectral and timing studies of several BeXB pulsars. However, among these BeXBs, two pulsars such as KS 1947+300 and EXO 2030+375 form the part of the thesis. The observational details of these pulsars with above mentioned X-ray observatories are discussed in respective chapters of the thesis.

2.7 Data Reduction Techniques, Software and Analysis Procedures

The X-ray data of stellar X-ray sources collected from various X-ray detectors on-board different X-ray satellites cannot be used directly for scientific analysis as these are contaminated by various factors. In X-ray astronomy, detection and measurement of characteristics properties of individual photons from stellar sources is the primary method of studying the emission properties. This is unlikely the case in longer wavelength regimes (infra-red and optical) of astronomical interest where the measurement of integrated flux is used to understand the dynamical properties of the source. The underlying difference lies in the fact that the individual X-ray photons are highly energetic relative to longer wavelength photons but drastically

Table 2.1 Characteristics of X-ray Detectors onboard various X-ray observatories (such as *Suzaku*, *NuSTAR*, *RXTE*). Data from these instruments has been studied in the present thesis.

Observatory	*Suzaku*			*RXTE*		*NuSTAR*
Detector	XIS	PIN	GSO	PCA	HEXTE	FPMA/FPMB
Energy Range(keV)	0.2-12	10-70	40-600	2-60	15-250	3-79
Energy Resolution (FWHM)	130 eV @5.9 keV	$\sim$ 4.0keV	7.6 $\times \sqrt{E_{MeV}}$%	<18% @ 6keV	15% at 60 keV	400 eV @ 10keV, 900 eV @ 68keV
Effective area	340cm^2(FI) and 390cm^2(BI) @1.5keV, 150cm^2(FI) and 100 cm^2 (BI) @8keV	$\sim$ 160cm^2 @ 20 keV	$\sim$ 260cm^2 @ 100 keV	6500 cm^2	1600 cm^2	800 cm^2@ 6 keV
Temporal Resolution	8s (normal), 7.8 msec (P-sum)	61μs	61μs	1μs	8μs	0.1 msec
Angular Resolution	$< 1.5'$	$2'$(HPD)	-	1°		$58''$(HPD), $18''$(FWHM)
Field of View	$18' \times 18'$	$34' \times 34'$ ($\leq 100keV$)	$4.5^\circ \times 4.5^\circ$ ($\geq$ 100keV)	1°FWHM	1°FWHM	$13' \times 13'$

low flux values. Hence, they can be counted at ease. The basic information of each X-ray event is stored in several data files. The structure of the data files is such that the X-ray events with their attributes such as position of incidence on the detector plane, the arrival time and the photon energy are stored in a specific format. Apart from these, the event file also contains some auxiliary information to distinguish the good events from the background X-ray events.

The High Energy Astronomy Software (*HEASoft*) is the most widely used software package for reduction and analysis of multi-mission X-ray data. We have used HEASoft[6] version 6.16 and 6.21 in all our imaging, timing and spectral analysis of X-ray data of BeXB pulsars. The observational data of stellar X-ray sources including those of X-ray binaries are obtained from NASA's HEASARC[7] archive data base. The updated calibration data files associated with each detectors of *RXTE*, *NuSTAR* & *Suzaku* were obtained from CALDB[8] database at HEASARC. The X-ray data of all astronomical sources are generally stored in FITS[9] format. FITS stands for *Flexible Image Transport System*, a data format which uses multi-dimensional arrays to store 1D spectra, 2D images also could accommodate the data in tables with the header keywords describing the information related to the data.

Tools for X-ray timing analysis

The XRONOS[10] timing analysis programs of FTOOLS[11] such as *lcurve*, *efsearch*, *efold*, *powspec* and other tasks such as *lcmath* etc. have been used to extract an X-ray light curve from the event data of X-ray pulsars, search for periodicity in the light curves and finally creating the pulse profiles at different X-ray energies from the X-ray light curves. A brief description of a few of these tasks is illustrated below:

1. The *efsearch* task has been used to search for periodicities in the light curves of X-ray pulsars. This is done by folding the time series data (lightcurve) with

[6] https://heasarc.nasa.gov/lheasoft/
[7] https://heasarc.gsfc.nasa.gov/docs/archive.html
[8] https://heasarc.gsfc.nasa.gov/docs/heasarc/caldb/caldb_intro.html
[9] https://fits.gsfc.nasa.gov/
[10] https://heasarc.gsfc.nasa.gov/docs/xanadu/xronos/manual/xronos.html
[11] https://heasarc.gsfc.nasa.gov/ftools/ftools_menu.html

a range of trial periods. A distribution of χ^2 values of the folded lightcurve versus the periods indicates the recurring periodicity of the pulsar with the highest value of χ^2.

2. Using *efold* and with the knowledge of best period of the pulsar from *efsearch* task, the light curves can be folded at the best pulse period to generate the pulse-profiles at a given epoch of observation. The output plot generated from this task is a plot of normalized counts/sec versus phase of the folded period. When the normalization parameter is set to zero, the pulse profiles are generated without any normalization i.e. with source count rate whereas the default value "norm = 1" results in a pulse profile in which folded light curves are normalized with respect to the average source intensity.

3. Another FTOOL task known as *powspec* can also be used to search the periodicity in the time series data. But this is in frequency domain in which a power density spectrum (PDS) is computed on the basis of a direct slow Fourier algorithm or by a Fast Fourier Transform (FFT) algorithm. The output of this task is a plot of power versus frequency. The error bars in the power spectrum can be obtained as standard deviation of the average power in each frequency bin from different intervals or from the relevant χ^2 distribution of individual frequency intervals.

XSPEC: X-ray spectral analysis tool

The X-ray spectral fitting package, $XSPEC$ (Arnaud, 1996) available within $HEASoft$ is used extensively in the present thesis to carry out spectral analysis of BeXB pulsars. The underlying principle is that observed X-ray spectrum of a source, $S(E)$ can be related to the actual source spectrum *f(E)* through the observed photon counts in the detector channels, $C(I)$ as :

$$C(I) = \int S(E)R(I,E)dE \tag{2.1}$$

Here $R(I,E)$ is the response of the detector to the incident X-ray photons. Its a measure of probability that an incident X-ray photon of energy E reaching the detector module of X-ray telescope can be detected in channel I. It is usually expressed as the product of $RMF(I,E) \times ARF(E)$, where $RMF(I,E)$ is the response matrix of the detector and $ARF(E)$ is the effective area of telescope. The response files for each X-ray mission are provided by the respective instrument team along with calibration database (CALDB). For example, in case of RXTE/PCA and RXTE/HEXTE the detector response files can be generated through the tasks such as "pcarsp[12]" and "hxtrxp[13]" provided as a part of FTOOLS with HESoft. Similarly in case of *Suzaku*/XIS, the response files for corresponding detectors for any particular observation can be generated through response generator tasks such as *XISRMFGEN*[14]. The noise in the source spectrum ($S(E)$) is due to associated systematic and statistical errors with the photon counts $C(I)$.

As per Equation 2.1, the source spectrum $S(E)$ can be computed by inverting the relation and with a given set of observed $C(I)$ and known values of $R(I,E)$. However, such inversion technique does not give a unique and stable solution as there are always small changes in observed spectrum $C(I)$. Instead, as an alternative method, the user predicted model spectrum, $S_p(E)$ from which a count spectrum of the source can also be predicted, i.e. $C_p(I)$ and then compared to the observed count spectrum $C(I)$. Generally a fit statistics is used in these comparisons to identify whether the predicted model spectrum best fits the data obtained from the detector. For this, the initial spectral parameters of predicted model components are varied until a desirable fit-statistic is obtained with best fitted spectral parameters. Based on the nature of X-ray source, other spectral models could be tried if the best fit spectral values are physically unacceptable. In $XSPEC$, while spectral fitting, the χ^2 fit statistics is used mostly in finding the "best-fit" model. In this method, the difference between the observed and predicted values is minimized as :

$$\chi^2 = \sum \frac{(C_{obs}(I) - C_p(I))^2}{(\sigma(I))^2} \tag{2.2}$$

[12]https://heasarc.gsfc.nasa.gov/docs/xte/recipes/pca_response.html
[13]https://heasarc.gsfc.nasa.gov/docs/xte/recipes/hexte_response.html
[14]https://heasarc.gsfc.nasa.gov/docs/suzaku/analysis/xisrmfgen.html

where $\sigma(I)$ is unknown error in channel I estimated to be $\sqrt{C(I)}$ for channel counts $C(I)$. The "goodness-of-fit" criterion of the best fitted composite spectral model indicates the confidence with which the observed spectrum of X-ray source, $C(I)$ matches with the predicted spectrum from the best-fit model. While spectral fitting in $XSPEC$ with χ^2 statistics, the degrees of freedom, dof is taken as the difference between the number of energy channels from which the count spectrum is generated and number of free parameters of the best-fit model. It is expected that for the best-fit model describing the observed spectrum C(I), $\chi^2 \sim dof$. In other words, the "reduced χ^2" i.e $\frac{\chi^2}{dof} \sim 1$. However, the spectral fitting resulting a poor fit would have $\chi^2_{red} > 1$. On the contrary, the values of $\chi^2_{reduced} < 1$ would indicate an over estimation of errors on the data. The choice of best-fit model becomes difficult with the above criterion in situations when different models could fit the spectrum well. This is usually the case if the data used in the fit is not of good quality. In such cases, the choice of an acceptable best-fit model over others can be based on the scientifically correctness of the estimated parameter values. Secondly, with the increase in χ^2 from that of the best-fit model, the "confidence-interval" of each best-fit parameters can be obtained. The amount of increase in χ^2 (i.e $\Delta\chi^2$) is subjected to the confidence level required to achieve. As an example, to estimate a 90% confidence interval for each best fit parameter, the other fit parameters are varied till fixing the parameter of interest to a certain value such that the $\Delta\chi^2 = 2.706$ is achieved from the fit statistic.

Chapter 3

2013 giant X-ray outburst of Be/X-ray binary pulsar KS 1947+300

In this Chapter, the spectral and timing properties of transient Be/X-ray binary pulsar KS 1947+300 have been explored when it was undergoing a giant (Type II) X-ray outburst in 2013 October-November. The X-ray observations were carried out at two different epochs with *Suzaku*, separated by about a month.

3.1 Be/X-ray binary pulsar KS 1947+300

The transient Be/X-ray binary pulsar KS 1947+300 was discovered during a giant outburst on 8 June 1989 at a flux level of 70±10 mCrab in 2-27 keV range with the *Mir-Kvant/TTM* coded-mask X-ray spectrometer (Borozdin et al., 1990). The source was highly variable during the observations of its first detected outburst in 1989 (Borozdin et al., 1990). By 19 August 1989, the observed X-ray flux decreased to 10 mCrab i.e., $1/7^{th}$ of the flux observed during its first detection. Assuming the Galactic column density of $N_H = (3.4 \pm 3.0) \times 10^{22} cm^{-2}$, the 2-27 keV X-ray spectrum was well described by a power law of photon index $\alpha = -1.72 \pm 0.31$. KS 1947+300 was again detected with the CGRO/BATSE in 20-70 keV range reaching a peak intensity of $\sim$ 50mCrab on 16th April 1994 (Finger et al., 1994). The observed pulse period and period derivative were estimated to be 18.7021±0.0001 s and $\dot{P} = 6.0 \pm 0.7 \times 10^{-9}$, respectively. Also independently, (Chakrabarty et al., 1995) detected 18.7 s pulsed emission from an accreting X-ray pulsar GRO J1948+32 in the Cygnus region using the data from 7 April 1994 observation with CGRO/BATSE large area detector. Among various pulsar parameters derived for GRO J1948+32 by (Chakrabarty et al., 1994), the binary system was found to be in a low eccentric orbit with eccentricity $e < 0.25$ unlike other Be/X-ray binaries most of which are in high eccentric orbits $e \geq 0.3$.

After this outburst, the pulsar KS 1947+300 was undetectable during 1995-2000. However, subsequent *RXTE* observations of KS 1947+300 carried out during 2000-2001 found that the source was in a strong outburst. KS 1947+300 became active in 2000 October, reaching an initial peak intensity of ~1 count s^{-1} by November-2000 (MJD 51855) followed by a second outburst with peak intensity of ~9 counts s^{-1} (i.e ~120 mCrab) around 2001 February (MJD 51950) (Galloway et al., 2004). (Swank and Morgan, 2000) detected X-ray pulsations at a period of 18.7579 s in the light curves of KS 1947+300 and found that it is indeed identical to GRO J1948+32, having slowed down from 18.70 s pulsation period during its outburst in 1994 at a rate of 8 ms/yr. Broad-band spectrum of the pulsar in 2-80 keV range obtained from PCA and HEXTE data during this outburst was well explained by a composite model consisting of Comptonization (*compTT* in XSPEC), blackbody and a Gaussian component to represent Fe Kα emission line at around 6.5 keV (Galloway et al., 2004). (Galloway et al., 2004) also estimated the orbital parameters of KS 1947+300 from the RXTE observations during 2000-2001 outburst as : orbital period $P_{orb} = 40.415 \pm 0.010$ days, projected semi-major axis $a_x \sin i = 137 \pm 3$ light seconds and eccentricity $e = 0.033 \pm 0.013$. Low frequency QPO with $\nu_{QPO} = 20$ mHz are reported from the *RXTE* observations of the transient pulsar KS 1947+300 taken during the declining phase of outburst in 2001 (James et al., 2010).

Using *BeppoSAX* observations of pulsar during the declining phase of this 2000-2001 outburst, Naik et al. (2006) also found pulsations at 18.70 s. The 0.1-100 kev broad-band X-ray spectrum was well explained by a continuum model containing Comptonized component (compTT in XSPEC) with a soft blackbody ($\sim 0.6 keV$). An iron emission line at ~6.7 keV was reported with line flux decreasing with hard X-ray flux rather than any iron Kα emission at 6.4 keV. A new outburst of KS 1947+300 was detected on 23 October 2002 with *RXTE* All-Sky Monitor observations. A maximum flux of ~ 20 mCrab in 1.5-12 keV range was detected from the pulsar on 8 November 2002. Before this outburst, the pulsar was detected weakly with a flux of <6 mCrab (Levine and Corbet, 2000). A series of weaker outbursts followed by a major outburst of KS 1947+300 was observed during 2002-2004 with IBIS/INTEGRAL. The strongest of these occurred in April 2004 with peak flux of ~ 100 mCrab in 18-60 keV energy range (Tsygankov and Lutovinov, 2005). The spectra obtained from INTEGRAL/JEM-X telescope during this outburst was well described with a power-law model with exponential cutoff. They also found the spectral softening of the pulsar at higher luminosity. However, any cyclotron line feature was not detected in the 5-90 keV of the spectra of KS 1947+300. Glitches in the pulsar frequencies were reported for the first time in KS 1947+300 from these observations. (Tsygankov and Lutovinov, 2005) observed a rapid variation of the pulse frequency of KS 1947+300 when it was close to the peak flux near 51956.41 MJD. Corresponding fractional change in frequency was $\frac{\Delta f}{f} \sim 3.7 \times 10^{-5}$. It was suspected that the sudden change in spin frequency of the neutron star may have resulted in glitches. (Tsygankov and Lutovinov, 2005) used the magnetized neutron star model of (Ghosh and Lamb, 1979) with standard values of mass and radius of the neutron star respectively at 1.4 $M_\odot$ and 10^6 cm and estimated the distance to the source as $d = 9.5 \pm 1.1$ kpc and magnetic field of the neutron start to be $B = 2.5 \times 10^{13}$G.

Since the last X-ray outburst in 2004, KS 1947+300 was again remained undetected until 2013. In 2013 October, an enhancement in X-ray flux of KS 1947+300 was detected with MAXI/GSC (Kawagoe et al., 2013) at a flux of ~ 20 mCrab in 2-10 keV energy range. Soon after, the outburst was followed by Swift/XRT and X-ray pulsations at 18.79 s were detected in the light curve obtained from a 1 ks exposure observation on 2 October 2013 at 23:03 UT (Kennea et al., 2013). The source flux reached a maximum value at ~ 130 mCrab in the 3-10 keV energy range during this outburst (Fürst et al., 2014). From the spectral analysis of simultaneous *NuSTAR* and *Swift/XRT* observations during this 2013-14 outburst of KS 1947+300, (Fürst et al., 2014) observed significant changes in the power-law photon index. Also

Table 3.1 Log for the *Suzaku* observations of KS 1947+300 during 2013 Type-II outburst.

Observatory/ Instrument	ObsID	Start Date	Exposure(ksec) XIS, HXD	Period (s)
Suzaku	908001010	2013-10-22	29, 29.5	18.8088(1)
Suzaku	908001020	2013-11-22	~5.7, ~32	18.7878(1)

a cyclotron resonance scattering feature (CRSF) at 12.5 keV was reported from these observations for first time (Fürst et al., 2014). The estimated magnetic field of the pulsar from these observations was reported to be $B \sim 1.1 \times 10^{12}(1+z)$G. Prior to this, KS 1947+300 had gone through major outbursts. However, the CRSF were not seen in its spectrum during any of the previously detected outbursts. In this Chapter, results obtained from a detailed timing and broad-band spectral studies of the Be/X-ray binary pulsar KS 1947+300 have been presented. The data from *Suzaku* observations of the pulsar at two epochs during the giant outburst in October-November 2013 are used in the study. The details of the observations are given in Table 3.1.

The *Suzaku* observations of KS 1947+300 used in this Chapter (Table.3.1) are taken from publicly available online archive at DARTS[1]. These were Target of opportunity(ToO) pointed observations with ObsIDs 908001010 (hereafter, Obs I) and 908001020 (Obs II) carried out during the giant outburst of the pulsar. Of these, the Obs-I was close to the peak of the outburst and the Obs-II was performed at the outburst peak. In Figure 3.1, the long term light curve taken from *Swift*-BAT monitoring observations is shown with a zoomed view of 2013 outburst shown in the inset of Figure 3.1.

3.2 Data Reduction and Analysis

In the beginning, the raw event data from both the epochs of *Suzaku* observations were reprocessed by using the task *aepipeline* of HEASoft (version 6.16). The

[1]https://darts.isas.jaxa.jp/astro/suzaku//public_list/public_seq.html

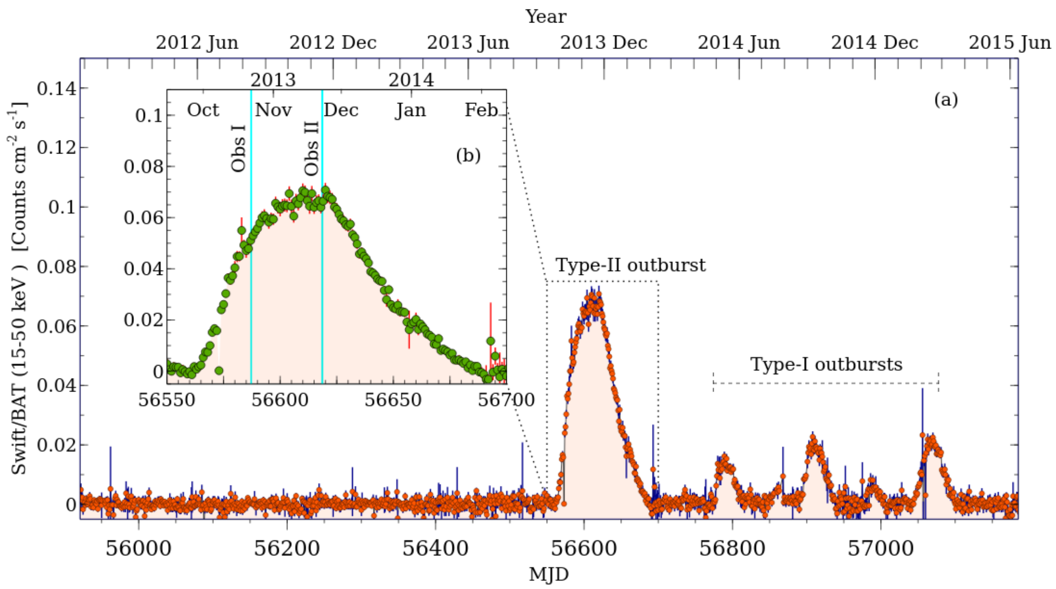

Fig. 3.1 (a) : Swift/BAT light curve of KS 1947+300 is shown with a Type II outburst in 2013 and subsequent Type I outbursts. (b) : A zoomed view of 2013 giant outburst with two *Suzaku* observations shaded at the respective epochs as Obs I & Obs II (see text for details).

thermal flexing of *Suzaku* led to slow wobbling of optical axis which could blurred the source images extracted from XIS events. This was taken care by adjusting the attitude file of the spacecraft. However KS 1947+300 was bright during the observation as it was undergoing a giant X-ray outburst. Hence, further improvements were done by correcting the attitude file by using the S-lang script *aeattcor.sl* [2]. This reduced the blurring in the image by producing the images with sharper PSF. Thereafter, we have checked for possible pile-up of X-ray photons using the S-lang script *pile_estimate.sl* [3]. The pileup in the CCD detectors occurs when more than one X-ray photon simultaneously fall on the same CCD pixel and within the same time frame. As a result of which the CCD readout records it as a single photon having higher energy than the incident individual photon. Sometimes, these events are also discarded as bad events by the detector electronics. The pileup script generates a pileup map from the *Suzaku*-XIS event data file that allows in estimating the effective pile-up fraction. During the Obs I, the images extracted from XIS event data showed a pile-up fraction of $\sim 31\%$, 21% & 33% at the respective image centers of XIS-0, XIS-1 & XIS-3. Similarly during Obs II, the central regions of XIS images had a fractional

[2]http://space.mit.edu/ASC/software/suzaku/aeattcor.sl
[3]http://space.mit.edu/ASC/software/suzaku/pile_estimate.sl

pile-up of $\sim 15\%, \sim 12\%$ & 18%, respectively. With the help of generated pile-up maps, we selected annular regions in each XIS image to limit the pile-up below 4% in our further analysis. Thus annular regions with inner and outer radii of $35''$& $200''$, respectively, were chosen for XIS images from Obs I. Similarly, for Obs II, annular regions centered with radii $35''$& $200''$around the XIS images had been considered as source regions for extracting source light curves and spectra. In order to extract XIS background light curves and spectra, we selected a circular source free region in the XIS image frame. We have also extracted the source light curves & spectra from HXD/PIN and HXD/GSO cleaned event data with by using suitable GTI (good-time-interval) selection in *XSELECT*. The respective background light curves and spectra were generated from the dead time corrected tuned background event data files provided by the *Suzaku* team. The requisite extraction procedures followed to produce source light curves after background correction are mentioned in Sections of Chapter 2. Subsequently, barycentric correction was applied on the extracted source light curves by using *aebarycen* task of FTOOLS to account for the effects of the satellite and Earth's motion around the Sun. The barycentric corrected light curves of KS 1947+300 were obtained from XIS, PIN and GSO event data of Obs I with a time resolutions of 2s, 1s & 1s respectively and for Obs II, time resolution of XIS, PIN and GSO light curves were extracted at time resolutions of 0.5 s, 1 s and 1 s, respectively. The periodicity in the pulsar light curves was searched by using χ^2 maximization technique of *efsearch* FTOOL.

3.3 Pulse profiles

During the epoch of Obs I, we found that the pulsar was showing X-ray pulsations at a period of 18.8088 s. During the second *Suzaku* observation, the pulsar spin period was estimated to be 18.7878(1) s. It can be clearly seen that, the pulsar was spinning up rapidly even with in one month interval. During the concurrent Type I outbursts following the 2013 giant outburst, the pulsar was also spinning up. In order to study the timing variability of the pulsar with pulse phases, we constructed pulse profiles by folding the light curves at the pulsar spin period.

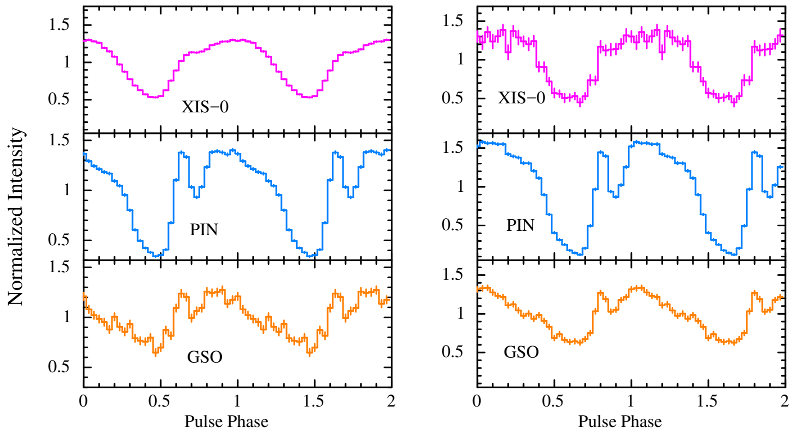

Fig. 3.2 Soft to hard X-ray pulse profiles of KS 1947+300 in different energy bands obtained from XIS-0 (top panel; in 0.2–12 keV range), PIN (second panel; in 10–70 keV range) and GSO (bottom panel; in 40–600 keV range) during Obs-I (left panel) and Obs II (right panel) of 2013 giant outburst, respectively. Pulse profiles were found to be smooth and single peaked at lower energies with the appearance of a dip-like structure at hard X-rays. The errors in the figure are estimated for 1σ confidence level. Two pulses are shown for clarity.

During both the epochs of *Suzaku* observations of KS 1947+300, the pulse profiles of the pulsar were found to be evolving. In Figure 3.2, the variations in the pulse profile of KS 1947+300 at soft and hard X-rays are shown. The pulse profiles at soft X-rays are found to be single peaked and devoid of any structures. However, at hard X-rays energy bands (i.e 10-70 keV, second panels of Figure 3.2), a sharp dip-like structure appeared at 0.7-0.8 pulse phases in the pulse profiles during both the observations. In order to understand the energy dependent behaviour of the dip, we further investigated the pulse profiles at different energy intervals. The source and background light curves at various energy ranges were extracted from the XIS, PIN and GSO event data of both the *Suzaku* observations.

The energy resolved pulse profiles obtained from these light curves are shown in Figures 3.3 & 3.4 for Obs I and Obs II, respectively. The evolution of the dip structure in the pulse profiles with energy can be clearly seen from these figures. At energies below 5 keV, the profiles were smooth and single peaked during Obs I. With increase in energy, a narrow dip-like feature emerged in the pulse profiles and became prominent in the 30-40 keV range. Afterwards, the pronounced dip structure started diminishing beyond 40 keV. These dips disappeared from the pulse profiles in 70-100 keV. Similar energy dependence is also seen in the pulse profiles

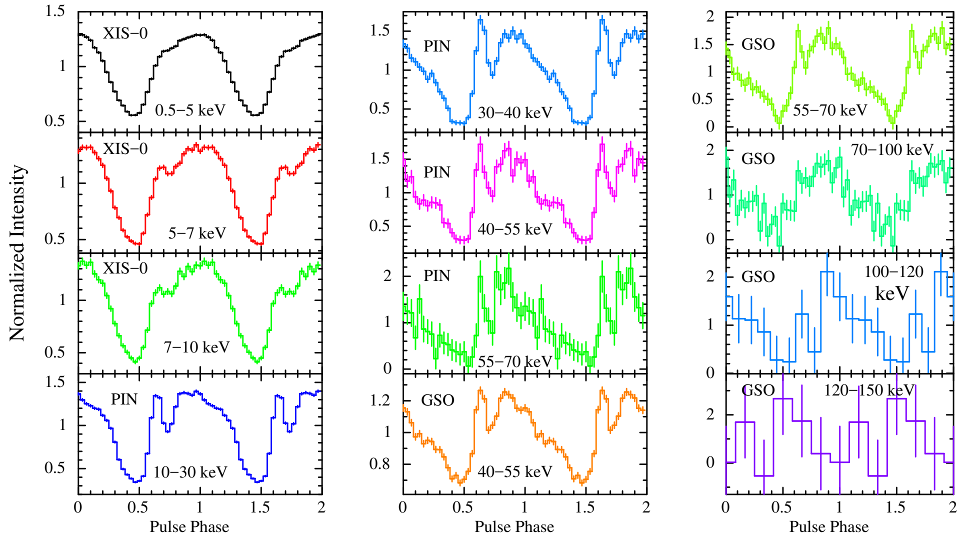

Fig. 3.3 Energy resolved pulse profiles of KS 1947+300 during the first *Suzaku* observation of the 2013 giant outburst. The pulse profiles were obtained from XIS-0, HXD/PIN and HXD/GSO light curves of the pulsar.The errors in the figure indicate the 1σ uncertainties. Two pulses are shown for clarity.

from the second *Suzaku* observation. The X-ray pulsations in the light curves of KS 1947+300 were detected up to as high as $\sim$ 120 keV and $\sim$ 150 keV from Obs I and Obs II, respectively.

The absorption dips in the pulse profiles of BeXB pulsars are generally found to be prominent in the soft X-rays with the subsequent weakening or disappearance in the hard X-rays (Paul and Naik, 2011). However, in the present case of KS 1947+300, the soft X-ray pulse profiles were devoid of any dips which became pronounced in hard X-rays. The cause of these peculiarities is investigated further with the spectral analysis of the pulsar emission during the Type II X-ray outburst. This has been discussed in following Sections.

3.4 Pulse-Phase Averaged Spectroscopy

In order to study carry out spectral investigation of KS 1947+300 during the Type II outburst, we have used the data from all XISs (i.e XIS-0, 1 & 3), PIN & GSO detectors onboard *Suzaku*. We extracted source & background spectra from the reprocessed cleaned event files of each of the above mentioned detectors. To obtain

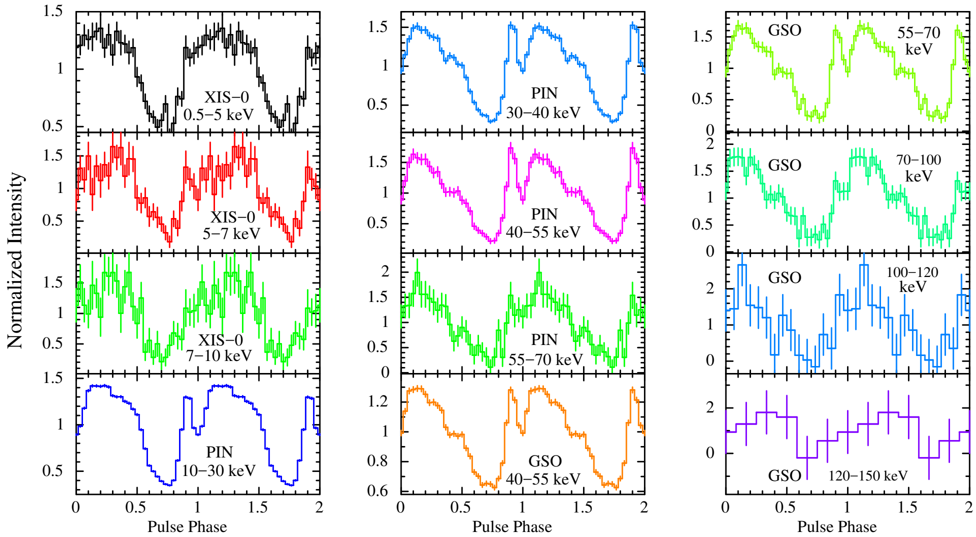

Fig. 3.4 The energy resolved pulse profiles of KS 1947+300 during the second *Suzaku* observation of the 2013 giant outburst. The pulse profiles were obtained from XIS-0, HXD/PIN and HXD/GSO light curves of the pulsar. The errors in the figure indicate the 1σ uncertainties. Two pulses are shown for clarity.

the source and background spectra from XIS event data, we selected corresponding extraction regions as mentioned in Section 3.2. The source spectra obtained from XIS and PIN event data were re-binned to get a minimum of 20 counts in each energy bin. For the GSO spectra, however, the grouping scheme[4] as suggested by the instrument team was followed. In order to resolve the cross calibration issues among the front and back illuminated CCDs, we added a systematic error of 1% to all the XISs spectra. Simultaneous spectral fitting in 1–110 keV range for both the epochs of *Suzaku* observations was done by using XSPEC v12.8.2 package. The presence of Si and Au edges in the XIS spectra at energies of 1.7–1.9 keV & 2.2–2.4 keV are known to be of instrumental origin. Hence, data in above energy ranges were ignored from fitting.

We tried to fit the broad-band spectra with continuum models such as high-energy cut-off power law, a cutoff power law model and the NPEX model (Negative and Positive power law with an EXponential cutoff). Relative instrument normalizations were allowed to vary freely whereas all other model parameters across the detectors were tied while simultaneously fitting the broad-band spectra. The absorption of

[4] https://heasarc.gsfc.nasa.gov/docs/suzaku/analysis/abc/node10.htm#SECTION00106000000000000000

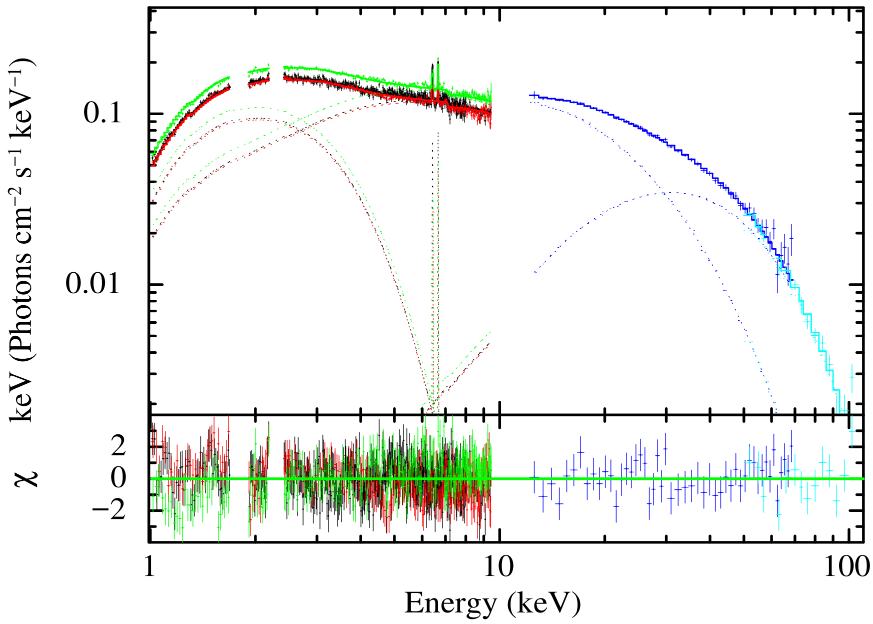

Fig. 3.5 Broad-band (1-110 keV energy range) spectrum of KS 1947+300 obtained with the XIS-0, XIS-1, XIS-3, PIN and GSO detectors of first *Suzaku* observation during the 2013 October outburst along with the best-fit model comprising a partially absorbed NPEX continuum model, a blackbody component for soft X-ray excess, a Gaussian function for the iron emission line and fixed cyclotron absorption component. The contributions of the residuals to the χ^2 for each energy bin for the best-fit model are shown in the bottom panel.

low energy photons by interstellar matter along the line of sight was taken care of with the inclusion of *photoelectric absorption*, i.e "phabs[5]" component. In soft X-rays, an additional component such as blackbody (XSPEC: bbody) was needed to account for the soft X-ray excess seen in the spectra of KS 1947+300. During initial fitting a broad emission line at ∼6.5 keV with a width of ∼200 eV was detected. However upon a close inspection of spectral residual at this energy, it was found that there were two iron lines at 6.4 and 6.7 keV with line equivalent widths of $\sim 18\ keV$. These are identified as emission lines from neutral and He-like iron atoms and fitted with Gaussian functions at respective energies. Apart from the soft X-ray excess and emission lines found in the spectra, we found that the addition of a partial covering absorption component to above mentioned continuum models improved the ξ^2 values with a change of $(\Delta\xi^2 \geq 70)$. We note that the partial covering spectral component has been used previously to investigate the presence of phase dependent absorption dips in pulse profiles of BeXB pulsars (Paul and Naik, 2011). As can

[5]https://heasarc.gsfc.nasa.gov/xanadu/xspec/manual/XSmodelPhabs.html

be seen from the timing studies of the pulsar that the pulse profile were seen with multiple absorption dips at certain pulse phases. Therefore, we used the partial covering component to investigate the cause of these absorption dips in the pulse profiles of KS 1947+300. We have also included a cyclotron line at 12.2 keV in our model as it was detected in pulsar spectrum obtained from *NuSTAR* observations. This energy falls at the edge of energy coverage of both XIS and PIN detectors and hence the detector calibration at this energy were poor. The PIN response matrices have a systematic uncertainties up to 5% in the 12-15 keV range. Therefore, during spectral fitting, we have ignored the PIN data below 15 keV as suggested by *Suzaku* team [6].

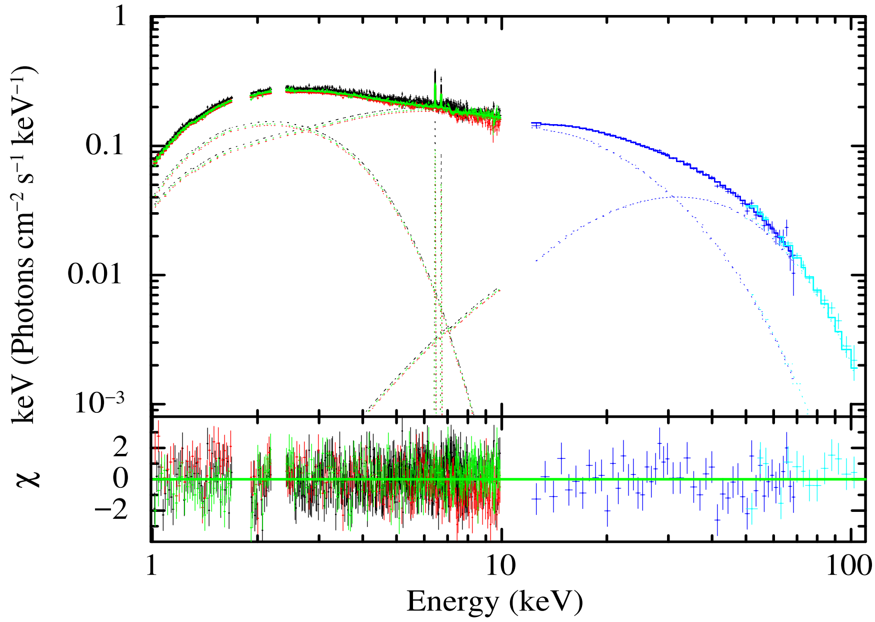

Fig. 3.6 The energy spectrum of KS 1947+300 in 1-110 keV obtained with the XIS-0, XIS-1, XIS-3, PIN, and GSO detectors of second *Suzaku* observation during the 2013 October outburst along with the best-fit model comprising a partially absorbed NPEX continuum model, a blackbody component for soft X-ray excess, a Gaussian function for the iron emission line and fixed cyclotron absorption component. The contributions of the residuals to the χ^2 for each energy bin for the best-fit model are shown in the bottom panel.

The cyclotron line parameters were therefore fixed at the values reported from *NuSTAR* observations ($E_{cycl} = 12.2\ keV$, $\sigma = 2.5\ keV$, & $\tau = 0.16$) (Fürst et al., 2014). We have found that among the spectral continuum models used to describe the *Suzaku* spectra of KS 1947+300, the partial covering NPEX model with other

[6] https://heasarc.gsfc.nasa.gov/docs/suzaku/analysis/abc/node8.html#SECTION00861000000000000000

spectral components was the best-fit model for both the observations. This can be seen from Table 3.2 in which the best fitted spectral parameters for all the three models are quoted for Obs I & II. In the table, it can be seen that the value of additional column density (N_{H2}) detected was significantly higher compared to the galactic column density (N_{H1}). The pulsar spectrum at the peak of the outburst (Obs. II) was harder than that during the Obs I. Similarly, the blackbody component used to measure the soft X-ray excess was strong at the outburst peak (Obs II) with higher values of blackbody temperature and flux compared to that during Obs I. The phase averaged energy spectra of KS 1947+300 along with best fitted partial covering NPEX continuum model and the residuals for Obs I & II are shown in Figures 3.5 & 3.6 respectively.

3.5 Pulse-phase Resolved Spectroscopy

The evidence of soft X-ray excess in the phase-averaged spectra was quiet intriguing and so is the nature of absorption dips in the hard X-ray pulse profiles. In order to understand the evolution of spectral parameters and the origin of soft X-ray excess emission, we have carried out further spectral investigation through pulse-phase resolved spectroscopy. For this, we have gathered the XISs, PIN and GSO source spectra in 9 and 10 phase bins, respectively, for both the observations. Background spectra, response files and effective area files used for phase-averaged spectral fitting were also used for phase-resolved spectroscopy. Simultaneous fitting of XIS, PIN and GSO phase-resolved spectra was carried out with the partial covering NPEX model along with other additional components. In phase-resolved spectroscopy, the Galactic hydrogen column density (N_{H1}) was kept fixed to its phase-averaged value as it is expected to be same along the source direction. Due to lack of sufficient photons, it was difficult to resolve the iron emission lines in phase-resolved spectral fit. Therefore, the energy and width of iron emission lines along with the cyclotron line parameters and relative instrument normalizations were kept fixed to their phase-averaged values. The pulse phase variations in other spectral parameters were noted and shown in Figures 3.7 & 3.8 for Obs I and II, respectively. It can be seen from

Table 3.2 Best-fitting spectral parameters (with 90% errors) obtained from two *Suzaku* observations of KS 1947+300 during 2013 October outburst. Model-1 : partial covering NPEX model with Gaussian components and cyclotron absorption line; Model-2 : partial covering high-energy cutoff model with Gaussian components and cyclotron absorption line ; Model-3: partial covering cutoff power law model with Gaussian components and a cyclotron absorption line.

Parameter	2013 October (Obs I)			2013 November (Obs. II)		
	Model-1	Model-2	Model-3	Model-1	Model-2	Model-3
$N_{H1}{}^{a}$	0.50±0.02	0.50±0.02	0.52±0.02	0.48±0.02	0.50±0.02	0.53±0.02
$N_{H2}{}^{b}$	7.6±1.0	8.2±1.1	7.6±1.1	11.3±2.5	10.7±1.7	12.1±4.8
Covering fraction	0.44±0.06	0.45±0.06	0.43±0.06	0.35±0.06	0.35±0.06	0.27±0.07
Photon Index (Γ)	0.67±0.03	0.95±0.04	0.92±0.05	0.62±0.04	0.93±0.04	0.93±0.03
E_{cut} (keV)	10.2±0.3	5.4±0.4	20.2±0.9	10.6±0.4	5.9±0.3	21.6±0.7
E_{fold} (keV)	–	21.0±0.7	–	–	21.6±0.7	–
Blackbody temp. kT (keV)	0.54±0.02	0.56±0.02	0.54±0.02	0.63±0.03	0.65±0.02	0.65±0.03
Blackbody flux^{c}	0.88±0.13	0.96±0.13	0.77±0.13	1.34±0.19	1.40±0.20	1.02±0.19
Emission lines						
Fe $K\alpha$ line energy (keV)	6.42±0.03	6.42±0.03	6.42±0.03	6.45±0.02	6.45±0.02	6.45±0.02
Width of Fe line (keV)	$0.01^{+0.06}_{-0.01}$	$0.01^{+0.06}_{-0.01}$	$0.01^{+0.06}_{-0.01}$	$0.01^{+0.04}_{-0.01}$	$0.01^{+0.04}_{-0.01}$	$0.01^{+0.04}_{-0.01}$
Eq. width of Fe line (eV)	18±2	19±2	19±2	20±3	20±3	22±2
Line energy (keV)	6.66±0.05	6.66±0.05	6.66±0.05	6.71±0.04	6.71±0.04	6.71±0.02
Line width (keV)	$0.01^{+0.07}_{-0.01}$	$0.01^{+0.07}_{-0.01}$	$0.01^{+0.07}_{-0.01}$	$0.01^{+0.07}_{-0.01}$	$0.01^{+0.07}_{-0.01}$	$0.01^{+0.07}_{-0.01}$
Equivalent width (eV)	17±2	18±2	18±2	11±3	11±3	13±3
Source flux						
Flux^{c} (1-10 keV)	2.6±0.2	2.7±0.2	2.6±0.2	4.3±0.4	4.3±0.4	4.1±0.4
Flux^{c} (10-70 keV)	5.4±0.5	5.3±0.4	5.3±0.3	6.6±0.6	6.5±0.5	6.5±0.4
Flux^{c} (70-100 keV)	0.21±0.03	0.27±0.02	0.27±0.02	0.38±0.03	0.38±0.03	0.38±0.02
Reduced χ^2	1.18 (942)	1.25 (970)	1.25 (971)	1.08 (970)	1.10 (942)	1.13 (971)

^{a} : Equivalent hydrogen column density (in 10^{22} atoms cm^{-2} units).
^{b} : Additional hydrogen column density (in 10^{22} atoms cm^{-2} units).
^{c} : Absorption corrected flux in units of 10^{-9} ergs cm^{-2} s^{-1}.
^{d} : Fixed cyclotron line energy.

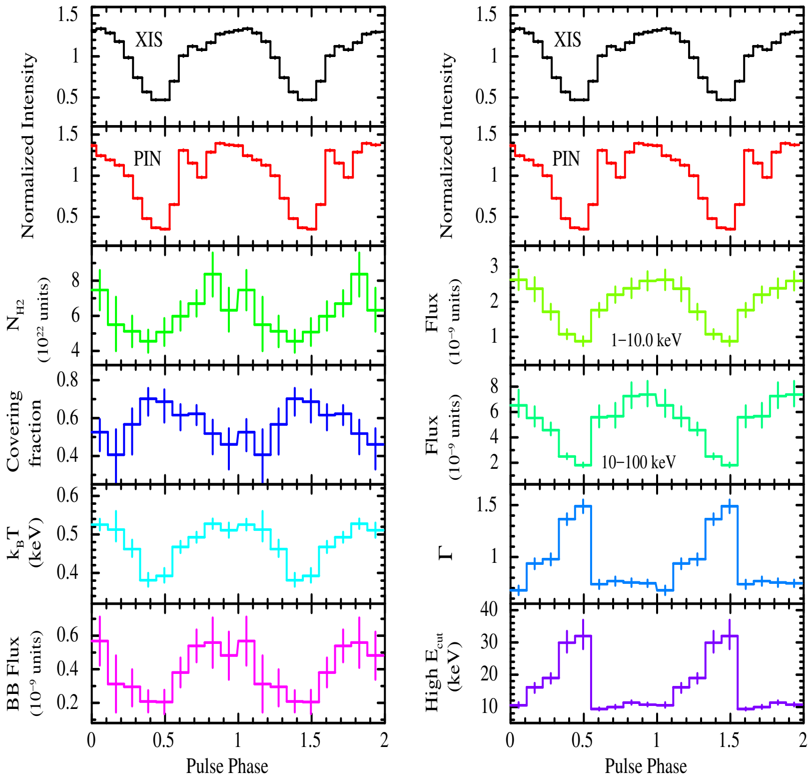

Fig. 3.7 Spectral parameters obtained from the phase-resolved spectroscopy of KS 1947+300 during first *Suzaku* observation in 2013 October. The first and second panels in both sides show pulse profiles of the pulsar in 0.5-10 keV (XIS-0) and 10-70 keV (HXD/PIN) energy ranges. The values of N_{H_2}, covering fraction, blackbody temperature and blackbody flux are shown in third, fourth, fifth and sixth panels in left side of the figure, respectively. The soft X-ray flux in 1-10 keV range, hard X-ray flux in 10-100 keV range, photon index and high energy cutoff are shown in third, fourth, fifth and sixth panels in right side of the figure, respectively. The blackbody flux and source fluxes in 1-10 and 10-100 keV are quoted in the units of 10^{-9} ergs cm^{-2} sec^{-1}. The errors in the figure are estimated for 90% confidence level.

these figures that the changes in the spectral parameters are similar during both the observations. The soft and hard X-ray pulse profiles obtained from the XIS-0 and PIN light curves of both observations are shown in top panels on either sides of Figures 3.7 & 3.8. The changes in flux values in 1-10 keV and 10-100 keV over pulse phases are shown in panels in the right side along with phase variations in power-law photon index & cutoff energy. In the left side panels of these figures, we showed changes in other spectral parameter such as additional column density (N_{H2}), covering fraction, blackbody temperature (kT) and corresponding soft X-ray excess flux.

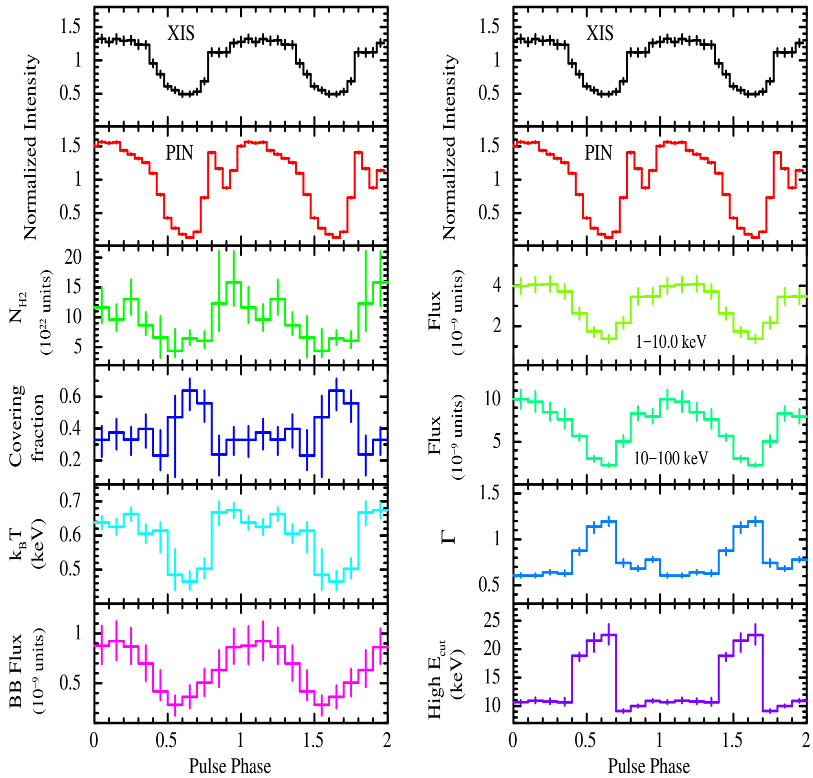

Fig. 3.8 Spectral parameters obtained from the phase-resolved spectroscopy of KS 1947+300 during second *Suzaku* observation in 2013 November. The first and second panels in both sides show pulse profiles of the pulsar in 0.5-10 keV (XIS-0) and 10-70 keV (HXD/PIN) energy ranges. The values of N_{H_2}, covering fraction, blackbody temperature and blackbody flux are shown in third, fourth, fifth and sixth panels in left side of the figure, respectively. The soft X-ray flux in 1-10 keV range, hard X-ray flux in 10-100 keV range, photon index and high energy cutoff are shown in third, fourth, fifth and sixth panels in right side of the figure, respectively. The blackbody flux and source fluxes in 1-10 and 10-100 keV are expressed in units of 10^{-9} ergs cm^{-2} s^{-1}. The errors in the figure are estimated for 90% confidence level.

Figures 3.7 & 3.8 showed that the spectral parameters are variable with pulse phases of the pulsar. At phases corresponding to the dips in hard X-ray pulse profile, the value of additional column density was found higher compared to other pulse phases. The variations of source flux in 1-10 keV, blackbody flux and temperature showed a similar pattern of variations as that of the pulse profile in soft X-rays. It clearly confirms that the soft X-ray excess is pulsating and is in phase with the source flux. At the main dip phase of the pulse profile, a higher value of power-law index (Γ) and high-energy cutoff was also observed.

The dependence of spectral parameters on additional column density and source flux in 1–10 keV range is also checked. It can be seen in Figures 3.9 & 3.10 that

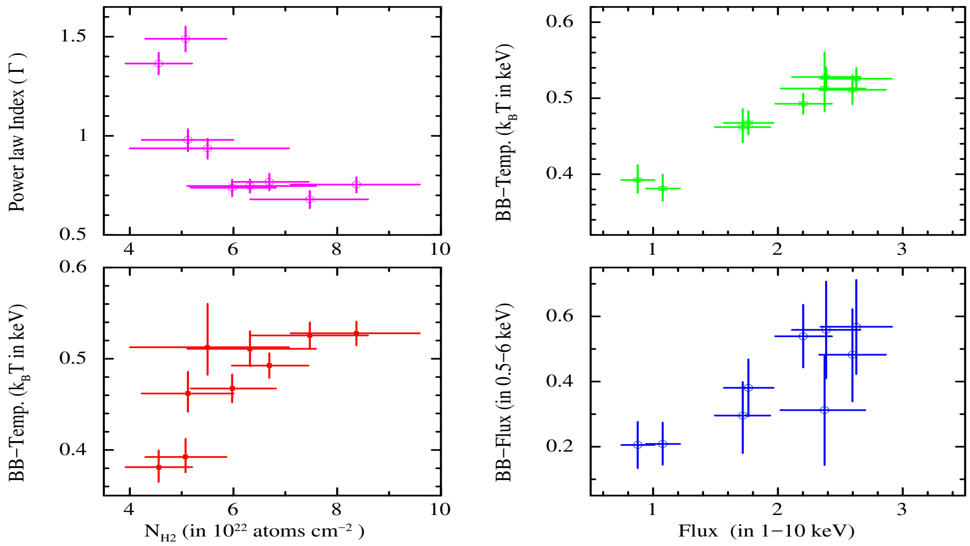

Fig. 3.9 Dependence of different spectral parameters obtained from the phase-resolved spectroscopy of KS 1947+300 during first *Suzaku* observation. The blackbody flux and 1-10 keV source flux are quoted in the units of 10^{-9} ergs cm^{-2} s^{-1}.

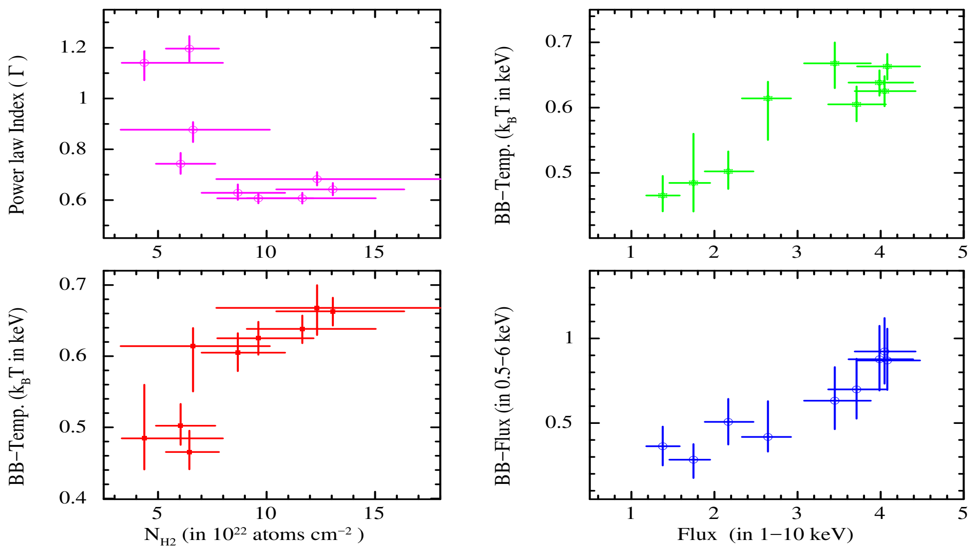

Fig. 3.10 Dependence of different spectral parameters obtained from the phase-resolved spectroscopy of KS 1947+300 during second *Suzaku* observation. The blackbody flux and 1-10 keV source flux are quoted in units of 10^{-9} ergs cm^{-2} s^{-1}.

the blackbody temperature and flux (i.e BB-flux) showed a positive correlation with the soft X-ray flux in 1–10 keV. However, the Γ values were high at low values of additional column density (N_{H2}) but decreased later on with the subsequent increase in N_{H2}.

3.6 Results & Discussion

In the Be/X-ray binary pulsars, during the episodes of Type II outburst, the accretion of matter by the neutron star occurs in large quantities from the decretion disc of the Be companion star. As the accreting matter transfers part of its angular momentum to the pulsar, a steady spin-up of the pulsar is expected. According to Ghosh & Lamb accretion model, the spin-up of the pulsar is related to the pulsar luminosity as $\dot{P}_{spin} \propto L^{6/7}$. In the case of KS 1947+300, we have seen that the pulsar was spinning up rapidly during the 2013 Type II outburst. From the *Suzaku* observations taken during this outburst, it was found that the pulsar was spinning at a rate of $\dot{\omega}_{su} \simeq 1.27 \times 10^{-5}\ Hz/d$. The possible cause of this spin-up can be due to a net effective torque exerted onto the neutron star by the accreting matter. This kind of rapid spin-up was also observed earlier during the declining phase of the outburst in 2001 (Naik et al., 2006). Using the theory of quasi-spherical settling accretion (Postnov et al., 2015; Shakura et al., 2012), we estimated the pulsar magnetic field from the steady spin-up of the pulsar. According to this theory, the spin-up of the pulsar is related to the neutron star dipole magnetic moment through the relation given by Eq.3.1

$$\dot{\omega}_{su} \simeq 10^{-9}[Hz\, d^{-1}]\, \Pi_{su}\, \mu_{30}^{1/11} v_8^{-4} \left(\frac{P_{orb}}{10\, d}\right)^{-1} \dot{M}_{16}^{7/11} \tag{3.1}$$

In the above equation, Π_{su} is the dimensionless parameter which is in the range of ∼4.6 to 10 (Postnov et al., 2015; Shakura et al., 2012) and is independent of the BeXB systems. For the present case of KS 1947+300, we considered it to be 4.6. Assuming a dipole configuration of the magnetic field, the dipole magnetic moment of the neutron star (i.e $\mu_{30} = \mu/10^{30}[G\ cm^3]$) is related to the neutron star magnetic field as $\mu = \frac{1}{2}BR_{NS}^3$ (here R_{NS} is the assumed neutron star radii of

10 km). The stellar wind velocity, $v_8 = v/10^8[cm\ s^{-1}]$ in case BeXB systems is considered to be around 200 km s^{-1} (Waters et al., 1988). The mass accretion rate is estimated from the outburst luminosity of the pulsar. From the observed luminosity of the pulsar ($L_x \sim 10^{38}$ergs s^{-1}) during the *Suzaku* observations, we estimated mass accretion rate to be $\dot{M}_{16} = 100$ where $\dot{M}_{16}$=$\dot{M}/10^{16}$[g s^{-1}]. The binary orbital period of KS 1947+300 is $P_{orb} = 40.42\ d$ (Galloway et al., 2004). Using the values of above mentioned parameter in Eq.3.1, we estimated the magnetic field of the pulsar and found it to be $\sim 1.2 \times 10^{12}$ G, typical of the accretion powered pulsars residing in BeXB systems. The present estimated value of pulsar magnetic field from the spin-up rate is found to be in agreement with the value obtained from cyclotron absorption line features seen in the pulsar at 12.2 keV from *NuSTAR* observations during the 2013 giant outburst.

The soft X-ray pulse profiles of BeXBs are generally found to be structured with the presence of single or multiple absorption dip-like complex features (Paul and Naik, 2011). These dips are thought to be due to absorption or obscuration of soft X-ray photons by streams of accreting matter around the neutron star. Sometimes, these absorption dips are seen even at hard X-rays. For example, in case of EXO 2030+375 (Naik, 2013; Naik and Jaisawal, 2015) observed multiple absorption dips in the pulse profiles up to X-ray energies as high as 70 keV. Later, from a phase resolved spectroscopy, they identified that the presence of additional matter in the dip phases was indeed the possible cause of these features seen in the pulse profiles. However, in the present study of KS 1947+300, the evolution of pulse profile dips up to $\sim$ 70 keV cannot be explained by invoking the presence of matter. This is due to the fact that the amount of additional matter detected at the dip phases through phase resolved spectral studies is insufficient ($\leq 20/times10^{22}$cm^{-2}) to cause hard X-ray absorption dips up to $\sim 70\ keV$. The other possible causes that would be responsible for pulse profile variations are the effect of cyclotron resonance scattering features seen in the hard X-ray spectra of the pulsar or due to geometrical effect. At cyclotron line energies, (Schönherr et al., 2014) showed that the beamed emission of the pulsar gets affected leading to phase shifts or phase lags in the average pulse profiles. The accreting plasma falling at relativistic speeds onto the neutron star poles could increase the angular difference between the beaming of cyclotron line photons and continuum radiation. Such effects were seen in the pulse profiles of V 0332+53 (Tsygankov et al., 2016), 4U 0115+63 (Ferrigno et al., 2011), and GX 304-1 (Jaisawal et al., 2016). However, in the energy resolved pulse profiles of KS 1947+300 (see Figs. 3.3 & 3.4), we do not see any such significant shifts in the pulse profiles near the cyclotron line energy. On the contrary, the strength of the dips increases and they become prominent in 30-40 keV range where the effect of cyclotron resonance scattering features could be negligible as the fundamental line is at 12.2 keV. Hence, we expect that the CRSF could not be playing a key role in shaping the hard X-ray dips in the pulse profiles of KS 1947+300. The evolution of a single dip in the pulse profiles of KS 1947+300 might suggest a direct viewing of the neutron star pole via accretion column. In that case, a radiation dominated shock forming above the neutron star surface at high luminosity of the pulsar (as seen in the present *Suzaku* observations of KS 1947+300) could absorb photons up to higher energies. This should in turn lead to formation of absorption dips at the peak of the pulse profile. However, the asymmetric position of the absorption dip with respect to the main dip seen in the pulse profiles of KS 1947+300 (in Figures 3.3 & 3.3) invalidates the direct viewing of accretion column structure along the neutron star magnetic axis which otherwise would have caused absorption dips at the peak of the pulse profiles. In exploring the other possible scenarios that might be affecting the shape of the pulse profiles, we came across another physical possibility. It is known from previous studies that in X-ray pulsars, the shape of pulse profile varies with the geometry of emission region or with viewing angle of accretion column (Caballero et al., 2011; Kraus et al., 1995; Sasaki et al., 2012). Considering this, we assume that the dips seen up to 70 keV in the pulse profiles could be due to these geometrical configurations. The absence of the intrinsic dip feature in low energy pulse profiles still puzzling. The possible cause of this peculiarity becomes clear from the spectra studies of the pulsar.

The broad-band phase averaged and phase resolved spectral studies of KS 1947+300 showed interesting behaviour of the source. During both the *Suzaku* observations, the amount of additional matter detected near the neutron star was significant as seen from the higher values of additional column density. The temperature corresponding to the soft X-ray excess was at higher values during the outburst peak (Obs II). Considering the blackbody emitting region to be spherically symmetric, we estimated the size of emitting region producing soft X-ray excess. It was found to be $\sim 29-31$ *km*. Thus, the pulsating nature of this emission and dimension of the emission region hint that it is located close to the neutron star surface. The probable sites of origin of this excess would be the accretion column and/or accretion streams in KS 1947+300 (Hickox et al., 2004; Naik and Paul, 2002, 2004). From the *BeppoSAX* observations of KS 1947+300 during its 2001 outburst, Naik et al. (2006) had not detected any neutral iron $K\alpha$ line near 6.4 keV except the emission lines at 6.7 keV from He like iron atoms. However, during the 2013 giant outburst, we could see both the neutral and ionized iron lines at 6.4 keV and 6.7 keV from the *Suzaku* observations. Fürst et al. (2014) detected a cyclotron absorption feature at ~ 12.2 *keV* in the spectra of KS 1947+300 obtained from the *NuSTAR* observations during 2013 giant outburst. Detection of such features helps in direct estimation of magnetic field of the pulsar through the relation $E_{cyc} = 11.6B_{12} \times (1+z)^{-1}$. The strength of magnetic field of the pulsar was reported to be $\sim 1.1 \times 10^{12}(1+z)$ G (Fürst et al., 2014). We would like to emphasize that, although the pulsar was observed at three different epochs during 2013 giant outburst with *NuSTAR*, the signature of fundamental cyclotron line in the spectrum was seen only on one occasion (during second *NuSTAR* observation). There was no evidence of any harmonics of the fundamental line in the *NuSTAR* spectra. Even in data obtained from the *Suzaku* observations, our search for cyclotron harmonics in hard X-ray spectra did not yield any confirmed detection although the pulsar was very bright. There are several cases of pulsars in which cyclotron lines are seen in the broad band spectra without any of its harmonics, *e.g.*Cen X-3 (Naik et al., 2011a; Suchy et al., 2008), Swift J1626.6-5156 (DeCesar et al., 2013) and IGR J17544-2619 (Bhalerao et al., 2015). The X-ray luminosity of the pulsar in 1-100 keV range, during the giant outburst was as high as $\sim 9.8 \times 10^{37}$ ergs s^{-1}and 1.3×10^{38} ergs s^{-1}during first and second *Suzaku* observations. We were interested in finding the luminosity state of KS 1947+300 during the Type II outburst. Assuming the canonical neutron star parameters with a CRSF feature at 12.2 keV, we estimated the critical luminosity of the pulsar to be $\sim 1.6\times10^{37}$ $\mathrm{ergs\,s^{-1}}$using the relation of Becker et al. (2012). It clearly showed that the pulsar was accreting in super-Eddington regime ($i.e.$above critical luminosity) during the 2013 outburst (present case) and during previous outburst in 2000 November (Naik et al., 2006).

3.7 Conclusion

In this Chapter, we have investigated the timing and spectral properties of transient Be/X-ray binary pulsar KS 1947+300 by using observations carried out with *Suzaku* during a giant outburst in 2013. The soft X-ray profiles were single peaked and devoid of any absorption dips. But in the hard X-ray pulse profiles, the presence of absorption like dips is evident. The phase-averaged spectrum of the pulsar in wide energy band (1-100 keV range) was well explained by a partially absorbed NPEX continuum model with an additional blackbody component accounting for soft X-ray excess. Phase-resolved spectroscopy subsequently revealed that the marginal enhancement in additional column density seen at dip-phases of the pulse profile cannot be the cause of hard X-ray absorption dips. Among other possible causes, the geometrical effect is seen as plausible for the presence of dips in the pulse profiles of KS 1947+300 in hard X-rays. The absence of absorption dips in soft X-ray pule profiles could be due to soft X-ray excess flux pulsating in phase with the pulsar. The detection of this emission excess also confirmed that the emitting region is close to the neutron star i.e. near the accretion column. We have also estimated magnetic field of the pulsar by using observed spin-up rate during the *Suzaku* and *NuSTAR* observations and found it to be 1.2×10^{12} G. Similar value was reported independenly from cyclotron line measurement.

Chapter 4

Timing and spectral studies of EXO 2030+375 during X-ray outbursts

In the present Chapter, results obtained from a detailed and extensive study of timing & spectral properties of Be/X-ray binary pulsar EXO 2030+375 are discussed. For this work, we have used *RXTE* monitoring observations during its giant X-ray outburst in 2006 and numerous normal outbursts spanned over a decade. During these observations, the pulsar luminosity was variable by about an order of two which presented an oppertunity to carry out a thorough investigation of source properties during different X-ray outbursts and at different luminosities. The pulse profile variations in EXO 2030+375 were studied extensively in a wide range of accretion luminosity of the pulsar. The details are described in the following sections.

4.1 Be/X-ray binary pulsar EXO 2030+375

Be/X-ray binary pulsar EXO 2030+375 was discovered with *EXOSAT* observatory during a giant X-ray outburst in 1985 (Parmar et al., 1989a). The observations during the same outburst revealed the pulsating nature of the neutron star with a spin period of 42 s along with an orbital modulation of 44.3–48.6 days. The transient nature of the pulsar was revealed during these observations. The 1-20 keV luminosity of the pulsar was observed to change by a factor of $\geq$2500 from quiescence over a duration of 100 days. A significant spin-up ($-P/\dot{P} \sim 30$ yr) of the pulsar was also observed during the *EXOSAT* observations (Parmar et al., 1989a), suggesting the presence of an accretion disk. Using optical and infrared observations, the counterpart of the compact object was discovered as a highly reddened B0 Ve star located at a distance of 7.1 kpc (Coe et al., 1988; Motch and Janot-Pacheco, 1987; Wilson et al., 2002). Stollberg (1997) derived orbital parameters of the binary system by using long term *BATSE* monitoring data. The orbital period was determined more precisely and found to be 46 days. Strong luminosity dependent pulse profile was seen during the 1985 outburst (Parmar et al., 1989b). At higher luminosity, the pulse profile of the pulsar was characterized by two peaks (main peak and a minor peak) separated by a phase difference of $\sim$0.5. The strength of these two peaks was found to alter when the source luminosity decreased by a factor of $\sim$100. This observed change in strength and structure of each of the peaks in the pulse profile with luminosity was attributed to the change in the emission beam pattern e.g. from fan beam to pencil beam geometry (Parmar et al., 1989a).

EXO 2030+375 is a unique BeXB pulsar which shows regular Type I X-ray outbursts at the periastron passage (Wilson et al., 2002). At the peak of the Type I outbursts observed with the *RXTE* in 1996–2006, source flux was approximately 100 mCrab. A correlation between the spin frequency and luminosity indicated that the pulsar was spinning-up during brighter outbursts in 1992-1994. On the other hand, a spin-down trend was observed during low luminous outbursts in 1994–2002 (Wilson et al., 2005, 2002). EXO 2030+375 was caught into a giant outburst in June 2006 with the source flux peaking up to $\sim$750 mCrab (Krimm et al., 2006). During this giant outburst which lasted for about 140 days, the neutron star showed a remarkable spin-up behaviour (Wilson et al., 2008). After this outburst, many intense Type I X-ray outbursts ($\leq$300 mCrab) were detected for a number of orbits till the source settled to its regular mode. Since early 2015, however, the pulsar had undergone into a period of low activity for more than a year. The peak flux drastically came down during this phase and hardly any X-ray enhancement was seen at the expected periastron epochs (Fuerst et al., 2016). Recent observations with *Swift*/XRT and *NuSTAR* after March 2016, however, confirmed the recurrence of X-ray activity (Type I X-ray outbursts) along with spin-down trend in the neutron star (Kretschmar et al., 2016).

The energy spectrum of pulsar obtained from the 1985 giant outburst was described by a power-law model along with thermal blackbody component at 1.1 keV (Sun et al. 1994 and reference therein). However, an absorbed power-law modified with high energy cutoff model was widely used in later observations of EXO 2030+375 during Type I and Type II outbursts (Reig and Roche, 1999; Wilson et al., 2008). Apart from the 6.4 keV iron florescence emission line, detection of cyclotron absorption line was reported at three different energies such as $\sim$11, 36 and 63 keV in pulsar spectra obtained from *RXTE* and *INTEGRAL* observations during different X-ray outbursts (Klochkov et al., 2008; Reig and Roche, 1999; Wilson et al., 2008). However, *Suzaku* observations during 2007 May-June and 2012 May Type I X-ray outbursts did not confirm the presence of any such features in the pulsar spectrum (Naik, 2013; Naik and Jaisawal, 2015). Above *Suzaku* observations also revealed some other interesting aspects. Along with iron lines, several emission lines were also detected in the spectrum. It was the first time when an absorption dip was detected in the pulse profile up to as high as $\sim$70 keV (Naik, 2013). This was explained as due to the presence of additional dense matter (partial absorber) at certain spin phases of the pulsar. A peculiar narrow absorption dip was also detected in soft X-ray pulse profile obtained from *XMM-Newton* observation in 2014 May at a luminosity of $\sim 10^{36}$ erg s^{-1} (Ferrigno et al., 2016). This feature was interpreted as the effect of self absorption from accretion mount onto the neutron star surface.

In this thesis, we have carried out a detailed study of decade long *RXTE* monitoring observations of the pulsar over a wide range of luminosity. Investigations on the pulse profiles and corresponding spectral parameters were performed to understand the properties of the pulsar during Type I and Type II outbursts. Along with well known traditional models, we have also used a physical model (BW model; Becker and Wolff 2007; Ferrigno et al. 2009) to describe the continuum spectrum of EXO 2030+375. This model is based on thermal & bulk Comptonization of infalling plasma in the accretion column. We have used first time this model to understand the physical properties of accretion column across wide range of the pulsar luminosity. The application of physical model to describe the X-ray continuum of EXO 2030+375 is the subject of discussion of next chapter.

4.2 Observations and Analysis of EXO 2030+375

The transient X-ray binary pulsar EXO 2030+375 is a prototype of BeXBs exhibiting regular Type-I outbursts at each periastron passage of its $\sim 42\ d$ binary orbit. During the *RXTE* era, EXO 2030+375 was frequently observed during Type I outbursts to study a variety of pulsar emission properties characteristic to BeXBs. The decade long *RXTE* monitoring observations also include many pointed observations taken during the 2006 giant outburst of the pulsar. The peak X-ray flux during the Type I outbursts of the pulsar was $\sim$ 100 mCrab and during the June 2006 Type II outburst the peak X-ray flux observed from the pulsar was as high as $\sim$ 750 mcrab. It gives us an opportunity to understand the X-ray variability of the pulsar in wide range of pulsar flux and hence luminosity. In the present thesis, we have used all the *RXTE* archival observations of EXO 2030+375 since 1996 to 2011. A log of these observations is given in Table 4.1. During above period, there are a total of 606 pointing observations carried out at various epochs and phases of the Type I and Type II outbursts of the pulsar. The total effective exposure of these observations used in our present study amounts to $\sim$ 1.52 million seconds spanning over a period of 15 years. Apart from the *RXTE* observations of the pulsar mostly taken during X-ray outbursts, we have also used a *NuSTAR* observation taken during an extended unusual low X-ray activity of the pulsar in July 2015.

For timing studies, we used the *Standard-1* binned mode PCA data of the pulsar. With a timing resolution of 0.125 s provided by these binned mode data, we extracted source light curves in 2-60 keV range. For this, we used the *saextrct* task FTOOLS. The background data files were generated from the corresponding *Standard-2* data file with the help of *runpcabackest*[1] script and using the bright background model and SAA history file provided by the PCA team. These are obtained online from

[1] https://heasarc.gsfc.nasa.gov/docs/xte/recipes/pcabackest.html

Table 4.1 Log of *RXTE*/PCA observations of the pulsar EXO 2030+375 during Type I and Type II outbursts.

Year of Observations	Proposal ID	No. of Obs. (IDs)	Time range (MJD)	On Source time (ksec)
1996 Jul	P10163	18	50266.55 – 50274.56	67.42
1998 Jan	P30104	2	50825.02 – 50827.77	37.94
2002 Jun	P70074	21	52431.97 – 52441.47	76.91
2003 Sep	P80071	15	52894.44 – 52898.32	145.87
2005 Jun – 2006 Feb	P91089	52	53540.78 – 53776.28	145.57
2006 Mar – 2006 Nov	P92067, P91089, P92066	143	53816.96 – 54069.97	342.34
2006 Dec – 2007 Jun	P92422	147	54070.95 – 54279.51	221.91
2007 Jun – 2008 Oct	P93098	79	54280.56 – 54749.53	202.41
2008 Dec – 2009 Oct	P94098	40	54830.20 – 55114.49	92.55
2010 Jan – 2010 Nov	P95098	43	55197.87 – 55530.08	83.79
2011 Jan – 2011 Nov	P96098	46	55566.06 – 55895.74	106.68

RXTE guest observer facility [2]. Subsequently, these can be put through *saextrct* task to produce background light curves and spectra. For the spectral analysis, we used the *Standard-2* PCA data & the response files specific to each observation epoch were constructed by using the *pcarsp* task of *RXTE* FTOOLS. We have also analysed the HEXTE data during 2006 giant outburst observations to study the X-ray spectrum in hard X-rays. For this we used data from the HEXTE Cluster-B data of respective observations. We have followed the standard data analysis procedures[3] in reducing the HEXTE cluster data.

In case of *NuSTAR* observation of the source taken during July 2015, we used *NUSTARDAS* data processing software v.1.4.1 of HEASoft to reprocess the data. The initial data processing and filtering of event data from FPMA and FPMB modules were performed by using *NuSTAR* pipeline version 1.4.1 and HEASoft version 6.16. To select the source events from the focal plane modules, we used a circular region of 120″ around the source image centroid. The background events were chosen from the source free region with a 90″ radius. From these selected source and background events, corresponding light curves were extracted from the selected event data. The photon arrival times in the source light curves were corrected to that of the solar system barycenter and to nullify the effects of orbital motion the satellites and the

[2] https://heasarc.gsfc.nasa.gov/docs/xte/pca_news.html
[3] https://heasarc.gsfc.nasa.gov/docs/xte/recipes/hexte.html

Earth. This is done by using the barycentric correction FTOOL *faxbary* on the PCA extracted source light curves. In case of *NuSTAR* data, the *nuproducts* script used to generate the source and background light curves including the spectra. With the additional input parameter 'barrycor=yes' while running the *nuproducts* scripts, the source light curves and spectra are barycenter corrected. A detailed description for processing and analysis of *NuSTAR* data can be found in *NuSTAR* data analysis web pages[4] and software users guide, v1.9.3[5].

4.2.1 Luminosity dependent pulse profiles

We have estimated the spin-period of the pulsar in EXO 2030+375 at all epochs of *RXTE* observations using *efsearch* method (as described in Section **??** of Chapter 2). The folding epochs of pulse profiles were chosen close to the start of respective observation such that the pulse profile minima is aligned among the pulse profiles for better comparison. We were motivated by the various emission geometries exhibited by the BeXBs at different pulsar luminosity. The variation in the shape of pulse profiles at wide range of pulsar luminosity could be a possible proxy to probe the emission geometries seen in the pulsars. With this hindsight, we have generated the 2-60 keV pulse profiles at wide range of pulsar luminosity. In the Figure 4.1, we show the pulse profiles of EXO 2030+375 observed at source luminosity in $\sim 3.8\times10^{36}$ to 2.6×10^{38} $\mathrm{ergs\,s^{-1}}$. The X-ray luminosity of the pulsar as indicated on the left side of the each of the panels in Fig. 4.1 was based on the spectral fitting model used to describe the pulsar spectra of corresponding epoch. This is discussed in next chapter.

Strong luminosity dependence of the pulse profiles can be clearly seen from the Fig. 4.1. At lower luminosity ($\sim 10^{36}$ $\mathrm{ergs\,s^{-1}}$), there is a significant peak near 0.3 pulse phase of the profile with a minor peak near 0.7 phase. Also the presence of dip like structure below 0.2 phase is visible. In the pulse profiles with increasing source luminosity, it can be noticed that the secondary sub-peak starts evolving. At the source luminosity of $\sim (4-7)\times10^{37}$ $\mathrm{ergs\,s^{-1}}$, it is comparable to the primary

[4]https://heasarc.gsfc.nasa.gov/docs/nustar/analysis/
[5]https://heasarc.gsfc.nasa.gov/docs/nustar/analysis/nustar_swguide.pdf

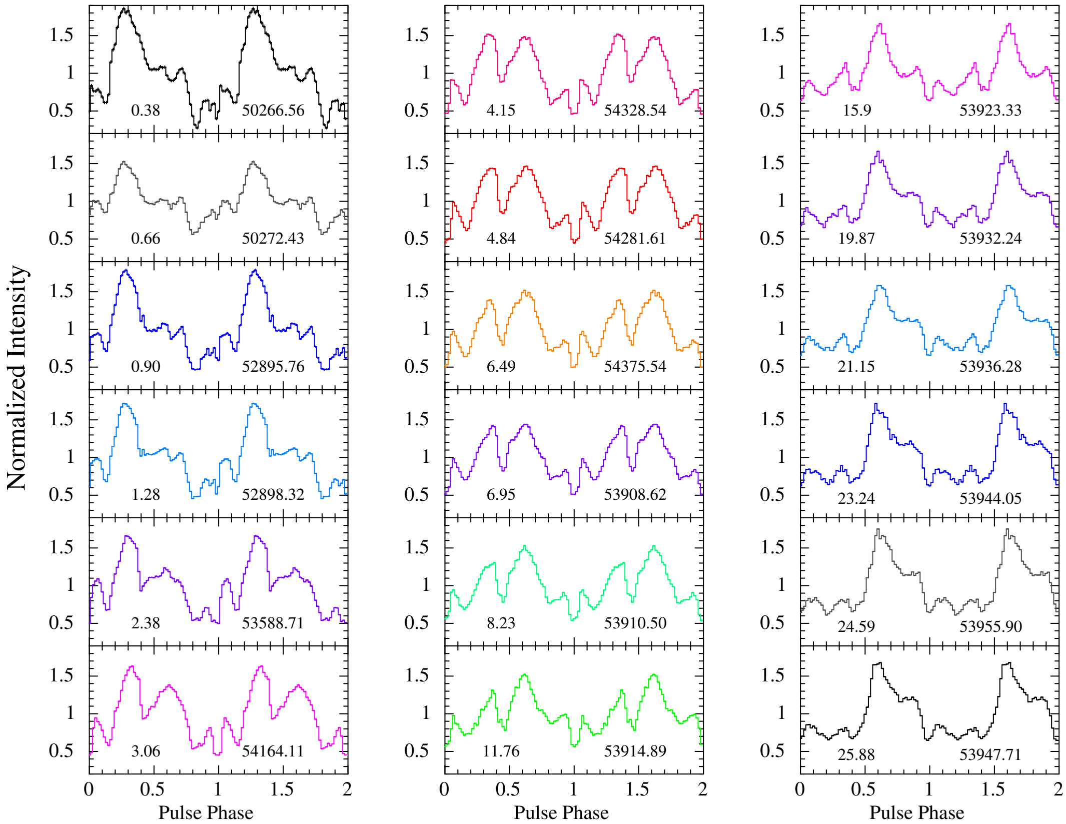

Fig. 4.1 The 2-60 keV pulse profiles of EXO 2030+375 obtained from *RXTE*/PCA light curves in wide range of pulsar $\mathrm{ergs\,s^{-1}}$seen at various epochs and phases of Type I outbursts and during 2006 Type II outburst of the pulsar. The pulse profiles are arranged in increasing order of source luminosity. The value of pulsar luminosity in 3-30 keV (in units of 10^37 $\mathrm{ergs\,s^{-1}}$) is shown in the left side of each panel. The respective epoch of observation (given in units of MJD) used to fold the light curves is shown in the right side of each panel.The errors bars in the pulse profiles represent the 1σ uncertainities. Two pulses of each pulse profile are shown in the figure.

peak (seen at ~ 0.3 pulse phase). With further increase in the source luminosity, the strength of the first peak gradually weakens and disappears from the pulse profiles at luminosities $\geq 1.6 \times 10^{38}$ $\mathrm{ergs\,s^{-1}}$. During the course of evolution of the pulse profile with luminosity, there were multiple absorption dips appearing in certain pulse phases of the pulsar. If we observe the structure of the pulse profile at either extreme of the observed source luminosity (first and last panels of Fig. 4.1), they are relatively similar except with a significant overall phase shift.

Comparison of pulse profiles during Type I and Type II outbursts

As we have seen in the Section 1.2.2 of Chapter 1, the properties of Type-I and Type II outbursts in BeXBs differ significantly in terms of their occurrence and outburst peak luminosity and duration. The possible similarities or differences in the X-ray pulse profiles of BeXBs during these outbursts could explain the cause of various emission patterns in these pulsars. With the above motivation, we explored the pulse profiles of EXO 2030+375 at various epochs. The pulse profiles EXO 2030+375 extracted from several Type I outbursts were compared to that of the 2006 Type II outburst at similar source intensities. A comparison of these pulse profiles is shown in Fig. 4.2. From the figure, it is worth noting first that at comparable values of source luminosity, the shape of the pulse profiles are similar during both type of X-ray outbursts. Secondly, the evolution of pulse profiles with luminosity shows similar variations during Type I and Type II outbursts as illustrated in Fig. 4.1. An important conclusion that can be drawn from these comparisons is that the pulse profiles of EXO 2030+375 are independent of their outburst types and are highly dependent on the source luminosity.

Pulse profiles during different phases of Type II outburst

During the Type-II outburst of EXO 2030+375 in 2006 June, there were large number of pointed observations taken with *RXTE*/PCA. These observations covered the observation epochs from the beginning to declining phases of the giant outburst. We have made use of these ovservations to study the evolution of pulse profiles at similar source intensities during rising and decaying phases of the Type-II outburst. The prime motivation behind this was to confirm further the lumiosity dependence of pulse profile during the rare Type II outburst and to find out the possible changes in the pulsar emission beam geometry in EXO 2030+375. We were able to trace the beam fuction of the pulsar at both the inclining and declining phases of the giant outburst by generating pulse profiles at similar source luminosities at these phases. The source luminosity in 3-30 keV during these epochs was in the range of $10^{37} - 10^{38}$ $\mathrm{erg\,s^{-1}}$. In Fig. 4.3, the pulse profiles of EXO 2030+375 at similar

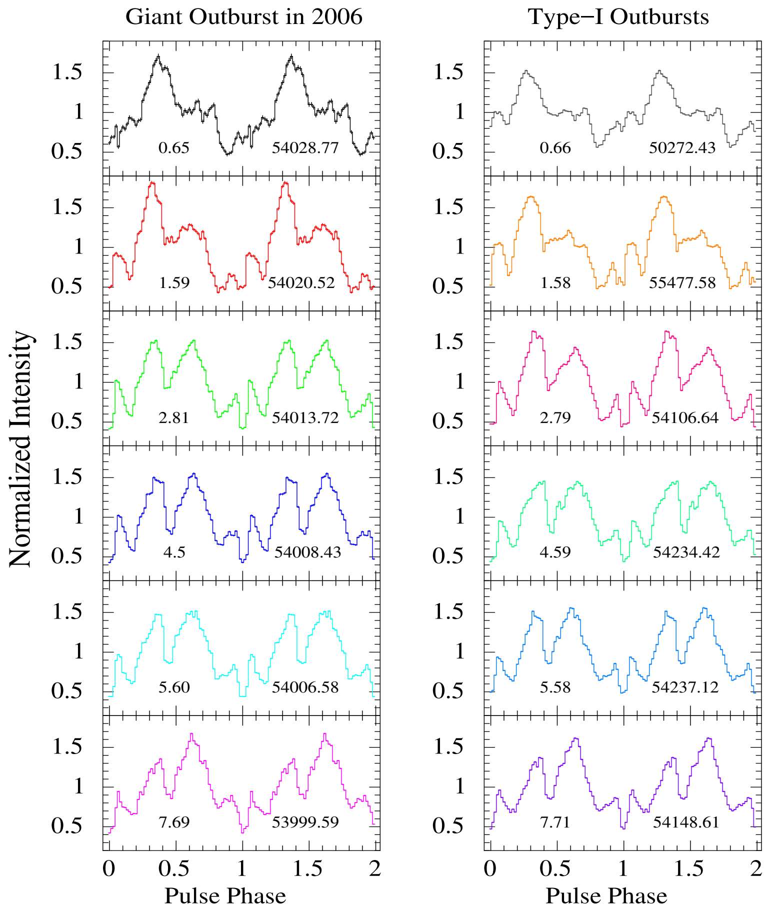

Fig. 4.2 The 2-60 keV RXTE/PCA pulse profiles of EXO 2030+375 during 2006 giant outburst (shown in the left side panels) are compared with those during Type I outburst (panels in the right side) at similar values of pulsar luminosity. The values of pulsar luminosity in 3-30 keV (in units of 10^37 ergs s^{-1}) is quoted in the left side of each panel. The start of corresponding epoch of observation (in MJD) is quoted in the right side of each panel.The errors bars in the pulse profiles represent the 1σ uncertainties. Two pulses of each pulse profile are shown in the figure.

luminosity are shown for the the duration of 2006 Type II outburst during its rising and declining phases in the left and right side panels, respectively. From these pulse profile studies, it becomes quiet evident that the pulse profiles at similar values of pulsar luminosity show similar shapes and are independent of the phases of Tyep II outburst. Thus, it further confirms strong luminosity dependence of pulse profiles in EXO 2030+375 at wide range of pulsar luminosity. Also the pulse profile shapes are independent of the outburst types and phases.

The pulse profiles of EXO 2030+375 were studied at various phases of Type I and Type II outbursts from observations carried out during the *RXTE* era. During

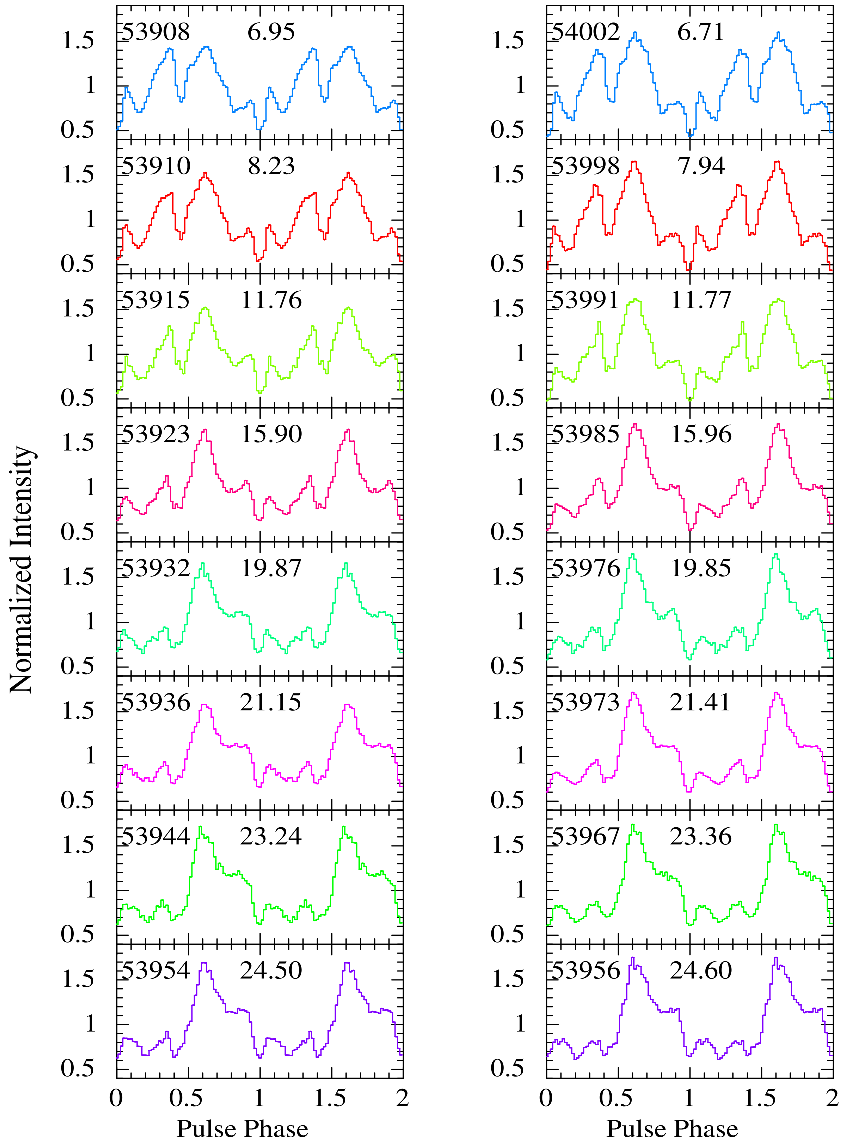

Fig. 4.3 The 2-60 keV RXTE/PCA pulse profiles of EXO 2030+375 during progressing phase of 2006 giant outburst are shown in the left side panels. These are compared with pulse profiles at similar luminosity seen during declining phase of the Type II outburst as shown in the corresponding panels in the right. The values of pulsar luminosity in 3-30 keV (in units of 10^{37} $\mathrm{ergs\,s^{-1}}$) is shown in the middle of each panel. The start of corresponding epoch of observation (in MJD) is quoted in the right side of each panel. The error bars in the pulse profiles represent the 1σ uncertainties. Two pulses of each pulse profile are shown in the figure.

these episodes of outbursts, the luminosity regime in which these pulse profiles were generated, spans in the range of $\sim 10^{37} - 10^{38}$ $\mathrm{ergs\,s^{-1}}$. However, since early 2015 the recurrence of Type I outbursts in EXO 2030+375 discontinued. The absence of X-ray activity of the pulsar during this phase was also seen from the

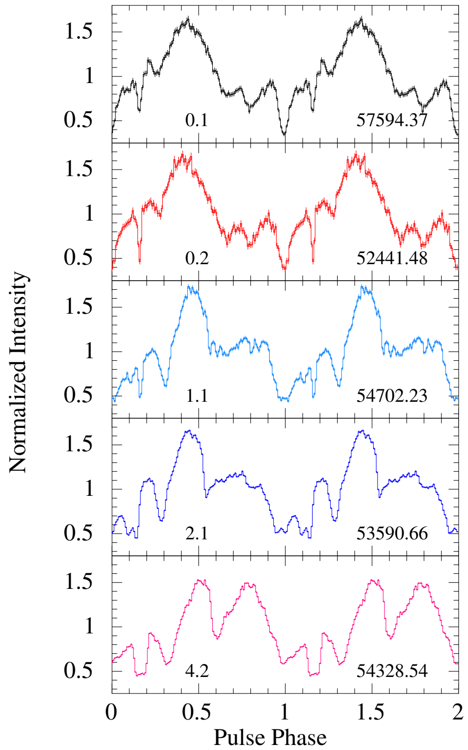

Fig. 4.4 Evolution of a narrow peculiar absorption dip (in 0.1-0.2 phase range) seen in the pulse profiles of EXO 2030+375 at low X-ray luminosity. The pulse profile in the top panel is taken from *NuSTAR* observations. The pulse profiles in the other panels are obtained from RXTE/PCA observations of the pulsar. The 3-30 keV X-ray luminosity (in units of 10^{37} $\mathrm{ergs\,s^{-1}}$) of the pulsar is quoted in the left side of each panel. The beginning of corresponding observation epochs (in MJD) are quoted in the right side of each the panel.

on-board X-ray monitors such as *Swift*/BAT, MAXI and *Fermi*/GBM. The low X-ray activity of the pulsar lasted for about an year. Later on, by the end of 2016, the normal Type I outbursts of the pulsar were resumed. During this prolonged low X-ray flux state of the pulsar, *NuSTAR* observed the source for $\sim$ 51 *ks*. From this observation, we generated pulse profiles of the pulsar. The luminosity of the pulsar in 3-30 keV during this observation was $\sim 10^{36}$ $\mathrm{ergs\,s^{-1}}$. This is the lowest luminosity of EXO 2030+375 in which X-ray pulsations were seen. The spin period of the pulsar during this epoch was found to be 41.2932(2) s.

In the top panel of Fig. 4.4, the pulse profile of EXO 2030+375 obtained from the *NuSTAR* observation during the low activity of the pulsar is shown. We have also compared the shape of the pulse profile with other low luminosity pulse profiles taken during different epochs of *RXTE* observations. These profiles are arranged in increasing order of luminosity in the figure. We noticed that at low luminosity of the pulsar, a peculiar narrow dip feature appears in the pulse profiles in 0.1-0.2 pulse phase range. The sharp absorption dip feature was found to be evolving with luminosity. We were able to trace evolution of dip structure up to luminosity $\leq 4 \times 10^{37}$ ergs s^{-1}. However, at higher values of pulsar luminosity the narrow feature vanishes into a broader dip structure in the pulse profile (bottom panel of Fig 4.4).

4.3 Phase Averaged Spectroscopy

To probe the spectral characteristics of the pulsar at different luminosities, we carried out spectral studies by using data from *RXTE* observations. Source and background spectra were extracted by following standard procedure as described in Section 2.1 for all the *RXTE* observations mentioned in Table 4.1. Using appropriate background spectra and response matrices, the source spectra from PCA detector were fitted by using *XSPEC* package. Data in 3–30 keV range were used in the spectral fitting. A systematic uncertainty of 0.5% was added to the data. While fitting the data, we explored several continuum models that are used to describe the energy spectrum of accretion powered X-ray pulsars. These models are high-energy cutoff power-law, cutoff power-law, negative and positive exponential cutoff power-law and with more physical model such as CompTT. In our analysis, we used an absorbed power-law model with a high-energy cutoff to describe the continuum spectrum of the pulsar. This model has been frequently used to express the broad-band spectrum of EXO 2030+375 (Reig and Roche, 1999; Wilson et al., 2008).

It has been recently found that the continuum of Be/X-ray binary pulsars is noticeably affected by the presence of additional matter at certain pulse phases during outbursts that can not be simply explained by a single absorber (Jaisawal et al., 2016; Naik, 2013). A partial covering absorption component along with the continuum model is generally used to describe the pulsar spectrum in phase-averaged as well as phase-resolved spectroscopy. In our fitting, a high energy cutoff power-law model was unable to fit the observed spectrum, specifically during bright phases of

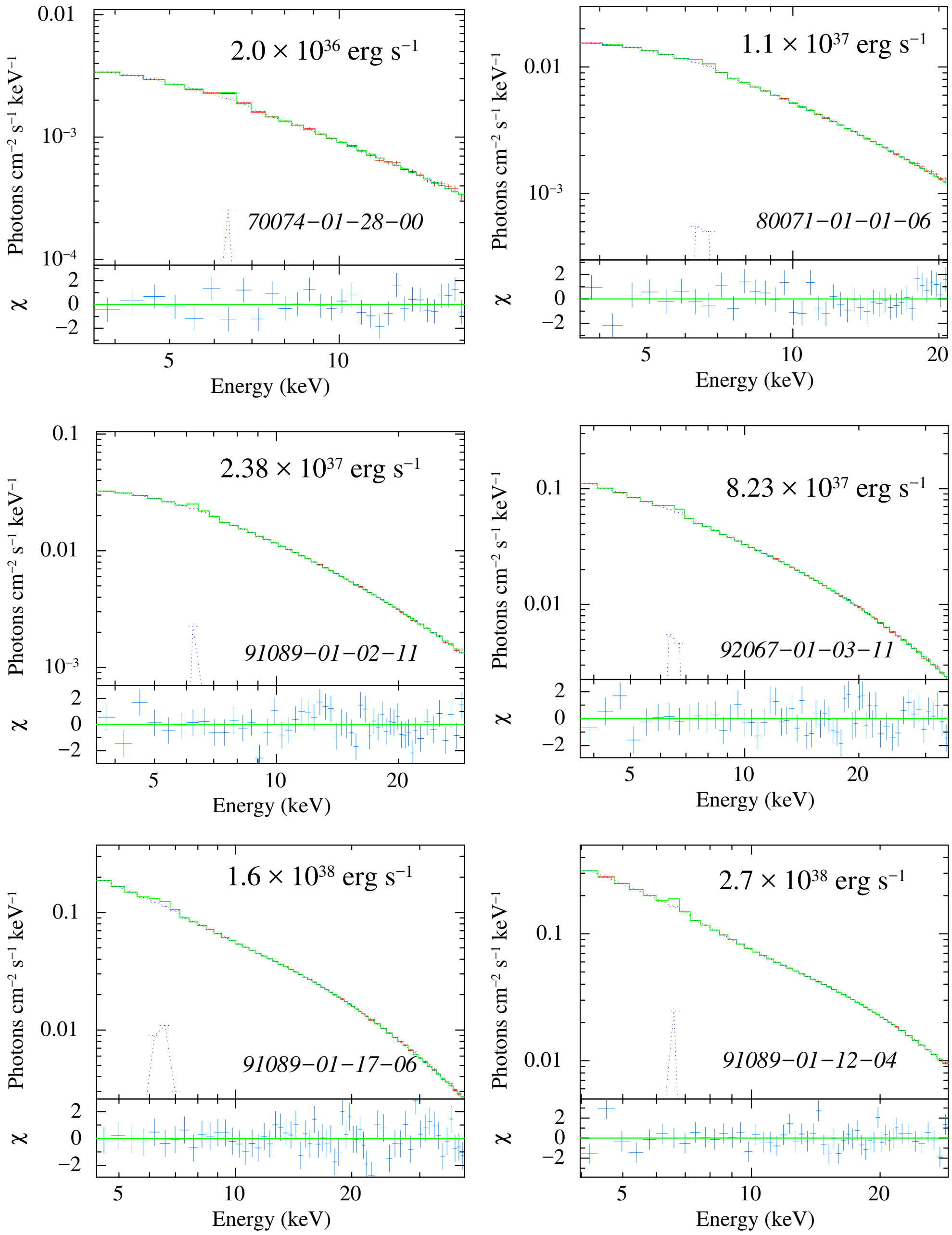

Fig. 4.5 Phase-averaged energy spectra of EXO 2030+375 at different luminosity levels, obtained from six epochs of *RXTE* observations during Type I and Type II X-ray outbursts. The spectra were fitted with partial covering high energy cutoff model along with an iron emission line at ∼6.4 keV. The source spectrum and best-fit model are shown in the top panel whereas the contribution of residuals to χ^2 at each energy bin are shown in the bottom panel for each epoch of *RXTE* observation. The observation IDs (in italics) and corresponding source luminosity are quoted in the figure.

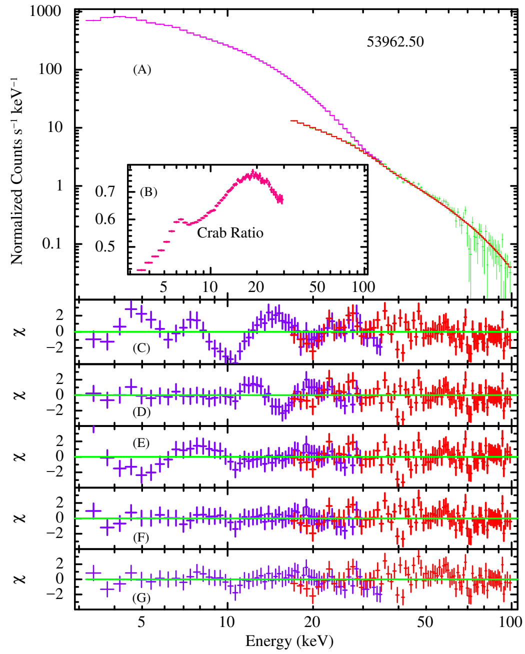

Fig. 4.6 The 3-100 keV energy spectra of EXO 2030+375 obtained from PCA and HEXTE detectors of *RXTE* at the peak of 2006 giant outburst (MJD 53962.50). Source spectra along with the best fitting model e.g. a partial covering high energy cutoff model along with a Gaussian function for iron emission line (Panel A) and corresponding spectral residual (Panel G) are shown. Panels C, D, E and F indicate the spectral residuals obtained by fitting pulsar spectra with a (i) high energy cutoff model, (ii) high energy cutoff model with a blackbody, (iii) CompTT with a blackbody and (iv) a partial covering CompTT model with blackbody component, respectively, along with interstellar absorption component and a Gaussian function for iron emission line at 6.4 keV. Any signature of cyclotron absorption line at previously reported value of ∼11 keV is not seen in the spectral residuals. The Crab-ratio (Panel B) also did not show any such feature in 10-20 keV range.

the outbursts. Addition of a partial covering component improved the fitting further and yielded an acceptable value of reduced-χ^2 (∼1). The iron fluorescence emission line at ∼6.4 keV was also detected in the pulsar spectrum. A partially covering absorbed power law with high-energy cutoff model can be mathematically expressed as

$$N(E) \quad = \quad e^{-N_{\rm H1}\sigma(E)}(K_1 + K_2 e^{-N_{\rm H2}\sigma(E)})\; f(E)$$

Table 4.2 Best-fitting spectral parameters with 1σ errors obtained from *RXTE/PCA* observations of EXO 2030+375 at six different luminosities. The best-fit model consists of a partial covering high-energy cutoff power-law model with a Gaussian component.

Parameters	Observation IDs					
	70074-01-28-00	80071-01-01-06	91089-01-02-11	92067-01-03-11	91089-01-17-06	91089-01-12-04
N_{H1}[a]	5.9±0.8	6.2±0.5	5.2±0.3	2.8±0.5	1.5±0.4	3.41±0.25
N_{H2}[b]	–	–	–	139.3±17.5	166.5±5.5	241.9±4.0
Covering fraction	–	–	–	0.25±0.02	0.35±0.01	0.45±0.01
Photon Index (Γ)	1.72±0.06	1.45±0.06	1.34±0.03	1.43±0.05	1.61±0.02	1.80±0.03
E_{cut} (keV)	8.2±0.8	7.6±0.4	7.7±0.2	8.0±0.3	8.2±0.2	7.8±0.2
E_{fold} (keV)	31.9±5.6	23.3±1.8	23.3±0.8	21.2±0.9	23.5±0.5	25.7±0.8
Emission lines						
Fe $K\alpha$ line energy (keV)	6.32±0.16	6.50±0.11	6.33±0.05	6.51±0.08	6.43±0.03	6.52±0.04
Width of Fe line (keV)	0.1	0.1	0.1	0.15	0.31±0.07	0.1
Source flux						
Flux[c] (3-10 keV)	0.17±0.03	0.88±0.09	1.8±0.9	6.6±0.7	13.8±0.7	25.0±1.5
Flux[c] (10-30 keV)	0.16±0.02	0.94±0.10	2.2±0.1	7.1±0.8	12.7±0.6	19.4±1.2
Flux[c] (3-30 keV)	0.33±0.04	1.82±0.19	4.0±0.20	13.7±1.4	26.5±1.3	44.4±2.6
Source Luminosity						
L_X[d] (3-30 keV)	0.20±0.03	1.10±0.12	2.38±0.14	8.23±0.89	15.96±0.90	26.77±1.72
Reduced χ^2(*d.o.f*)	0.99 (24)	1.01 (34)	1.04 (46)	1.00 (50)	1.08 (53)	1.11 (43)

Notes: [a] : Equivalent hydrogen column density (in 10^{22} atoms cm^{-2} unit); [b] : Additional hydrogen column density (in 10^{22} atoms cm^{-2} unit); [c] : Absorption corrected flux in unit of 10^{-9} ergs cm^{-2} s^{-1}; [d] : The 3-30 keV X-ray luminosity in the units of 10^{37} ergs s^{-1} assuming a distance of 7.1 kpc to the source.

where

$$
\begin{aligned}
f(E) &= E^{-\Gamma} && for\ E < E_c \\
&= E^{-\Gamma} e^{-\left(\frac{E-E_c}{E_f}\right)} && for\ E > E_c
\end{aligned}
$$

Here, *f(E)* represents the high energy cutoff power-law model with photon index Γ, E_c and E_f are the cutoff and folding energies in keV, respectively. The normalization constants K_1 & K_2 are in the units of photon keV^{-1} cm^{-2} s^{-1}. N_{H1} & N_{H2} are the equivalent hydrogen column density and the additional column density (in units of 10^{22} atoms cm^{-2}), respectively. $\sigma(E)$ is the photoelectric absorption cross-section. The energy spectra of EXO 2030+375 along with the best-fitting model (top panel) and residuals (bottom panel) for six epochs of *RXTE* observations are shown in Figure 4.5. Observation ID.s and 3-30 keV pulsar luminosity during these observations are quoted in the figure. The best-fitted parameters obtained from spectral fitting of data obtained at these epochs are given in Table 4.2.

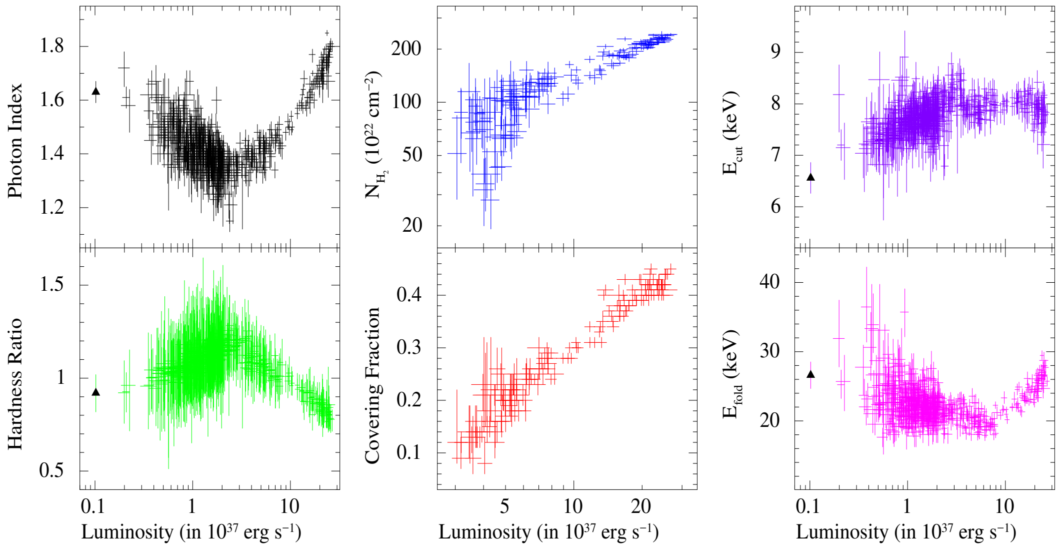

Fig. 4.7 Spectral parameters such as photon index (top left panel), additional column density (top middle panel), cutoff energy (top right panel), covering fraction (bottom middle panel) and folding energy (bottom right panel) obtained from the spectral fitting of *RXTE* observations of EXO 2030+375 with a partial covering high energy cutoff power-law model during Type I and Type II outbursts, are shown with the 3-30 keV luminosity. Hardness ratio (ratio between 10-30 keV flux and 3-10 keV flux) with luminosity is also shown in bottom left panel of the figure. The parameters from *NuSTAR* observation are marked with empty triangles. The error bars quoted for 1σ uncertainties.

During 2006 June outburst, detection of a cyclotron absorption line like feature at $\sim$11 keV in the pulsar spectrum was reported earlier (Wilson et al., 2008). We used same observation in the present study to investigate the cyclotron line feature in the pulsar spectrum. During this outburst, as the pulsar luminosity was very high, data from PCA and HEXTE detectors were used to get a broad-band spectral coverage. The 3-100 keV broad-band spectrum, obtained from the *RXTE* observation of the pulsar on MJD 53962.5 (2006 August 15) was fitted with a high energy cutoff power-law model yielding a poor fit with a reduced χ^2 of $>$8. A broad absorption-like feature at $\sim$10 keV was detected in the spectral residual (Panel C of Figure 4.6). Various combination of models such as high energy cutoff power-law, CompTT, NPEX along with other components such as blackbody or a partial absorber were used to test reliability of the reported line. Addition of a partial covering component to the above continuum models resolves the broad feature with a reduced-χ^2 close to 1. Therefore, a high energy cutoff model along with a partial covering component was used as best-fit model in our analysis. We generated Crab-ratio to check the presence of absorption like feature in the pulsar spectrum. The Crab-ratio was obtained by normalizing the pulsar spectrum with the feature-less power-law spectrum of Crab pulsar to remove the presence of any uncertainties related to calibration and model (see also Jaisawal et al. 2013). This ratio showed a highly absorbed spectrum along with a 6.4 keV iron emission line below 10 keV. We did not find any signature of absorption feature in 10-20 keV range in the Crab-ratio (Panel B of Figure 4.6). Residuals obtained from fitting the pulsar spectra with different continuum models are shown in panels C, D, E and F of Figure 4.6. The absence of any absorption like feature in 10-20 keV range can be clearly seen in above panels. To check the presence/absence of this absorption like feature, we fitted 3-79 keV broad-band spectrum of EXO 2030+375 obtained from a *NuSTAR* observation during an extended period of low activity in 2015 with a high energy cutoff model. Any emission/absorption like features was not seen in the spectrum.

Spectral parameters such as power-law photon index, cutoff energy, folding energy, additional column density (NH_2), covering fraction, hardness ratio (ratio between 10-30 keV flux and 3-10 keV flux) obtained from spectral fitting of all *RXTE* observations of EXO 2030+375 are shown with corresponding 3-30 keV luminosity in Figure 4.7. All these parameters showed intriguing trends with luminosity which had not been explored earlier. In the figure, one can notice that the values of power-law photon index are distributed in three distinct regions such as negative, constant, and positive correlations with source luminosity which suggest a direct measure of spectral transition in EXO 2030+375. At lower luminosity ($\leq 10^{37}$ erg s^{-1}), the pulsar spectrum was relatively soft. A negative correlation between the power-law photon index and luminosity can be clearly seen for this regime. The value of photon index was found to varying between 1.2 and 1.8 (first panel of Figure 4.7). When the luminosity was in the range of 2–4$\times 10^{37}$ erg s^{-1}, the distribution of values of photon index did not show any dependence on source luminosity. With increase in source luminosity, the photon index showed a positive correlation. It is, therefore, clear that the pulsar changes its spectral behavior with change in luminosity. Flux ratio (ratio between flux in 10-30 keV range and 3-10 keV range) also showed smooth transition with increase in pulsar luminosity (left bottom panel of Figure 4.7).

As mentioned earlier, while fitting spectra from high flux level of the outbursts, a partially absorbed component was included in the fitting model. This was required in spectral fitting when the pulsar luminosity was above 3×10^{37} erg s^{-1}. In our spectral fitting, the maximum value of additional column density (NH_2) obtained was as high as 250×10^{22} cm^{-2} which is significantly larger than the value of equivalent hydrogen column density in the source direction. From our fitting, the values of additional column density and covering fraction were found to be strongly luminosity dependent (middle panels of Figure 4.7). The cutoff energy and folding energy did not show any noticeable changes with the pulsar luminosity (last panels of Figure 4.7). The parameters obtained from *NuSTAR* observation are also included in the figure.

4.4 Results & Discussion

The pulse profiles of the BeXB pulsar EXO 2030+375 showed distinct patterns of variations with luminosity. Over a braod range of pulsar luminosity (i.e from $\sim 10^{36}$ to $\sim 10^{38}$ ergs s^{-1}), the shape of the average pulsar profiles of EXO 2030+375 in 2-60 keV have been investigated by using numerous RXTE pointing observations. From these extensive studies, a strong luminosity dependence of pulse profiles of the pulsar across Type I and Type II outbursts is confirmed. Previous studies of the pulsar with different observatories also established the dependence of the pulse profile variations on the pulsar luminosity (Klochkov et al., 2008; Naik, 2013; Naik and Jaisawal, 2015; Parmar et al., 1989a). However from our timing stuides of EXO 2030+375, an interesting trend in the pulse profiles is emerged. It is observed that the pulse profiles of EXO 2030+375 at similar values of pulsar luminosity are found to be identical in shape. Secondly, the structure of the pulse profiles does not depend upon the outburt types (i.e Type I or Type II) or different phases i.e rising or declining phases of the outbursts. Although the Type II outbursts are rare and unpredictable, we have seen that the pulse profiles of the pulsar during Type I and Type II outbursts at similar values of pulsar luminosity showed similar variations. This signifies that the pulsar emission beam pattern in case of EXO 2030+375 does not change during the two types of X-ray outbursts. Rather, its the accretion luminosity (or change in mass accretion rate during the outbursts) that plays a dominant role in shaping the pulse profiles. At low X-ray luminosity state of the pulsar (i.e $L_x \leq 10^{37}$ $\mathrm{ergs\,s^{-1}}$), the mass accretion on to the neutron star is also expected to be low. The X-ray emission in this case appears to occur from the neutron star hotspot closer to the magnetic poles as the accreting gas freely falls onto it. The resulting emission beam is that of a pencil-beam originating from the hot thermal mound at the base of accretion column and extending along the magnetic axis. The result of this beamed emission geometry leads to formation of single peaked pulse profiles, as seen in our present study of low luminosity pulse profiles in EXO 2030+375. In high luminosity state of the pulsar, due to the formation of a radiation dominated shock in the accretion column, the pulse profiles changed from a single peaked profile to a double peaked structure. However, in the intermediate luminosity range, a mixture of fan beam and pencil beam emission components can contribute equally towards the double peaked structures of the pulse profiles. This is indeed the case seen in the pulse profiles of EXO 2030+375 in the luminosity range of $\sim (3-12)\times 10^{37}$ $\mathrm{ergs\,s^{-1}}$. We interpret this to be the critical luminosity regime of the BeXB pulsar EXO 2030+375. In the Type II outbursts, the pulsar luminosity surpasses the critical luminosity due to enhanced mass accretion rate. As a result of which the height of the radiation shock shifts upward along the accretion column. This in turn, obstructs the accreting matter above the shock region due to build up of high radiation pressure (Becker and Wolff, 2007).The X-ray photons beyond this point diffuse through the side wall of the accretion column thereby forming a fan beam emission geometry (Klochkov et al., 2008). Using the above arguments, the high lumiosity (i.e $L_x > 1.2\times 10^{38}$ $\mathrm{ergs\,s^{-1}}$) pulse profiles seen in EXO 2030+375, could be originated from pure fan beam emission of the pulsar.

The shape of pulse profiles in BeXBs is generally complex due to the presence of several absorption dips and peaks in soft X-rays. In hard X-rays, the pulse profiles become single peaked. In order to understand the various emission components that are responsible for X-ray emission from the magnetic poles of the pulsar,Sasaki et al. (2010) modelled the energy resolved pulse profiles of EXO 2030+375 from the 2006 giant outburst. The asymmetric pulse profiles of EXO 2030+375 at different energies and luminosities were assumed to be an admixture two symmetric pulse profiles due to emission from two poles of the pulsar. As a result of which, the emission from two polar regions is observed partially and without any overlap. A moderate distortion in the magnetic field of the pulsar (and hence the deformity in the location of accretion column) was understood to be the cause of asymmetry in EXO 2030+375 pulse profiles. The presence of multiple absorption dips in certain phases of pulse profiles is also confirmed from *Suzaku* observartions of EXO 2030+375 taken during Type I outbursts in 2007 and 2012 (Naik, 2013; Naik and Jaisawal, 2015). From the phase resolved spectral studies, it was suggested that the narrow streams of additional matter present at these phases was causing the strong energy and luminosity dependent dips in the pulse profiles up to hard X-rays (i.e $\sim$ 70 keV) (Naik, 2013). The absorption dips are also seen among the outburst pulse profiles of other BeXBs such as A 0535+262 (Naik et al., 2008), GRO J1008-57(Naik et al., 2011b), GX 304-1 (Jaisawal et al., 2016). Apart from energy dependent dips in the pulse profiles of EXO 2030+375, presence of sharp dip-like features are also seen, particularly at low-luminosity (i.e $L_x \sim 10^{36}$ ergs s^{-1}regime) (Ferrigno et al., 2016). These were understood to be due to self-absorption from the accretion column. The presence of this peculiar sharp-dip is also seen in the low luminosity pulse profiles of EXO 2030+375 below the critical luminosity regime (i.e $< 4 \times 10^{37}$ ergs s^{-1}) in our present study. It may be the case that the pencil beam emission along the magnetic axis prevalent in low luminosity regime interacts directly with accretion column to produce such sharp dip like features in the pulse profiles. At higher accretion luminosity, the contribution of fan beam emission may change the overall emission geometry causing the absence of these features. From our present timing studies, we have also seen that the sharp 'V-shaped' feature indeed vanishes from the pulse profiles beyond the critical luminosity.

The broadband energy spectrum of accretion powered X-ray pulsar is known to be originated due to the inverse Comptonization of soft X-ray photons emitted from the hot spots on the surface (Becker and Wolff, 2007). The continuum is generally described with simple models such as high energy cutoff power law, NPEX, exponential cutoff power law etc., despite of the complex phenomenon occurring in the accretion column. We carried out spectral analysis of a large number of *RXTE* pointed observations of Be/X-ray binary pulsar EXO 2030+375, spanned over a decade by using a high energy cutoff power-law model along with a partial absorbing component and a Gaussian function for the 6.4 keV iron emission line. The *RXTE* observations of the pulsar provided opportunity to trace spectral evolution of the pulsar at various luminosity levels during Type I and Type II X-ray outbursts since 1996 to 2011. Parameters obtained from the spectral fitting showed very interesting variation with luminosity. The photon index was found to exhibit three distinct patterns with luminosity indicating signatures of spectral transition between sub-critical and super critical states. All three regimes are reflected in the pattern of the pulse profiles and are interpreted as due to different beam pattern at three different luminosity ranges.

A negative correlation was seen between power-law photon index and pulsar luminosity in sub critical regime (*i.e.*below the critical luminosity, as can be seen from first panel in Figure 4.7) where spectrum was relatively hard. In this condition, the broadband X-ray emission is considered to be originated from a hot mount on the neutron star surface (Basko and Sunyaev, 1976; Becker et al., 2012). Critical luminosity is associated with the transition between two accretion scenarios. In our study, we detected a plateau like region in the distribution of power-law photon index in luminosity range of $\sim$(2-4) $\times$ 10^{37} erg s^{-1}. This luminosity range can be considered as the critical luminosity for EXO 2030+375. The critical luminosity regime has been explored for other accretion powered X-ray pulsars such as 4U 0115+63, V 0332+53, Her X-1, A 0535+26 and GX 304-1 in luminosity range of $\sim$(2-8) $\times$ 10^{37} erg s^{-1} (Becker et al. 2012 and reference therein). A positive correlation between photon index and luminosity was detected above the critical luminosity. This occurs because of dominating role of shock in the accretion column which effectively reduces the velocity of energetic electrons. In this case, the pulsar spectrum appears soft due to lack of bulk Comptonization of photons with accreting electrons (Becker et al., 2012). A positive correlation between photon index and luminosity, therefore, is observed in super-critical regime. During 1985 giant outburst, the photon index was also proportional to the luminosity, indicating that the pulsar was accreting above the critical limit (Reynolds et al., 1993).

The hardness ratio (ratio between 10-30 keV flux and 3-10 keV flux) also showed similar kind of transition with luminosity. This showed an increasing trend till the pulsar luminosity reached its critical value beyond which a decreasing trend was observed. It showed that the pulsar emission was relatively hard in the sub-critical luminosity region. A softening in the spectrum was observed above the critical luminosity as discussed in above section. The folding energy was found to vary with luminosity. This spectral parameter represents the plasma temperature in the emission region. At lower luminosity, the value of folding energy was relatively constant although a few high values (with large errorbars) were also evident. The high values in sub-critical luminosity regime may correspond to the deep regions of accretion column. The value of folding energy was increasing beyond the critical luminosity. It is expected that on increasing mass accretion in super-critical region can produce the high temperature plasma in the presence of shock.

The magnetic field of the pulsar can be investigated by using observed cyclotron resonance scattering features in the broad-band spectrum. Cyclotron resonance scattering features appear due to the resonant scattering of electrons with photons in the presence of magnetic field (Caballero and Wilms, 2012). These absorption like features appear in the hard X-ray spectrum of accretion powered X-ray pulsars with magnetic field in the order of 10^{12} G. The detection of these features allow us to directly estimate the magnetic field of pulsar. Detection of a cyclotron absorption line at $\sim$11 keV in the pulsar spectrum obtained from *RXTE* observation was reported earlier (Wilson et al., 2008). Using same data set, we attempted to explore the cyclotron line feature further. However, our results showed that this feature was model dependent, only seen in a single cutoff based model. This discards the detection of cyclotron scattering feature in EXO 2030+375. The feature was also not detected in the pulsar spectra obtained from *NuSTAR* observation, though it was carried out during low intensity phase. Moreover, our studies based on BW model showed a constrain on pulsar magnetic field which is in the range of $\sim$(4–6)$\times 10^{12}$ G (it is discussed in the next chapter). For such strength of magnetic field, a cyclotron feature is expected to observed in the 40–60 keV energy range of pulsar spectrum. We have not observed any such features in the above energy range using *RXTE* observations, although a claim of cyclotron line at $\sim$36 or 63 keV have been made earlier in the pulsar (Klochkov et al., 2008; Reig and Roche, 1999). With high capability of new generation satellite such as *AstroSat* and *NuSTAR*, the cyclotron line features in EXO 2030+375 can be investigated during an intense X-ray outburst.

Chapter 5

Accretion column emission in EXO 2030+375: a physical perspective

The study of spectral properties of EXO 2030+375 by using empirical model such high-energy cutoff power-law model over a broad range of the pulsar luminosity, during Type I and Type II X-ray outbursts has enriched our understanding about beamed emission of the pulsar. A thorough and detailed spectral investigation of *RXTE* pointed observations of EXO 2030+375 carried out at different luminosities during different types of outbursts in a time span of over a decade showed that, depending on source luminosity, the power-law photon index was distributed in three distinct regions. It suggests the phases of spectral transition from sub-critical to super-critical regimes in the pulsar. A region with constant photon index was also observed in $\sim(2-4)\times10^{37}$ $\mathrm{ergs\,s^{-1}}$range, indicating critical luminosity regime in EXO 2030+375. The existence of this regime is also reflected in the pulse profile variations with luminosity as the emission geometry changed from a pure pencil beam emission at lower X-ray luminosity to a mixture of pencil and fan beam emission at critical luminosity. Despite our understanding of structural changes in column emission of the pulsar, we are still clueless of the physical properties of accretion column. The empirical models could not address fully the complex emission processes happening near the pulsar site which shape the accretion column. In order to comprehend the dynamics of radiative processes happening at these sites which also possess strong magnetic field ($\sim 10^{12} G$), a proper physical model accounting for all the source properties should be considered. In the present Chapter, we explore the accretion column emission properties of the BeXB pulsar EXO 2030+375. For the first time we have used a physical model (BW model;Becker and Wolff 2007; Ferrigno et al. 2009) to describe the continuum spectrum of EXO 2030+375. This model is based on thermal & bulk Comptonization of infalling plasma in the accretion column. It could describe the physical properties of accretion column across wide range of the pulsar luminosity.

5.1 Physical Spectral Model

The X-ray continuum spectra of accretion powered pulsars is a result of complex physical phenomena happening at the vicinity of pulsar accretion column. The incoming plasma entrained by the dense magnetic field into narrow regions of pulsar accretion column decelerates through a radiative shock before settling onto the neutron star surface. The deceleration causes the gas to fall at relativistic speed. This in turn causes the accreting matter to loose its enormous gravitational energy through emitting X-ray photons from the regions around the accretion column. The X-ray luminosity of accretion powered pulsars ranges in $L_x \sim 10^{34} - 10^{38}$ erg s^{-1} with the pulse periods varying in $0.1\ s \leq P_{spin} \leq 1000\ s$. The resulting spectra of the pulsars are often fitted with various forms of power-law and sometimes with the combination of a blackbody component (with temperature, $T \sim 10^6 - 10^7\ K$). In few of these sources, signatures of cyclotron line features in 10-100 keV range spectra are also seen apart from iron emission lines. Despite the fact that the broad-band X-ray spectra of accretion powered pulsars enrich with occasional emission or absorption features, there is no convincing physical model which could explain all the observed spectral components. There have been several attempts to calculate the spectra of these pulsars by considering the radiative processes happening at the accretion column. Recent developments in understanding the spectral formation in accretion powered pulsars has lead to many physical models which can explain the observed spectra. Among these the promising one is the thermal & bulk Comptonization model proposed by Becker and Wolff (2007). This model has been used in our spectral investigation of *RXTE* observations of EXO 2030+375 to estimate the characteristic parameters of the pulsar. This has been discussed below.

5.1.1 Thermal and Bulk Comptonization model

Radiative processes such as blackbody, Comptonization etc. play a major role in broad-band X-ray emission from accretion powered binary pulsars. The Comptonization process is also the primary mode of interaction between photons and electrons present in a radiation dominated plasma such as in accretion column. In order to explain the high energy spectrum comprising column emission from X-ray pulsars, Becker and Wolff (2007) developed a physical model based on 'bulk' and 'thermal' Comptonization of seed photons in the accretion column. The seed photons in turn were produced from the bremsstrahlung and cyclotron emission in the accretion column and from the blackbody emission emerging from thermal mound located near the neutron star surface. As the seed photons diffuse through the accretion column, they are scattered by infalling high speed electrons in the accreting plasma. The plasma settles onto the neutron star surface as the photons escaping through the column wall carry away the kinetic energy of the infalling gas. In the "pure" bulk Comptonization process, the seed photons gain energy as they collide with the rapidly compressing gas in the accretion column. The Comptonization process results in a mean energy gain by the seed photons as they collide with the scattering centers (i.e infalling electrons) within the accretion column. However, in thermal Comptonization, the seed photons are energized by 'stochastic' motions of electrons produced by second-order Fermi mechanism (Becker, 2003; Sunyaev and Titarchuk, 1980).

The Becker & Wolff (BW) model as proposed by Becker and Wolff (2007), consists of free parameters such as column radius (r_0), gas temperature in the thermal mound (T_{th}), electron temperature in the optically thin region above the thermal mound (T_e), strength of magnetic field (B) and mass accretion rate ($\dot{M}$). The number of free parameters gets reduced with additional constraints relating these

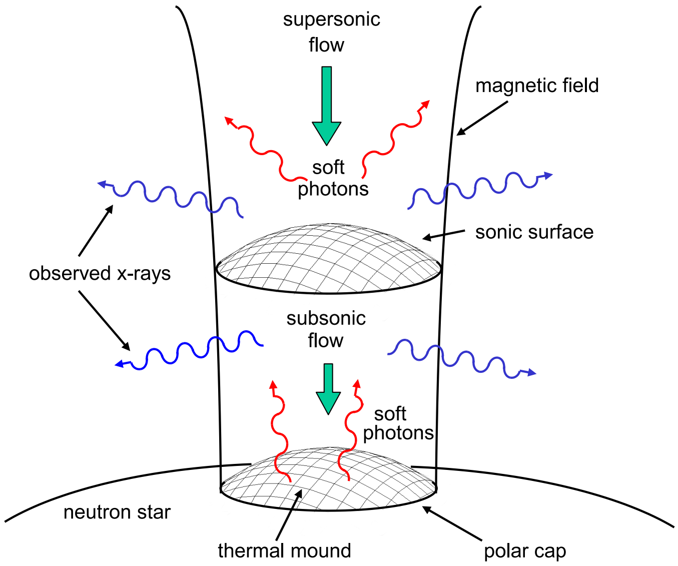

Fig. 5.1 Schematic representation of matter accretion onto the pole of a neutron star as depicted in (Becker and Wolff, 2007). A radiation dominated shock is formed above the neutron star surface before the accreting gas settles onto the neutron star surface. The dense thermal mound located inside the accretion column just above the surface is the source of most of the photons emitted from the column. The blackbody photons originated in the thermal mound are eventually upscattered in the shock and diffuse through the column walls. The settling of the thermal plasma onto the stellar surface is possible as the escaping photons carry away the kinetic energy of the gas.

parameters. In case of accretion powered X-ray pulsars, if we consider standard values of neutron star mass and radii as $M_NS = 1.4\,M_{\odot}$ and $R_{NS} = 10\,km$, respectively, then there are only 6 free parameters that need to be varied while fitting the broad-band spectrum. These are namely, $T_e, \dot{M}, r_0, B, \delta$ and ξ. Last two parameters such as the Comptonization parameter, δ and the photon diffusion parameter, ξ are defined as:

$$\xi \equiv \frac{\pi r_0 m_p c}{\dot{M}\sqrt{\sigma_{\perp}\sigma_{\parallel}}} \tag{5.1}$$

$$\frac{\delta}{4} = \frac{y_{\text{bulk}}}{y_{\text{thermal}}} \tag{5.2}$$

Here, m_p denotes the proton mass, c is the speed of light and $\sigma_{\perp}$ & $\sigma_{\parallel}$ are respectively the energy averaged scattering cross-sections of photons propagating perpendicular and parallel to the magnetic field. The y_{bulk} and y_{thermal} represent the

Compton y parameters due to *bulk−* and *thermal* Comptonization processes. The diffusion parameter δ subsequently signifies the leading Comptonization process in energizing the photons that are escaping from the accretion column as emerging X-ray radiation. For values of $\delta \gg 1$, the bulk Comptonization plays a major role in photon energization and for $\delta \ll 1$, the thermal Comptonization leads in energization of the escaping photons. At the values of diffusion parameter, i.e $\delta \sim 1$, the energy transfer between electrons and photons is equally led by the two Comptonization processes (Becker and Wolff, 2007).

5.1.2 BW model explaining the spectra of EXO 2030+375

To explore the physical properties of accretion column, we have fitted the Becker & Wolff (BW) model with the phase averaged spectra of EXO 2030+375 in wide luminosity range ($i.e.10^{36} \lesssim L_x \lesssim 10^{38}$ ergs s^{-1}). This model is proposed by Becker and Wolff (2007) to explain the emission from accretion powered X-ray pulsars by considering the effects of thermal and bulk Comptonization in accretion column. It has been successful in explaining the broadband spectra of bright X-ray pulsars such as 4U 0115+63 (Ferrigno et al., 2009), 4U 1626-67 (D'Aì et al., 2017), Her X-1 (Wolff et al., 2016). According to this model, seed photons originated due to bremsstrahlung, blackbody and/or cyclotron emissions undergo thermal and bulk Comptonization in the accretion column. Comptonization of these seed photons with highly energetic electrons lead to the power-law like resultant spectrum with high energy exponential cutoff.

Using this model, we have described the 3-70 keV broad-band phase-averaged spectra of EXO 2030+375 at 23 different luminosity epochs, covering the range of 10^{36}–10^{38} erg s^{-1}. As mentioned above, for a canonical neutron star mass and radius, the BW model has six free parameters, i.e. the diffusion parameter ξ, the ratio of bulk to thermal Comptonization δ, the column radius r_0, mass accretion rate $\dot{M}$, electron temperature T_e and the magnetic field strength B. Among these parameters, the mass accretion rate $\dot{M}$ was estimated by using the observed source flux obtained from high energy cutoff empirical model and considering a source distance of 7.1 kpc (Wilson et al., 2002). Since the column radius strongly depends on accretion rate

Table 5.1 Best-fitting spectral parameters with 1σ errors obtained from *RXTE/PCA* and *RXTE/HEXTE* observations of EXO 2030+375 with BW model.

Obs-Ids	Luminosity[a] (10^{37}ergs s^{-1})	BW model Parameters $\dot{M}$ (10^{17} g s^{-1})	ξ	δ	B (10^{12}) G	T$_e$ (keV)	r$_0$ (m)	Reduced χ^2 (*dof*)
91089-01-12-04‡	28.04 ± 0.84	14.96	1.88 ± 0.03	14.38 ± 1.01	4.25 ± 0.20	3.95 ± 0.11	177.0	1.22(103)
91089-01-12-05	28.22 ± 0.38	14.82	1.77 ± 0.02	17.57 ± 1.20	4.23	3.42 ± 0.10	165.0	1.04(80)
91089-01-15-00	27.12 ± 0.53	14.59	1.82 ± 0.02	16.82 ± 1.19	4.58	3.83 ± 0.10	158.0	1.05(104)
91089-01-14-03	26.36 ± 0.49	13.88	1.86 ± 0.03	17.03 ± 2.50	4.34 ± 0.25	4.01 ± 0.16	141.0	1.02(85)
91089-01-09-03	19.39 ± 0.39	10.44	1.98 ± 0.03	11.24 ± 0.91	4.66 ± 0.22	4.53 ± 0.12	138.0	1.09(105)
91089-01-09-00	17.11 ± 0.65	9.21	2.06 ± 0.05	9.64 ± 2.75	5.29	5.15 ± 0.40	116.0	1.09(104)
91089-01-08-01	13.40 ± 0.48	7.22	2.13 ± 0.05	10.48 ± 1.10	5.59	5.61 ± 0.14	105.0	1.08(107)
91089-01-07-00	11.63 ± 0.58	6.26	2.43 ± 0.17	4.22 ± 0.72	4.85 ± 0.35	5.56 ± 0.31	98.5	1.13(98)
92067-01-03-13	10.09 ± 0.54	5.43	2.44 ± 0.16	4.17 ± 0.54	5.18 ± 0.36	5.97 ± 0.40	74.0	1.09(90)
92067-01-03-11	8.17 ± 0.98	4.40	2.36 ± 0.29	4.30 ± 1.16	5.33 ± 0.35	6.14 ± 0.43	35.6	1.16(95)
92067-01-03-00	6.86 ± 1.47	3.69	3.11 ± 0.73	2.09 ± 1.07	5.03	6.32 ± 0.16	28.2	1.10(99)
93098-01-03-05	5.72 ± 0.70	3.25	1.91 ± 0.16	7.90 ± 1.38	4.85	4.85 ± 0.41	26.0	1.08(87)
93098-01-01-01	4.86 ± 0.46	2.79	2.08 ± 0.15	5.50 ± 1.10	4.35 ± 0.21	4.88 ± 0.27	25.5	1.05(111)
92422-01-25-06‡	4.74 ± 0.74	2.66	3.01 ± 1.19	2.43 ± 1.20	5.39 ± 0.45	6.68 ± 0.36	24.5	1.11(101)
93098-01-01-00	3.90 ± 0.83	2.34	5.08 ± 1.24	0.97 ± 0.35	4.78	6.32 ± 0.07	19.6	1.08(102)
92422-01-05-04	3.82 ± 0.84	2.22	7.37 ± 3.18	0.64 ± 0.21	4.82	6.53 ± 0.05	19.2	0.99(96)
93098-01-02-04	3.71 ± 1.08	1.98	7.26 ± 2.86	0.62 ± 0.27	4.70	6.34 ± 0.07	23.4	1.03(89)
92422-01-14-03	3.07 ± 0.75	1.74	6.11 ± 1.95	0.77 ± 0.29	4.50	6.09 ± 0.07	17.5	1.07(90)
80071-01-01-11	1.41 ± 0.01	0.81	6.49 ± 1.05	0.66 ± 0.13	3.74	5.24 ± 0.02	17.5	1.06(87)
80071-01-01-06	1.20 ± 0.01	0.67	8.15 ± 2.50	0.52 ± 0.20	3.77	5.29 ± 0.03	16.0	1.08(86)
80071-01-01-00	1.14 ± 0.01	0.64	7.11 ± 1.65	0.60 ± 0.17	4.02	5.69 ± 0.03	18.4	1.19(97)
80071-01-01-01‡	0.88 ± 0.01	0.48	7.89 ± 1.80	0.57 ± 0.15	3.75	5.32 ± 0.02	17.4	1.12(87)
80071-01-01-020	0.92 ± 0.01	0.44	10.29 ± 2.58	0.39 ± 0.16	3.69	5.28 ± 0.01	15.0	1.03(72)

Notes: [a]: The 3-70 keV luminosity in the units of 10^{37} ergs s^{-1} by assuming a distance of 7.1 kpc.
‡: Indicates the observation IDs from which the extracted spectra are shown in the Figure 5.2.

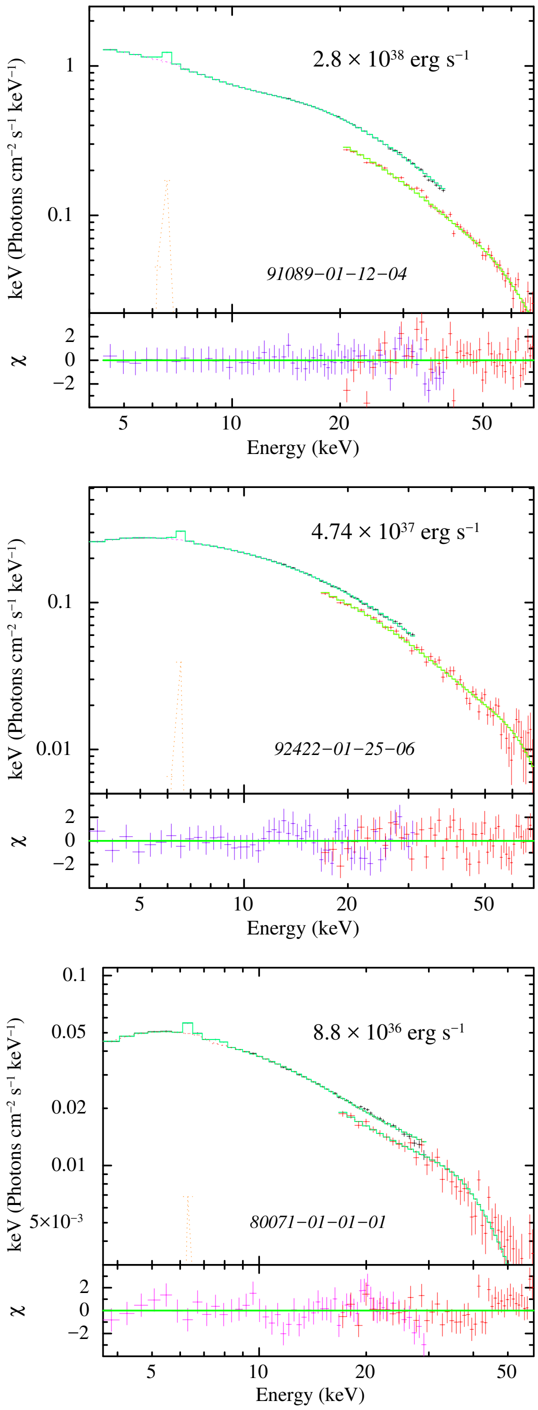

Fig. 5.2 Phase-averaged energy spectra of EXO 2030+375 at three distinct luminosities obtained during Type I and Type II X-ray outbursts obtained from PCA and HEXTE detectors. The spectra of pulsar was fitted with BW model (Ferrigno et al., 2009) along with an iron line at ∼6.4 keV and partial covering component (top panel of figure). Corresponding spectral residuals are shown in bottom panels of the figure. Presence of any absorption like feature was not seen in 10–20 keV energy range of the pulsar spectra.

(see Eqn. 112 of Becker and Wolff 2007), the parameter $\dot{M}$ was fixed at a given value while fitting the broad-band spectrum of the pulsar. After fitting, the column radius was also fixed for getting better constraints on other spectral parameters. This was done carefully by analyzing the 2-D contour plots between r_0 & $\dot{M}$, as done by Ferrigno et al. (2009). Other BW model components such as normalizations of Bremsstrahlung, cyclotron and blackbody seed photons were also kept fixed as suggested in the BW_cookbook[1].

A partial covering component as required in empirical models was also needed to explain the absorbed spectra of the pulsars during bright X-ray outbursts. The values of additional column density and covering fraction obtained from the BW model were found to be consistent with the values obtained with the high energy cutoff power-law model (see Table 4.2 of Chapter 4). Therefore, we have not discussed these parameters in this section. An iron fluorescence line at $\sim$ 6.4 keV was also added in the continuum. Spectral parameters obtained after best fitting the pulsar spectra with BW model are given in Table 5.1. The values of reduced χ^2 obtained from our fitting, as given in Table 5.1, showed that the BW continuum model fits the data well in a wide luminosity range. For three different values of pulsar luminosity, broadband energy spectra of the pulsar from PCA and HEXTE detectors, along with the best-fitted BW continuum model and Gaussian function for iron emission line are presented in top panels of the Figure 5.2. The bottom panels in this figure show corresponding spectral residuals of best fitted model. It can be seen that the residuals obtained from fitting the pulsar spectra with BW model did not show any evidence of presence of absorption like feature. This finding also supports the non-detection of cyclotron line in EXO 2030+375, as discussed in Section 4.3 of Chapter 4. Luminosity dependent variations in the parameters obtained after fitting the pulsar spectra with BW model are shown in Figure 5.3.

[1] http://www.isdc.unige.ch/~ferrigno/images/Documents/BW_distribution/BW_cookbook.html

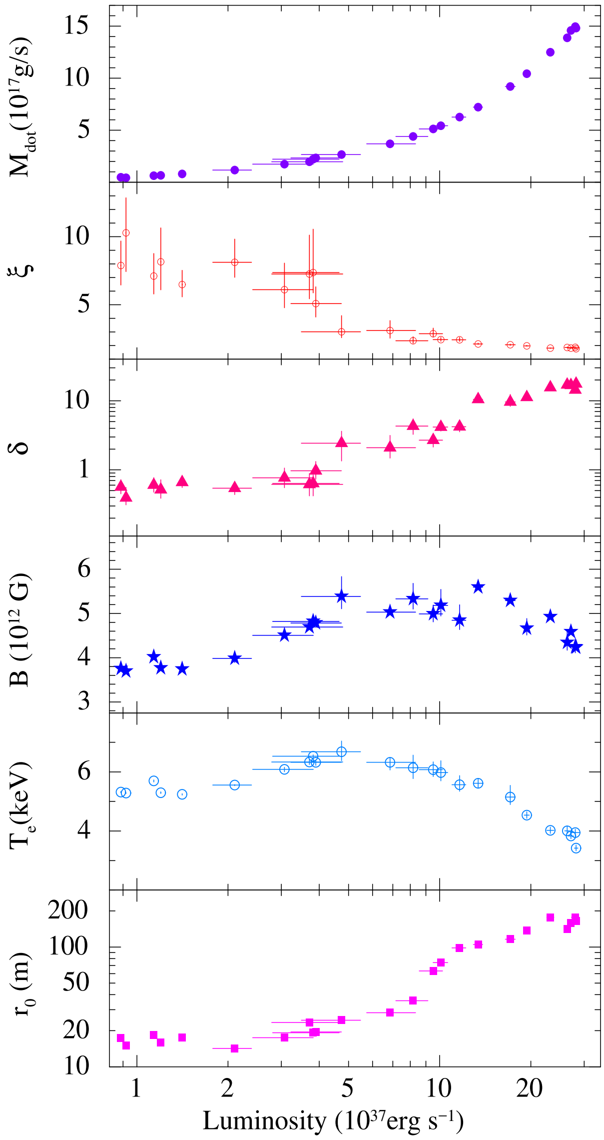

Fig. 5.3 Spectral parameters obtained from the fitting of phase averaged spectra of EXO 2030+375 with BW model at different luminosities. The top, second and third panels of figure show the mass accretion rate, diffuse rate and the ratio of bulk to thermal Comptonization in accretion column, respectively. While the fourth, fifth and sixth panels indicate the luminosity variation of magnetic field, plasma temperature and column radius, respectively.

5.2 Discussion

An interesting trend of parameter δ with luminosity was noticed in the third panel of the Figure 5.3. This parameter signifies the ratio of bulk to thermal Comptonization occurring in the accretion column. The value of δ was found close to unity at luminosity $\leq$(3–4)$\times 10^{37}$ ergs s^{-1}. This indicates that the effects of thermal and bulk Comptonization are nearly same in accretion column at lower luminosity of the pulsar. However, as the luminosity increases, the bulk Comptonization starts playing a major role in column emission. In comparison to the contribution of thermal Comptonization process in energizing the X-ray photons, it is seen that the bulk emission is higher by a factor of 20 as observed at lower luminosity.

The column radii (r_0), was found to strongly dependent on luminosity or mass accretion rate. An upper limit on the column radius r_0 is given by (Becker and Wolff, 2007, Eqn. 112).

$$r_0 \lesssim 6.5 \times 10^4 \left(\frac{B}{10^{12} G}\right)^{-2/7} \left(\frac{R_{NS}}{10\ km}\right)^{9/14} \left(\frac{M_{NS}}{\mathrm{M}_{\odot}}\right)^{1/14} \left(\frac{\dot{M}}{10^{17}\ gs^{-1}}\right)^{1/7} cm$$

Using the magnetic field value and mass accretion rate estimated for EXO 2030+375 at different luminosity, we have seen that the upper limit on column radius ranges in 400–650 m. Here the maximum value of upper limit correspond to the case of highest observed luminosity state of the pulsar as seen during peak of the Type II outburst (i.e Obs.-ID 91089-01-12-04, see Table 5.1). We note that the estimated values of r_0 in EXO 2030+375 are less than their upper estimates. At lower luminosities, in fact the r_0 values are an order of magnitude below the corresponding upper limits.

Moreover, the diffusion parameter ξ was also observed to vary with source intensity, showing a minimum value at higher luminosity. An alternative view of ξ is expressed by considering the ratio of dynamical time scale (t_{shock}) to the mean escape time scale (t_{esc}). Becker and Wolff (2007) define t_{shock} to be the time scale during which the accretion material reaches the neutron star surface from the sonic point. And t_{esc} is defined to be the time length for photons to diffuse through the walls of accretion column. The ratio of these two time scales is expressed as $\frac{t_{shock}}{t_{esc}} \sim 0.24\ \xi$ (see Equation 104 of Becker and Wolff 2007). In case of radiation dominated accretion flow in pulsars, Becker (1998) found the value of ξ to be $2/\sqrt{3}$. In the present case of EXO 2030+375, we have seen that at higher accretion luminosity where the accretion is presumably radiation dominated, the value of ξ is close to 1. As per Becker (1998), in a radiation dominated pulsar accretion column, this condition ensures that the accretion flow halts at the stellar surface. This also represents the balance of escape time scale of photons from the accretion column with that of the accretion time scale. A more physical explanation of this behaviour is reflected from the requirement that the kinetic energy of the flow through the column walls should be radiated away within the time in which the gas settles onto the star. In case of EXO 2030+375, we have seen that at higher values of pulsar luminosity, this is indeed the case as the plasma is radiation dominated. However at lower luminosities, the value of ξ is higher than 1.

In addition to these, the electron plasma temperature was changing in the range of 3 to 7 keV. The temperature showed a gradual increase up to luminosity 4×10^{37} ergs s^{-1}. Beyond this, cooling of plasma temperature was observed. This may occur in the presence of strong radiation dominated accretion shock at which the in-falling matter mostly bulk Comptonize the seed photons that carries plasma energy by diffusing through the side walls of accretion column. It leads to the settling of plasma in accretion column at lower temperature. This model also provides an opportunity to constrain the magnetic field of the pulsar which is found to be in the range of $\sim$(4–6)$\times 10^{12}$ G (see Figure 5.3). In some cases, magnetic field estimated from this model was found insensitive to upper value though their lower estimate was easily constrained in all these observations. Therefore, only best fitted values without error bars are quoted in Table 5.1.

Chapter 6

Summary and Future Scope

In the present thesis, the timing and spectral studies of two high mass X-ray binary pulsars have been carried out. Broad-band timing and spectral studies of transient Be/X-ray binary pulsar KS 1947+300 during its giant outburst revealed several interesting results for the first time in this source. The evolution of pulse profiles with energy has been investigated to understand the emission properties of the pulsar. The cause of rare absorption dip like features in the pulse profiles of KS 1947+300 emanating at hard X-rays and their near absence in soft X-rays has brought speculation of their origin. The cause of these dips was investigated and found that these dips are different to those generally seen in soft X-ray pulse profiles due to the absorption of soft X-ray photons by the narrow streams of matter that are phase-locked with the neutron star. Apart from the dips in the pulse profile, presence of pulsating soft X-ray excess, iron emission lines at 6.4 keV and 6.7 keV from neutral and He-like iron atoms, respectively, were detected in the pulsar spectrum. Phase averaged and phase resolved spectral studies of KS 1947+300 have shown that the pulsating "soft X-ray excess" emission component could possibly result in lack of dips in low energy pulse profiles. Other possible scenarios have also been investigated to explain the hard X-ray dips in the pulse profiles.

The enumerable outbursts of EXO 2030+375 as observed with *RXTE* were found to be indispensable for our studies. These observations captured the source emission at different luminosity levels of the pulsar. The pulse profile variations of EXO 2030+375 have been investigated across various phases of Type I and Type II

X-ray outbursts to understand the possible differences or similarities in emission geometries of column emission during these outbursts. An extensive phase-averaged spectral studies of EXO 2030+375 at wide range of source luminosities has been done to find the variations of spectral properties of the pulsar. These studies reveal that the pulsar was transiting across different emission geometries with varying mass accretion rate (and hence luminosity). We have also used a physical model to understand more about the accretion column properties of the pulsar. The results obtained from these studies have been the subject of discussion in Chapter 3 and Chapters 4 & 5. In the present chapter, I lay out a summary of the work done in these chapters. A future endeavour of such studies and their impact on the subject area is also mentioned briefly.

6.1 Summary

In Chapter 3, we presented the timing and spectral properties of the transient BeXB pulsar KS 1947+300. The observed pulsations in the light curves of KS 1947+300 during two different epochs of its 2006 giant outburst showed that the pulsar was spinning up rapidly. The spin-up of the pulsar was justified on the basis of the accretion model of Ghosh and Lamb (1979). This is due to transfer of large amount of angular momentum of the accreting matter onto the neutron star. Using the results of quasi-spherical settling accretion theory, we could estimate the neutron star dipole magnetic moment (and hence the magnetic field) from the observed spin-up rate of the pulsar. Thus, the surface magnetic field of the pulsar was estimated to be around $\sim 1.2 \times 10^{12}$ G. Our estimation of magnetic field agrees with the value of the magnetic field derived from the detection of cyclotron resonance scattering features in the pulsar spectrum independently. The pulse profiles of KS 1947+300 have shown the presence of a narrow dip like feature evolving with energy in hard X-rays. However below 10 keV, the pulse profiles are smooth and single peaked. The phase averaged spectral studies of the pulsar have been carried out by using best fitted NPEX continuum model. We have also detected the presence of additional matter near the pulsar which has been studied by using a partial covering absorption component in the spectral model. However, a close inspection of the spectra through phase-resolved studies revealed that the amount of additional matter detected near the dip phases of the pulsar was substantially less to absorb high energy photons leading to such prominent dips in the hard X-ray pulse profiles. Based on the asymmetric position of the dip features in the pulse profiles, we envisaged that it may not be the viewing angle through the accretion column rather a geometrical effect causing dips in hard X-ray pulse profiles. The pulsating soft X-ray excess component as detected through the pulse phase resolved spectroscopy confirmed that the location of this excess emission region is confined to nearby region of the pulsar. Following an estimation of size of this emission region, we found that the nearby region of accretion column in EXO 2030+375 was the site of this excess emission. The absence of dips in the soft X-ray pulse profiles could be due to additional soft X-ray emission at these phases cancelling the effect up absorption dip structure in forming a smooth and single peaked pulse profile. Apart from soft excess, we have also identified fluorescence Fe-Kα line emission at 6.4 keV and emission from helium like iron atoms at 6.7 keV in the phase averaged spectra of KS 1947+300. The overall spectral parameters during the two epochs of the outburst were found similar apart from the blackbody component representing the soft X-ray excess emission. During the peak of the outburst, the temperature and flux of the blackbody component were comparatively higher than the first *Suzaku* observation that was taken a month before the second observation. The accretion luminosity of the pulsar ($\sim 10^{38}$ergs s^{-1}) during the giant outburst was way higher than the computed critical luminosity ($i.e. L_{crit} = 1.6 \times 10^{37}$ ergs s^{-1}) of the pulsar. This showed that the pulsar was accreting in the super-Eddington regime. However, we note that even at such high luminosities, we could not find the presence of any harmonics of cyclotron resonance scattering features in the pulsar spectrum in 10-100 keV range.

We have studied extensively the properties of another BeXB pulsar namely EXO 2030+375 in Chapter 4. In earlier studies, the properties of the pulsar have been studies during any particular X-ray outburst by using a single or a few pointed observation at different phases of the outburst. Such studies were helpful in finding the characteristic emission features at a particular luminosity of the pulsar during individial outburst. However, in BeXB pulsars, it is seen that the pulse profile structures show strong luminosity dependent variations in addition to usual energy dependent evaluations. Hence, in order to understand the source emission in wide range of pulsar luminosity, it is important to consider many pointed observations of a pulsar carried out while the pulsar was in different intensity levels observed during several X-ray outbursts of different peak luminosity. The *RXTE* observations of EXO 2030+375 comprising of many Type I outbursts in 1996-2011 and a long duration Type II outburst in 2006 have made it feasible to investigate the luminosity dependent emission properties of the pulsar. Secondly, such studies helped further in finding the similarities and variations of X-ray emission during different types of outburst exhibited by the source. In a way, this could become an important milestone in finding the possible cause of such intense Type II outbursts in the pulsar whose origin remains unclear till date. These studies also can provide information on the nature of the companion Be star and the evolution of its equitorial circumstellar disk.

The pulse profile studies of EXO 2030+375 at different flux levels showed that the profiles are strongly luminosity dependent. Although the physical mechanisms behind the cause of Type I and Type II outbursts in BeXBs are known to be completely different, the pulse profiles during these outbursts at similar flux levels show similar structure and variations. This illustrated that the beam function of the pulsar remains unaffected at a certain luminosity irrespective of the type of X-ray outburst and its mechanism. In other words, it solely depends upon the mass accretion rate onto the pulsar. Based on these studies, it is observed that at low luminosity (and hence low accretion rate), the pattern of the pulsar emission is dominated by pencil beam. However, at peak luminosity of Type II outburst, the geometry of emission pattern was found to be that of purely a fan beam type of emission. We could explain the phase averaged spectra of EXO 2030+375 by using a high energy cutoff power law model. At high intensity phases of the pulsar, particular those corresponding to 2006 Type II outburst observations, we have found the evidence of additional matter present at close proximity of the pulsar. Among the changes in spectral parameters, we have found that the variation in photon index showed three different patterns with luminosity. Subsequently it was identified that the spectral transition of the source from sub-critical to super-critical accretion regime was causing such patterns in the power-law photon index. The critical luminosity regime of EXO 2030+375 in this way was derived to be $\sim L_{crit} \sim 4 \times 10^{37}$ ergs s^{-1}. In this regime, a mixture of pencil and fan beam emission pattern has been seen from the corresponding pulse profile variations with luminosity. The variation in the hardness ratio also showed the signatures of emission transition in the pulsar. Apart from this, we have seen that earlier detection of cyclotron absorption line at ~ 11 *keV* in the hard X-ray spectra of the pulsar largely remained speculative. The detection of CRSF feature was highly model dependent. It could be identified with single cutoff based models. The *NuSTAR* spectra taken during a low intensity phase of the pulsar also showed absence of CRSF feature in hard X-rays.

A physical model explaining the column emission in EXO 2030+375 was never attempted before. In Chapter 5, for the first time we have attempted to probe the pulsar accretion column emission at wide range of luminosity. We have used the BW model Ferrigno et al. (2009) based on the thermal & bulk Comptonization in accretion cloumn developed by Becker and Wolff (2007). Using this physical model, we estimated the magnetic field of the pulsar to be $\sim (4-6) \times 10^{12}$ G. The radius of accretion column was found to have a dependence on mass accretion rate. At high luminosity state of the pulsar, it was found that the bulk Comptonization plays a major role in shaping the pulsar emission. However at lower luminosity, both the Comptonization processes (*i.e.*thermal and bulk Comptonization) play equally significant role in the dynamics of column emission from the pulsar. The electron plasma temperature was varying within 3-7 keV. As the luminosity of the pulsar was increasing beyond the critical luminosity level, we noticed the cooling of the plasma temperature from its peak value. It may be the case that at high luminosities, the formation of a radiation dominated shock mostly bulk Comptonize the seed photons that diffuse through the column side walls carrying away the kinetic energy of the plasma. Subsequent settling of the plasma in the accretion column substantially cools it as the temperature decreases.

6.2 Future Outlook

The extensive study of outburst observations of EXO 2030+375 carried out in the present work have strengthened the fact the long term X-ray variabilities of BeXB pulsars show signatures of spectral transitions. This helped in identifying the different accretion regimes of the pulsar. The timing studies also proved useful in finding the varying emission patterns of the pulsar. Based on these studies, we could estimate the critical luminosity. Secondly, an estimate of one of the intrinsic physical parameter of the pulsar, *i.e.*its magnetic field could be constrained. There are only few pulsars in which the CRSFs have been identified in their spectra. Using this, we can have an estimation of field intensity in these pulsars. Other than these, among the less direct methods, we propose that the identifying the critical luminosity regime from the phase averaged spectral studies of the pulsar could be an important step in having an approximate estimate of magnetic field in accreting X-ray pulsars. Since the Type II X-ray outbursts are rare and unpredictable, timing and spectral investigation of such intense outbursts in other BeXBs could help us in finding unique physical properties shared among all the pulsars. Probably the extensive studies on other BeXBs in future, could possibly explain the origin of these unpredictable and rare events. The long term spectral variabilities of BeXBs during various outbursts at different intensities could help in describing the column emission from the pulsar even at low X-ray luminosity through the improvement of existing or development of new physical models. A comparison of pulse profiles at luminosity in other BeXB pulsars (as done in the present study of EXO 2030+375) would be useful to identify whether the luminosity dependence of column emission geometry is characteristic to all accretion powered X-ray pulsars. With the new X-ray observatories active at present, such as *NuSTAR*, *AstroSat* having better spectral and timing capabilities than their contemporaries, we can probe different emission regions of the pulsars to understand the dynamics of accretion column.